

The Erosion of Metals

A dissertation submitted to the University of Cambridge for the degree of Doctor of Philosophy.

David Richard Andrews

Selwyn College

Cambridge

May 1980

Memorandum I

The work described in this dissertation was carried out between October 1976 and January 1980 in the Cavendish Laboratory under the supervision of Dr J. E. Field. Unless specifically stated otherwise, all work is the result of my own research activities and none of it has been used previously in a degree thesis submitted to Cambridge University or any other university.

David R Andrews

David Richard Andrews

Selwyn College

Cambridge

Memorandum II

This thesis was converted from a hard-back (paper) book into an electronic document in February and March 2015 for inclusion in the University of Cambridge's on-line library, so that a wider public may gain access to it. The process of conversion included:

- Optical scanning and character recognition of text.
- Optical scanning and creation of image files for figures.
- Creation of a Microsoft Word 2007 document into which text and files have been pasted.
- Mathematical equations were recreated manually using the equation editor in Word.
- Similarly, references were recreated manually using Words bibliography manager.
- Flow diagrams were recreated using Microsoft Visio and pasted into the Word document.

The creation of the Word document was done to improve the final appearance and to compress the size of the electronic thesis. The following changes have also been made:

- Re-formatting – the greatest change to appearance by far.
- In a very few places one or two words were found to be missing from the original thesis and these have been added.
- A new, short section on historical context has been added to the section titled Importance of Erosion.
- One reference error has been corrected.
- In one equation the explanation of variables has been changed to reflect convention.
- The title of one chapter has been altered by adding a few words – to reflect a discussion with one of the examiners of the thesis in 1980.
- Equation numbers have been altered to include the chapter in which they are first created.
- Generally, shortened terms like: *E.g.* and *viz* have been converted to prose.
- In several places the use of inverted commas around words to indicate some special or unusual context has been replaced with italic letters, to conform to popular use; italic letters were not readily available to Mrs Lonzarich in 1979/80 when she typed the original thesis.

The changes above were made to improve readability of the electronic thesis and have not in any way changed the scientific content. I have performed all the above tasks myself to ensure the quality of conversion.

David Richard Andrews

camben@cambridgeultrasonics.com. Cambridge Ultrasonics, Over, Cambridge CB24 5NX, UK

Acknowledgements

I would like to thank Dr J. E. Field for his help, advice and interest throughout the duration of this work. I am also deeply indebted to him for the opportunity to join the Physics and Chemistry of Solids research group of the Cavendish Laboratory.

I would also like to thank Professor D. Tabor, Dr I. M. Hutchings, Dr M. Chaudhri, Dr D. Gorham, Dr J. Matthewson and Mr P. N. H. Davies for stimulating conversations concerning the work described here. May I also take this opportunity to thank the many research assistants and technicians of the Cavendish for their help with innumerable pieces of equipment but in particular Mr P. N. H. Davies, Mr C. Naunton and Mr D. L. Johnson.

I wish to thank the Science Research Council and United States Air Force for financial assistance. British Gas has been most generous in connection with this work by the loan of equipment - my thanks go to them and in particular to Dr M. Howe and Dr I. Glasgow. I would like to thank Rolls Royce (1971) for allowing me to visit their research laboratories at Hucknell.

Lastly, but by no means least, may I thank Mrs C. Lonzarich for her patience and excellence in typing the original manuscript.

David Richard Andrews

Selwyn College

Cambridge

1980

I would also like to thank Cambridge Ultrasonics for allowing me to use its facilities for converting this thesis into electronic format and for allowing me some time away from work to perform the conversion process.

David Richard Andrews

Cambridge Ultrasonics

Cambridge

February 2015

Summary

The study of the erosion of metallic surfaces by solid particles has been an area of dispute recently (1980) especially concerning the importance of target melting as a mechanism for the removal of material. In addition, erosion by particles at a normal angle of impingement has remained unexplained and there has been no satisfactory theory of erosion which has taken into account the statistical nature of erosion, that is, the continual bombardment of a surface by a large number of eroding particles.

This work concentrates on the foregoing aspects of erosion. Apparatus is described which is capable of producing erosion by single impact and continual bombardment. Conditions conducive to target melting are discussed and under equivalent experimental conditions target melting is deduced to have occurred. The statistical nature of erosion has been approached from two directions:

1. The importance of the shapes of eroding particles.
2. Considering the influence of the erosive flux on the temperature of the target and resulting erosion rate.

Material removal by single impacts at normal impingement has been observed using high-speed photography.

Contents

The Erosion of Metals	1
Memorandum I	2
Memorandum II	3
Acknowledgements.....	4
Summary	5
Importance of Erosion	9
Extract from The Times 28th April 1980.	9
Historical context	9
Chapter 1 Review	10
1.1 Introduction	10
1.2 Erosion Prediction	11
1.3 Mechanism (1): Erosion by Cutting.....	13
1.4 Fragmentation and Scouring.....	16
1.5 Mechanism (2): Fatigue of the Impact Surface.....	17
1.6 Mechanism (3): Target Melting	18
1.7 The Effects of Temperature and Strain-rate	20
1.8 Aerodynamic and Geometric Effects	22
1.9 Prediction of Erosion Resistance.....	22
Chapter 2 Aims of This Work and Theory	26
2.1 General Aims.....	26
2.2 (a) Statistical Nature of Erosion - I	26
2.3 (b) The Importance of Target Melting	27
2.4 (a) Statistical Nature of Erosion - II	31
2.5 Forces Experienced by a Sphere during Impact.....	42
2.6 Erosion at Normal Impingement.....	44
2.7 Improving the Erosion Resistance.....	45
2.8 Apparatus	45
Chapter 3 Single Particle Erosion Rig	46
3.1 Design Specification	46
3.2 Gas gun.....	47
3.3 Projectile Velocity Measurement	53

Timer Circuit Operation	55
3.4 Specimen Heating	57
3.5 Specimen Chamber	59
3.6 Safety Considerations	61
3.7 Performance	62
Chapter 4 Quantitative Observations of Single Impacts	63
4. 1 Introduction	63
4.2 Moiré Topography	64
4.3 Specimens	68
4.4 Results	69
4.5 Change of Mass as a Result of Impact	72
4.6 Conclusion	73
Chapter 5 Qualitative Observations of Single Impacts	75
5. 1 Introduction	75
5.2 Strain Fields	75
5.3 Features of Copper Deformation	78
5.4 Features of Nimonic 105T Deformation	83
5.5 Features of the Deformation of Mild Steel (ENIA)	86
5.6 Features of Titanium Deformation	88
5.7 Features of Bismuth Deformation	89
5.8 Conclusion	90
Chapter 6 Statistics of Real Erosive Particles: Towards a Geometric Classification	92
6.1 Types of Erosive Particles	92
6.2 Correlation between Shape Index and Impact	93
6.3 Conclusion and Discussion	97
6.4 Summary	99
Chapter 7 Erosion at Normal Impingement Angles	101
7.1 High Speed Photography	101
7.2 Theoretical considerations	106
7.3 Conclusion	109
Chapter 8 Multiple Particle Erosion Rig	110
8.1 Introduction	110
8.2 Acceleration Tube	110

8.3 Grit Ingestion Controller	113
8.4 Specimen Chamber	114
8.5 Velocity Measurement.....	115
Time of flight: a deduction by cross-correlation.....	116
Velocity Measurement: Rapid Assessment	122
8.6 Safety Considerations	125
8.7 Performance of the Erosion Rig	125
Chapter 9 Conclusion and Discussion	126
9.1 Major Themes of This Work.....	126
9.2 Importance of Target Melting.....	126
9.3 Statistics of Impact.....	127
9.4 Normal Impact	127
9.5 Discussion.....	127
Appendix A.....	129
Correct adjustment of the velocity measuring circuit (Single impact)	129
Appendix B	131
Curve fitting to impact craters	131
Computer Listing	134
Appendix C	139
Computer aided cross-correlation	139
PLS method of C-C: Flow diagram.....	141
PLS method of C-C: computer program (HP-L)	142
PLS and SM method of C-C: Test data.....	146
Appendix D.....	148
Properties of the Cross-Correlation Function	148
Velocity Distributions.....	151
Bibliography	154

Importance of Erosion

Extract from *The Times* 28th April 1980.

“The flight was about 500 miles, the limit of the helicopters’ range. Three of them flew into a severe sandstorm.

The other two helicopters caught in the sandstorm landed and waited for conditions to improve. They then went on to the rendezvous.

One of the seven remaining helicopters suffered a severe mechanical failure and had to land. It is not clear whether this was one of those affected by the sandstorm. Its crew was picked up and six helicopters, therefore, reached the base, known as *Desert One* where the six C130s were waiting.

Everyone said the flight from the Nimitz to Desert One was the most difficult part of the operation. The helicopters had to fly very low to avoid Iranian radar and found the weather conditions worse than expected.”

Historical context

There was a revolution in Iran in the years 1978 and 1979. The Shah of Persia went into exile in 1979, resulting in the formation of an Islamic state in Iran. The new regime did not respect the sovereignty of the embassy buildings of the United States of America in Teheran and on 4th November 1979 the Embassy staff and occupants were taken as prisoners and hostages for 444 days. The then US President, Jimmy Carter, authorised the armed forces of the USA to mount a mission to rescue the American hostages on 24th April 1980. The mission was unsuccessful due to mechanical failure of the helicopters, which were forced to fly close to the ground through a sandstorm. Almost certainly erosion of the leading edges of turbine blades (probably made of Nimonic alloy – see later in this study) in the helicopter engines contributed to the failure of the mission, caused by the engines ingesting large quantities of sand. In Iran, the failure of the American military mission was hailed as an act of god.

Chapter 1 Review

1.1 Introduction

Erosion is a wear process. In the work described here only one class of erosion will be discussed in detail: the erosion of ductile metal surfaces by the impingement of solid particles.

Erosion is commonly measured in terms of a parameter W which is equal to the mass of material removed from the surface divided by the mass of the eroding material. Occasionally it is more convenient to refer the parameter to the volume loss divided by the volume of eroding material. In either case the parameter is dimensionless.

$$W = \frac{\text{Mass lost from surface}}{\text{Mass of impacting material}}$$

In most cases $W > 0$, a condition which indicates that material is removed during erosion but under certain circumstances $W < 0$.

Within the last twenty years erosive wear has become of increasing interest and a considerable research effort has been directed towards elucidating the mechanisms of erosion. This intensive study has been made usually in order to minimize the undesirable effects of erosion, however, erosion can have beneficial effects, for example: the shot-peening and peen-forming processes (Meguid, Johnson, & Al-Hassani, 1976).

It seems likely that a heuristic approach will still remain more useful for predicting erosion under a given set of industrial conditions. The reason for this is because there are a large number of parameters which influence the rate of erosion and these can be interrelated (for example: eroding particle velocity, site and angle of impingement are not independent due to the aerodynamic flow field around the target).

The examples of industrial problems attributable to erosion are exhaustive but some of the more common and well-documented cases are listed briefly here:

- (a) The erosion of turbine blades in gas-turbine aero-engines, especially helicopter engines which suffer from the adverse effects of ingesting sand or salt grains whilst hovering.
- (b) Damage to pressure vessels and pipes in the catalyst cracking of petroleum oils (Finnie A. , 1960).
- (c) Erosion of components in fluidized-beds (Wood & Woodford, 1979).
- (d) Erosion of ducts and pipes carrying pulverised coal in coal-fired power stations (Raask, 1979).
- (e) Plant erosion, especially in the cyclone stages of the so-called *coal-gassification process* to produce methane gas directly from coal (Dapkunas, 1979).
- (f) Erosion of jet nozzles and nozzle guide vanes.

In many industrial cases erosion occurs along with chemical attack of the metallic surface. This co-operative effect can be particularly damaging and is termed erosion-corrosion.

The range of particle sizes commonly encountered in industrial erosion is roughly 1 μm — 1 mm, the larger sizes being flakes of friable material that may disintegrate forming smaller sized particles. Erosion has been observed for velocities in the range of 10 — 500 ms^{-1} . The range of velocities above 500 ms^{-1} is termed the hyper-velocity region where the projectile velocity is commensurate with the speed of sound in the target. This field of study has many features associated with it that are quite distinct from the sub-sonic range of velocities and will not be considered in this study. The velocity range lower limit does extend in theory to velocities below 10 ms^{-1} , but there are very few instances reported of erosion below 10 ms^{-1} .

1.2 Erosion Prediction

A particle moving faster than about 0.5 ms, relative to a stationary surface, will leave a permanent indentation or crater if it should strike the surface. Below this velocity the indentation is purely elastic and therefore recoverable (Davies, Proceedings of the Royal Society A (197), 1949). If the crater so formed has a volume V and if the target has an indentation hardness of P , then the total work done during the impact is,

$$\text{Work done during impact} = \int_0^V PdV + \text{kinetic energy of eroded material}$$

If we neglect the second term on the right-hand side of the expression, and assume that the indentation hardness is substantially constant during the impact - and there is good indirect evidence in support of this (Hutchings, Winter, & Field, 1976), (Rickerby & MacMillan, 1979). Then the change in kinetic energy of the projectile is given by the following relation, where m is the mass of the projectile, v_{in} and v_{out} are respectively the incident and rebound speeds of the eroding particle.

$$\text{Change in kinetic energy} = \frac{1}{2}m[v_{in}^2 - v_{out}^2] = PV$$

Equation 1.1

We arrive at a simple prediction of erosion by two assumptions:

1. v_{out} is proportional to v_{in} .
2. The volume lost during the impact is a fixed proportion of the crater volume V .

Then,

$$V = \frac{\beta m v_{in}^2}{P}$$

Where β is an undetermined constant. The erosion parameter, W , can now be obtained by dividing by the volume of the projectile and noting that mass divided by volume is density, ρ .

$$W = \frac{\beta \rho v_{in}^2}{P}$$

Equation 1.2

We now make the assumption that a random battering of the target surface is equivalent to the sum of many, similar impacts, in which case the erosion parameter is unaltered and v_{in} becomes the average velocity of the eroding stream.

Many researchers have put considerable effort into finding purely empirical relations for their particular erosion problems. Interest has concentrated on the erosion dependence of three principal parameters: the mean particle size, d , the average velocity of the erosive particles v , and the angle of impingement, α , between the velocity vector and the target surface. (Note: there are two definitions of this angle, α : one measured between the velocity vector and surface normal and another, between the velocity vector and a projection of the velocity vector onto the plane of the target surface. In common with the majority of literature on the subject of erosion I will use the latter definition).

A general, empirical erosion relation is of the form:

$$W = f(\alpha)v^x d^y$$

Equation 1.3

Where x has been reported to have a range of values $2.0 \leq x \leq 3.4$,

Metals	Value of x in equation 1.3	Source
Pure metals	2.1 to 2.5	(Finnie, Wolak, & Kabil, Journal of Materials (2), 1967)
Alloys	2.3	(Goodwin, Sage, & Tilly, 1969)
Alloys	2.35	(Sheldon, Maji, & Crowe, 1977)
Alloys	2.0	(Smeltzer, Gulden, McElmury, & Compton, 1970)

and y may take on a range of values $0.9 \leq y \leq 3.0$. It should be regarded as the aim of any theoretical model of erosion to be able to predict relations of this form.

The function $f(\alpha)$ has been determined experimentally (Finnie A. , 1960); it has the form shown in Figure 1.1 which is similar for all ductile metals. The curve for brittle materials is shown for comparison.

It has been a common failing of theoretical models to be unable to predict a velocity exponent greater than 2.0; compare equations 1.2 and 1.3. Finnie and McFadden (Finnie & McFadden, 1978), however, have succeeded in predicting an exponent within the empirical range.

At present there is only partial consensus of opinion as to the dominant mechanism(s) of ductile erosion. Those proposed and having popular acceptance are:

1. Cutting or micro-machining of the target material surface by the erosive particles.

2. Fatigue wear of the eroded surface due to repeated impact.
3. Melting or ablation of the target surface by the erosive particles.

1.3 Mechanism (1): Erosion by Cutting

Figure 1.2 shows three similar mechanisms of erosion, each producing plastic deformation by raising chips or lips at the projectile exit end of the crater, and in two cases removing material at the same time.

Finnie (Finnie I. , 1958) (Finnie A. , 1960) first proposed and later refined (Finnie I. , 1972) the idea of deformation by cutting. He envisaged an irregular-shaped, sharp-cornered particle striking a ductile, plane surface and removing a chip by a process of micro-machining. The direct evidence in support of this theory was based largely on scanning electron microscopy (SEM) examination of eroded surfaces (Tilly 1973).

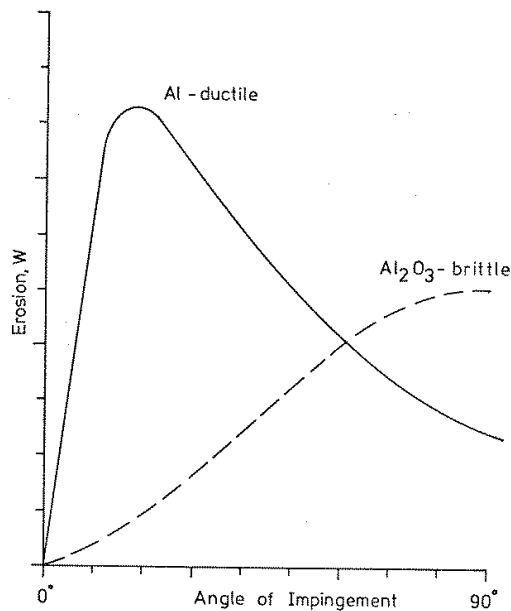


Figure 1.1

A comparison of the erosion rates of ductile and brittle materials as a function of impingement angles, α , (Finnie, Wolak, & Kabil, Journal of Materials (2), 1967).

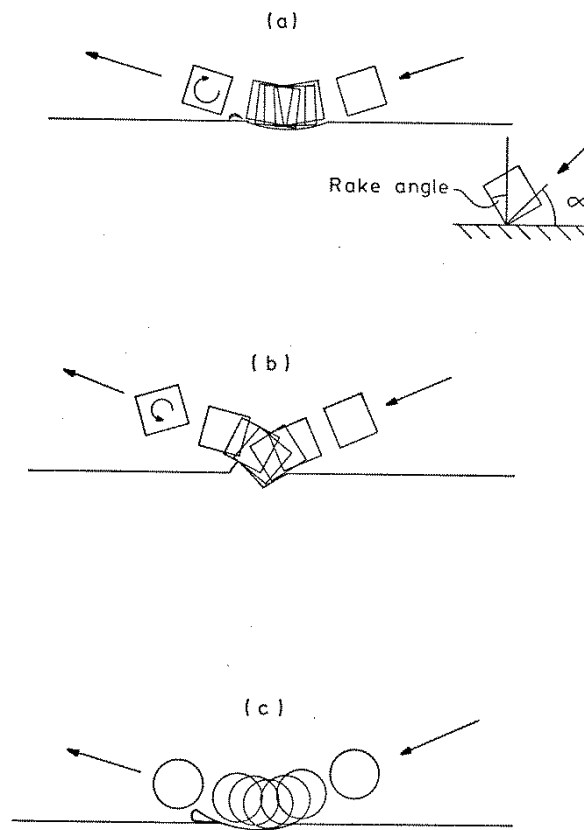


Figure 1.2

The cutting mechanism of erosion (three categories of impact).

Figure 1.2 Shows the three categories of impact in the cutting mechanism of erosion:

- (a) Angular particle (square sectioned in this case) - back rotating and micro-machining.
- (b) Angular particle - forward rotating and not removing material.
- (c) Spherical particle - ploughing and raising a lip that can be detached from the surface.

Inset in the figure is the definition of rake angle.

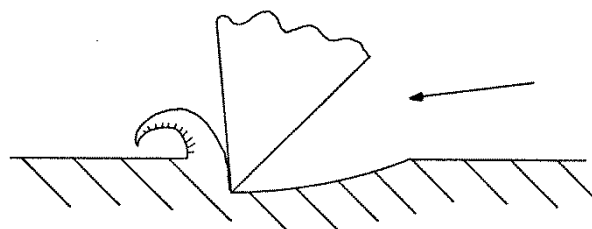


Figure 1.3

A Finnie-type of erosive particle with a cutting tip.

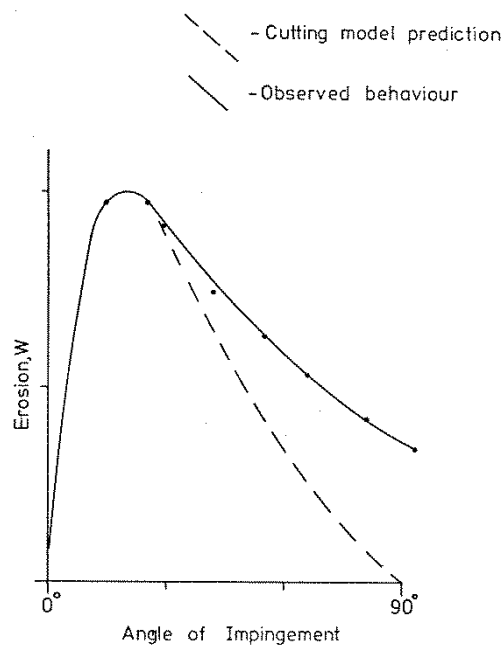


Figure 1.4

Finnie-model prediction of cutting erosion as a function of impingement angle, α .

Hutchings (Hutchings I. , 1977) and Hutchings et al. (Hutchings, Winter, & Field, 1976) studied the impact of single particles, very much more massive than typical erosive particles (of the order of several millimetres), and showed, using high-speed photography of the impact event, that micro-machining could take place under suitable circumstances. They showed that there exist three regimes of cutting according to the particle shape and orientation at impact.

1. Spherical particles will *plough* the target surface, raising a lip that may detach at sufficiently high velocities.
2. Square-sectioned, angular particles will rotate on impact, machining a chip from the target if the particle is rotating backwards during the impact.
3. Square-sectioned, angular particles will rotate on impact raising a firmly attached lip if the rotation is forwards.

Hutchings (Hutchings I. , 1977) suggests that there is a simple geometric relationship between the impingement angle of the angular projectile and the rake angle of its leading edge (see figure 1.2 inset) which governs its subsequent rotation during the impact.

Hutchings et al. (Hutchings, Winter, & Field, 1976) have modelled by computer both types of projectile impacts, spherical and square-sectioned, simulating the behaviour of the target and projectile during the impact. The authors assume that the target is a rigid-plastic material with constant flow pressure during the impact and that the projectile does not deform during the impact. They claim good agreement for angular particles, predicting the transition behaviour from forward to backward rotation, but only fair prediction of the crater volume for spherical projectiles. Rickerby

and Macmillan (Rickerby & MacMillan, 1979) have pointed out that very good agreement is possible in the latter case when a more accurate estimate is made of the area of contact between the sphere and target during impact. This being the case, it is strong indirect evidence that it is sufficient to consider the target material as being perfectly plastic during impact and it is not necessary to consider the effects of heating during the impact process.

The initial attraction of the Cutting model was its ability to predict the observed peak of erosion at impingement angles of 15° to 30° (Finnie A. , 1960) (see figure 1.4). This method of prediction is based on a mathematical analysis which, by contrast to Hutchings' work, does not consider particle rotation to be important during the impact. It does, however, assume that the yield stress of the target is constant during the impact - in concord with Hutchings' assumption.

Recently, Finnie and McFadden (Finnie & McFadden, 1978) have shown that the same analysis can predict a velocity exponent, x , greater than 2.0, typically $x = 2.6$ (see equations 1.2 and 1.3).

The major failing of the Finnie-Hutchings cutting model is its inability to predict erosion at normal incidence; Finnie's analysis predicts $W = 0$ for $\alpha = 90^\circ$. Many authors have assumed a dual mechanism for erosion, combining cutting with other mechanisms to account for the non-zero erosion at normal incidence. This further assumption may not be necessary; it is very likely that aero-dynamic effects on small erosive particles ($\sim 50 \mu\text{m}$) allow them to strike the target at angles less than ninety degrees and thereby cause erosion.

1.4 Fragmentation and Scouring

Erosive particles are usually brittle, for example: silicon carbide, quartz, sand etc. All of these materials will fracture into small fragments under suitable loads. Tilly (Tilly, 1973) has shown conclusively that this may occur during impact, using high-speed photography to follow individual $500 \mu\text{m}$ size quartz particles striking a steel target. He suggests that fragmentation will only occur for brittle particles larger than about $30 \mu\text{m}$ in size at velocities below 330ms^{-1} . He also suggests that the contribution to erosion from scouring rises monotonically from zero at $\alpha = 0^\circ$, to a maximum at normal incidence, but that it cannot fully account for the erosion observed at $\alpha = 90^\circ$ (see figure 1.5). He offers no statistical prediction of the proportion of grains which will fragment during erosion.

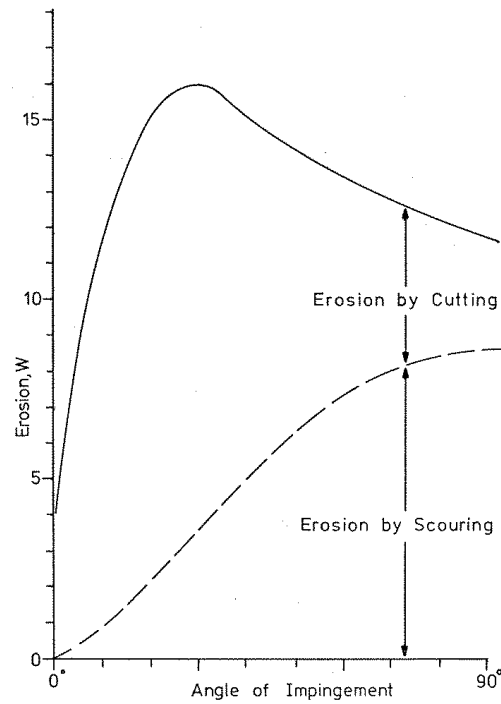


Figure 1.5

Erosion as a function of impingement angle, α , which shows the proposed contributions due to cutting and scouring as envisaged by Tilly (Tilly, 1973).

1.5 Mechanism (2): Fatigue of the Impact Surface

Not all impacts lead to a cleanly machined chip that is removed by the particle forming it: the lip raised by forward-rotating angular particles in Hutchings' experiments still seems to be firmly attached to the surface. If a second impact occurs within the plastic strain field of the first then it may be possible for material to be removed. Shewmon (Shewmon, 1979) has shown that this kind of fatigue wear can occur for only two overlapping impacts.

Hutchings (Hutchings I. M., 1979) tentatively proposes the use of the Coffin-Hanson equation in a general analysis of this wear process. However, he does this without considering the details of how this equation, based on results from cyclic-bending measurements, may be applied to the random loading found in erosion. In addition, the Coffin-Manson equation is commonly used for loading cycles up to 10^4 times, this figure should be compared to that of Shewmon.

Hutchings deduces an erosion relation of the form,

$$W \propto \left[\frac{\Delta \varepsilon_p}{\varepsilon_f} \right] \frac{\rho v^2}{P}$$

Equation 1.4

Where $\Delta\varepsilon_p$ = plastic strain introduced per cycle, ε_f = strain to failure in a conventional tensile test, ρ = density of impacting material of velocity v and P is the indentation pressure of the target.

This relation shares the value of 2.0 in the exponent of velocity, in common with the simple theory of erosion in equation 1.2. Apparently,

$$\left[\frac{\Delta\varepsilon_p}{\varepsilon_f} \right] = 0.1$$

from which it is possible to make a fair order-of-magnitude estimate of the erosion parameter, W , for one material under one condition of erosion. In view of the fact that there are still largely undetermined parameters in equation 1.4 this single prediction seems almost obligatory. In its favour it does represent the first attempt to draw upon a proven empirical relation from the field of fatigue. Other workers have only suggested the mechanism of fatigue to explain erosion at normal incidence (Finnie I. , 1972) (Eddington & Wright, 1978).

It is the case that the use of the word *fatigue* to describe this type of wear is a misnomer, for reasons already partially elucidated in this section. The standard fatigue test is a bending test and after failure the specimen very often does not exhibit any signs of failure except a crack. Perhaps for this and other reasons Bitter (Bitter, 1963) chose instead to call this mechanism *deformation wear*. This title has no popular favour at present.

In his analysis, Bitter includes a plastic threshold velocity corresponding to purely elastic, recoverable deformation (Davies, Proceedings of the Royal Society A (197), 1949); this inclusion is arguably negligible. Bitter splits-up erosion into cutting wear and deformation wear, and proceeds by an energy consideration suggesting that deformation wear, W_D , is given by

$$W_D = \frac{m}{2\varepsilon} (v \sin(\alpha) - K)^2$$

Equation 1.5

Where α = angle of impingement, m = mass of impacting material, ε = energy required to remove unit volume of target material, K = threshold velocity for plastic deformation.

Since Bitter has employed a general energy argument there is no reason to restrict material selection to ductile metals. Bitter and subsequent workers Nielson and Gilchrist (Nielson & Gilchrist, 1968) and (Kleis, 1969) use the same equations but without the cutting term to predict the erosion resistance of brittle and rubbery materials.

Unfortunately, this approach for deformation wear has no foundation in the theory of fatigue.

1.6 Mechanism (3): Target Melting

Equation 1.1 relates the loss of energy of the projectile to the energy required to form a new state of strain within the target. This energy is converted into heat which, when concentrated into a sufficiently small volume, could cause the target material to be melted.

Evidence in support of the theory that melting is a significant mechanism of mass loss in erosion is based almost exclusively on scanning electron microscopy examination (SEM) of the impact sites (Smeltzer, Gulden, McElmury, & Compton, 1970), (Jennings, Head, & Manning, 1976), (Yust & Crouse, 1978), (Gulden, 1979), (Shewmon, 1979), (Christian, 1979)

Although SEM is undeniably a valuable tool for examining damage sites it cannot provide quantitative results such as the temperature reached during an impact or how much material has been melted. This last point is surely the crux of the problem of the melting theory of erosion, and for this reason SEM examination must be interpreted with care.

Most of the authors quoted in this section have observed small *globules* of material in the impact crater “. . . whose form was clearly established by the effect of surface tension on liquid metal” (Shewmon, 1979). These globules are usually no more than one micron in diameter (Smeltzer, Gulden, McElmury, & Compton, 1970) they represent a volume 10^{-6} of that of a typical impacting particle and as little as 10^{-5} of the volume of material removed by the eroding particle (Hutchings, Winter, & Field, 1976).

In support of the theory of melting, it is very commonly observed in the abrading of metals that hot sparks fly from the abraded surface. These sparks have a temperature of at least 1300 K judging by their colour. Hutchings (Hutchings I. M., PhD Thesis, 1974) has observed surface oxide colouring inside impact craters in steel, which was produced by single, 9.5 mm diameter, hardened steel balls striking the steel surface in air.

Duvall and Graham (Duvall & Graham, 1977) review some of the present work on phase transition due to shock-wave loading. The results quoted by them are strictly applicable to hyper-velocity impact only (velocity $> 1000 \text{ ms}^{-1}$), but serve to illustrate the very considerable problems involved in detecting short-lived, first-order phase transitions. For the case of alloys and some elements there is the added possibility of polymorphic phase transitions. For example: $\alpha \leftrightarrow \epsilon$ Iron at 13 GPa and, in the case of non-metals, graphite \leftrightarrow diamond at 40 GPa. In the case of lead, Carter (Carter W. J., 1973) has shown the existence of homogeneous melting at 28 GPa and a temperature of 1210 K, which should be compared with the melting point of 600 K at a pressure of 0.1 MPa. Compare this pressure for melting with the yield stress of the metal, which is only 12 MPa. In addition, it may be that for the short-lived pressures encountered in impact (about 10^{-5} s and only 10^{-7} s for hyper-velocity impact) metastability of the solid phase may be possible at temperatures and pressures well in excess of their normal melting conditions.

Hutchings et al. (Hutchings, Winter, & Field, 1976) have estimated that a temperature of about 3000 K will be attained by a sub-surface shear band, frequently observed below impact craters; the so-called *adiabatic shear band*.

Davies (Davies, Proceedings of the Royal Society A (197), 1949) points-out that during a quasi-static, spherical indent on an ideally elastic-plastic surface (obeying the yield criterion of von Mises) the maximum shear stress occurs at a point below the point of maximum penetration of the sphere, at a

depth of roughly one half of the radius of contact between the sphere and the surface. It is at such a point of maximum shear where yield will most likely start. Winter (Winter, 1975) has shown in metal punching experiments that bands of intense shear start at a point below the punch and intersect with the surface of the metal. Winter and Hutchings (Winter & Hutchings, 1974) and Christian and Shewmon (Christian & Shewmon, 1979) have observed a similar band in their experiments with single steel balls. These bands appear to play a crucial role in the mechanism of material removal in such experiments.

Zener and Holloman (Zener & Holloman, 1944) first observed bands of intense shear in sections of highly deformed steel which appear white when etched with Picral or Nital. Wingrove (Wingrove, 1971) has confirmed that this white etching is due to the formation of Martensite, which is formed by quenching the Austenite phase of steel (in this case in the surrounding material presumably after the formation of the shear band). Austenite forms at temperatures above 1000 K, implying that a temperature rise of at least 730 K must have accompanied the formation of the shear band. Hartley et al. (Hartley, Jenkins, & Lee, 1979) predict that adiabatic effects will occur in any metal test with a strain-rate greater than 10^{-1} s^{-1} . Impacts have characteristic strain-rates of at least 10^5 s^{-1} .

It is interesting to note that it has been suggested that adiabatic shear bands form at the tool-tip in metal cutting (Horne, 1979), and therefore may be important in the micro-machining process envisaged by Finnie.

The exact conditions under which material removal may occur in connection with the formation of adiabatic shear bands are unknown at present. There is neither an erosion prediction based upon this mechanism nor is there a successful predictive theory for the mechanism of large-scale target melting.

1.7 The Effects of Temperature and Strain-rate

The motion of dislocations within a metal crystal can be activated either by stress or temperature. Increasing either quantity will cause dislocations to move more rapidly. Since plastic strain is accommodated within a metal by the motion of dislocations, it follows that the speed of straining will be controlled by both the magnitude of shear stress on the metal surfaces and the temperature.

$$\sigma = C \exp \frac{Q}{RT}$$

$$\varepsilon = \text{constant}, d\varepsilon/dt = \text{constant}.$$

Equation 1.6

Equation 1.6 represents a common expression for the thermal activation of dislocations, where σ = flow stress, Q = activation energy for plastic flow per mole, R = universal gas constant per mole, T = absolute temperature, C = constant, ε = true strain. Strain and strain-rate are held constant.

Zener and Holloman (Zener & Holloman, 1944) have adopted this idea, putting it into an equation for combined temperature and strain-rate dependence.

$$\sigma = f(Z)$$

$$\epsilon = \text{constant}$$

Equation 1.7

$$Z = \dot{\epsilon} \exp \frac{\Delta H}{RT}$$

Equation 1.8

Where Z is the Zener-Holloman parameter or the temperature-modified strain-rate. Equation 1.7 is not to be interpreted as a mechanical equation of state because the flow-stress depends on the dislocation structure within the metal which in turn depends on the history of the metal. In equation 1.8, ΔH is also the activation energy for hot working.

A commonly used relationship between flow-stress and strain-rate, $d\epsilon/dt$ or $\dot{\epsilon}$, at constant temperature and strain, is,

$$\sigma = D \dot{\epsilon}^m$$

$$\epsilon = \text{constant}, T = \text{constant}; m < 1.0$$

Equation 1.9

Where D is another constant. It can be shown that

$$Q = m\Delta H$$

Equation 1.10

The case of $m = 1$ represents a super-plastic material.

There are other equations which give a good representation of material behaviour.

Hutchings (1977) suggests that the strain-rate hardening can imply a size effect in erosion; small erosive particles must have a higher velocity for the onset of plastic deformation. Tilly (Tilly, 1973) also points out a critical velocity for erosion related to particle size. Goodwin et al. (Goodwin, Sage, & Tilly, 1969) have observed a linear decrease in erosion with particle size from 100 μm to 5 μm , with a possible cut-off size at 5 μm for which erosion does not occur at velocities below 300 ms^{-1} .

By way of contrast, the dependence of erosion on temperature is by no means certain. Thermal softening of the target will certainly take place when the temperature is raised, in some cases the material (metal, ceramic or mineral) may transform from exhibiting brittle to ductile behaviour, e.g. mild steel at 268 K. However, there is no consensus as to how either thermal softening or the ductile-brittle transition will affect erosion. Ives (Ives, 1977) reports an average increase of erosion by a factor of ten upon heating stainless steel from room temperature to 975°C, his experiments were performed using a chemically active gas stream containing silicon carbide particles. Young and Ruff (Young & Ruff, 1977) have observed both a decrease of the angle of impingement causing peak erosion and an overall decrease of erosion by a factor of more than ten when raising the test temperature from room temperature to 500°C. This effect was observed for a wide range of

materials and erosive particles. The carrier gas Young and Ruff used was carbon dioxide. Clearly the carrier gas used in such experiments may have a very important effect on the erosion rate.

Klueh and Oakes (Klueh & Oakes, 1977) have drawn surfaces of yield strength as a function of temperature (300 to 840 K) and strain-rate ($2.7 \times 10^{-6} \text{ s}^{-1}$ to 144 s^{-1}) for a Bainitic Cr-Mo Steel. These surfaces, although smooth, possess maxima, minima and saddles.

1.8 Aerodynamic and Geometric Effects

Any particle in motion with, or against, a fluid will experience a viscous force. This force is strongly dependent upon the particle shape and the viscosity of the fluid. The Reynold's number, R , is constant for similar flow fields.

$$R = \frac{\rho v a}{\mu}$$

Equation 1.11

Where v = flow velocity, a = radius of the particle, ρ = density of the fluid and μ = viscosity.

If a different size of particle is used in an erosion test the result will be a different flow field, unless one of the parameters in equation 1.11 is altered to compensate. This may alter the average angle of impingement of the particles onto the target; for very small particles ($\sim 5 \mu\text{m}$) the impingement angle may become very small (grazing incidence), in which case the erosion will be very much reduced.

Hutchings (Hutchings I. M., PhD Thesis, 1974) studied the problem of scaling the volume of single impact craters according to particle size, a , density, ρ' , and velocity v . He shows that the crater volume, V , will depend on these parameters and impingement angle, n , in the following way.

$$V(a, \rho', v, \alpha) = a^3 f(\alpha) g(\rho', v^2)$$

Equation 1.12

Where $f()$ and $g()$ are unspecified functions.

Carter et al. (Carter & Nobes, 1979) have applied Slowness theory to solve specific erosion problems involving geometry, for example: eroded profiles of pipe bends, tubes and plates. Slowness theory uses as an empirical basis the curve of erosion against impingement angle (see Figure 1.1) and goes on to deduce the steady-state erosion profile. This approach is useful for indicating likely failure points of eroding structures.

1.9 Prediction of Erosion Resistance

Predictions of erosion fall into three categories:

- (a) Empirical or heuristic.
- (b) Mechanistic or mechanistic/empirical.

(c) Target material based.

This chapter has so far concentrated exclusively on predictions of the kind (a) and (b). There are several theories of type (c).

Hutchings (Hutchings I. M., 1975) suggests that for metals the product of the target material specific heat, C , density, ρ , and temperature change, ΔT , required to melt the metal is a good guide to the erosion resistance (see Figure 1.6).

$$\text{Erosion resistance} \propto C\rho\Delta T$$

The rationale behind this theory is the idea of susceptibility to adiabatic shear (see section 1.7). The product, $C\rho\Delta T$, represents the energy required to heat unit volume of the metal up to the melting point. The objections to this theory are that it is still not clear how adiabatic shear influences the process of chip detachment in ploughing impacts, adiabatic shear has not been observed for micro-machining angular particles, the theory takes no account of latent heat of melting, it does not consider the strain history of the metal, and it cannot account for the observation that some materials exhibit reduced erosion at higher temperatures (Young & Ruff, 1977).

Ascarelli (Ascarelli, 1971) has suggested that the *thermal pressure parameter*, $\beta K\Delta T$, gives a good prediction of erosion resistance.

$$\text{Erosion resistance} = \beta K\Delta T$$

Where ΔT has already been defined, K is the coefficient of linear thermal expansion of the metal and β = bulk modulus. The reasoning behind this proposal is that although the theory of plasticity may describe the mechanism of formation of the crater it is the ability of the metal to withstand melting that is important in preventing any loss of molten material during the impact. The pressure resisting compression, produced when the metal reaches its melting point, is $\beta K\Delta T$. If the metal has a large value of this product then it will be less liable to melt (see Figure 1.7). The objections to this proposal are that melting has not been demonstrated as a dominant mechanism of erosion and this theory, in common with that of Hutchings, cannot predict increased erosion resistance at elevated target temperatures.

Vijh (Vijh, 1976) relates the value of metal-metal bond energy, $b(M - M)$, with increased erosion resistance (see Figure 1.8). Apparently this correlation is a good indication of general wear resistance and resistance to electric arc erosion (Vijh, 1978). The magnitude of the bond energy is related to the heat of sublimation of the metal, ΔH_s , and the bulk coordination number, C_N , by the following

$$b(M - M) = \frac{2(\Delta H_s)}{C_N}$$

Vijh (Vijh, 1975) suggests that the melting temperature is also a good, general index of the metal's erosion resistance and Smeltzer et al. (Smeltzer, Gulden, McElmury, & Compton, 1970) confirm this. This last suggestion is also a feature common to the proposals above of Hutchings and Ascarelli. It may be that this is the underlying feature of all three proposals.

Other suggestions for erosion prediction have been based upon either the indentation hardness of the metal or the elastic modulus. Finnie (Finnie I., 1972) and Tilly (Tilly, 1969) have examined the veracity of the former claim and shown at best only limited correlation, whilst Tuit (Tuit, 1974) has noted some correlation between erosion resistance and elastic modulus.

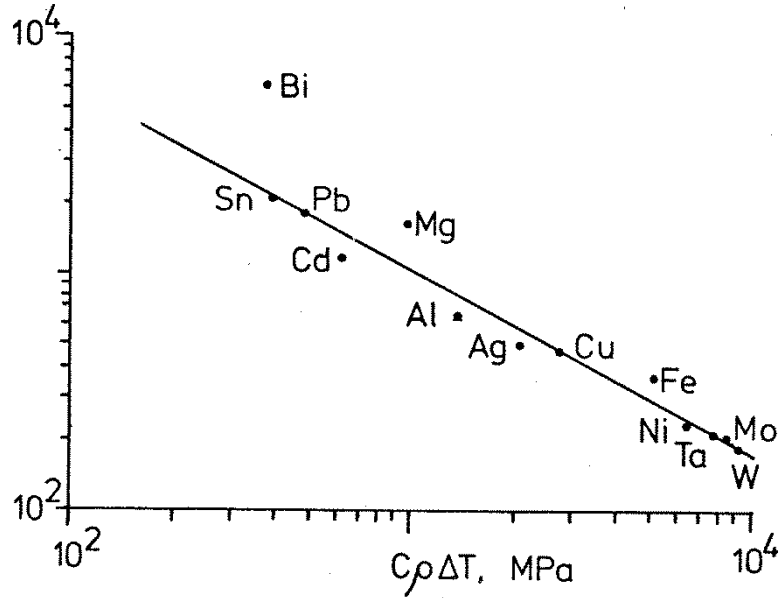


Figure 1.6

Erosion resistance prediction: Hutchings' $C_p\Delta T$ factor plotted against volume erosion rate.

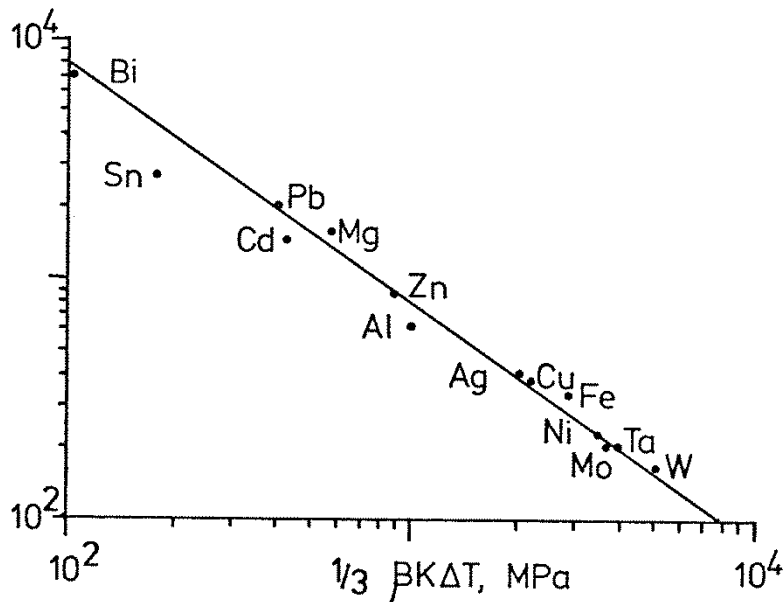


Figure 1.7

Erosion resistance prediction: Ascarelli's $\beta K\Delta T$ factor plotted against volume erosion rate.

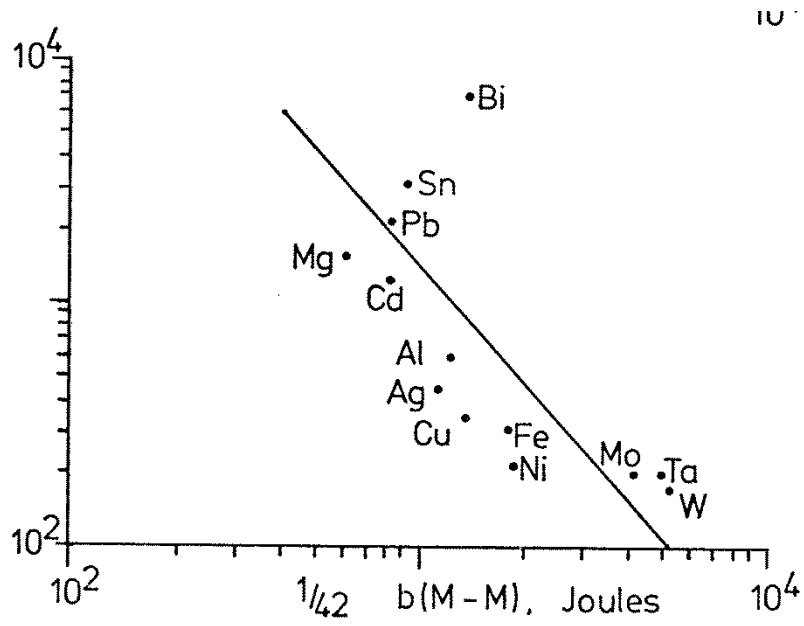


Figure 1.8

Erosion resistance prediction: Vijh's metal-metal bond energy plotted against volume erosion rate.

Erosion data for all three figures 1.6, 1.7 and 1.8 comes from a common reference source: Finnie, Wolak and Kabil, (Finnie, Wolak, & Kabil, Journal of Materials (2), 1967). The erosion particles were SiC travelling at a velocity of 136 ms^{-1} . Erosion loss is in mixed units: $(\text{mm})^3 \text{ kg}^{-1}$.

Chapter 2 Aims of This Work and Theory

2.1 General Aims

It appears that there are three plausible mechanisms of erosion.

1. The cutting mechanism (models of Finnie and Hutchings), which has been observed to occur in single impacts and which is capable of predicting two of the characteristic erosion relations: the peak in the curve of erosion versus impingement angle and the velocity dependence of erosion.
2. The target melting mechanism (as proposed by Smeltzer, Gulden and Shewmon), which has only been inferred from scanning electron microscopy observation of impact sites and which has not yet been able to predict erosion in any quantitative way.
3. The fatigue mechanism, which has an intuitive appeal but has not been used to predict erosion except in a loose fashion by Bitter.

There appear to be two broad areas in need of clarification, namely:

(a) The statistical nature of erosion.

(b) The degree to which melting is important in single impacts. These points will be discussed in more detail in the following sections.

2.2 (a) Statistical Nature of Erosion - I

Finnie and Hutchings and their co-authors have proposed that erosion is produced by either the cutting or ploughing of hard particles into the surface of ductile metals. Finnie has shown that this mechanism can successfully predict the peak of erosion at approximately 20° impingement angle. Hutchings looked at the shape of the particle and how this can influence the crater it produces during impact, and found that spherical particles can plough the surface, raising a lip of material which can become detached under certain circumstances. A spherical particle is certainly not the kind of particle upon which Finnie based his cutting analysis but, paradoxically, Hutchings found that single spherical particles also produce a maximum mass loss at impingement angles of about 20° (Hutchings, Winter, & Field, 1976) - see Figure 2.1. Hutchings has also studied angular particles and shown that the rotation of particles during impact is important; particles which rotate backwards machine a chip out of the surface, whereas particles rotating forwards only seem to raise a lip which is quite firmly attached to the target.

There is not yet any way of predicting what proportion of a given erosive sample will produce either ploughing damage, or forward or backward rotation deformation on impact. One of the aims of this work will be to study the correlation between an index of shape and the proportion of impacts belonging to each of the three categories for a variety of eroding grits.

2.3 (b) The Importance of Target Melting

The theory of target melting has many advocates in the literature on erosion, but none of them has been able to predict either the erosion peak at impingement angles of 20° or a velocity dependence of erosion with exponent greater than 2.0. In addition, there has been no direct evidence that melting takes place during impact other than observations from metal grinding and inferences from scanning electron microscopy of impact sites.

It would seem likely that some metals are more likely to melt than others during high strain-rate loading. The susceptibility of a metal to melting is not easy to gauge because it will depend upon the concentration of the strain field around the crater and how much energy is required to melt unit volume of metal. I suggest that it is possible to estimate the susceptibility using the following argument.

In Chapter 1, a simple theory of erosion was developed resulting in equation 1.2. This theory equates the loss of energy of the projectile to the energy, PV , required to produce the strain field around the crater of volume V . The indentation hardness of the metal is P which equals roughly $3\sigma_y$ where σ_y is the yield stress of the metal. Nearly all of the energy producing the strain field will be converted into heat, resulting in a temperature rise, ΔT , within some volume around the crater. If this volume is set equal to some proportion, γ , of the crater volume, and it is assumed that the temperature rise is uniform throughout this volume, then we can equate the work done to the gain in thermal energy.

$$3\sigma_y V = \rho \gamma C \Delta T$$

Equation 2.1

Where ρ and C are the target density and specific heat respectively.

If the test temperature of the target is T_a and its melting point is T_m then it is possible to re-write equation 2.1 in terms of a homologous temperature ($\vartheta = T/T_m$)

$$\theta = \frac{1}{T_m} \left\{ \frac{3\sigma_y}{\rho C} \frac{1}{\gamma} + T_a \right\}$$

Equation 2.2

In Figure 2.2 families of ϑ versus γ curves are plotted for one metal at various ambient temperatures (data for these plots are obtained from Smithells (Smithells, 1962)). Equation 2.2 constrains all of such curves to be rectangular hyperbolae, however, they all show that each metal will reach $\vartheta = 1.0$ with some values of γ and there is a monotonic increase of this critical γ with increasing test temperature - this is not surprising. Table 2.1 shows that certain metals will reach the melting point with relatively larger values of critical γ for a given initial temperature, for example, strong nickel alloy at 300K.

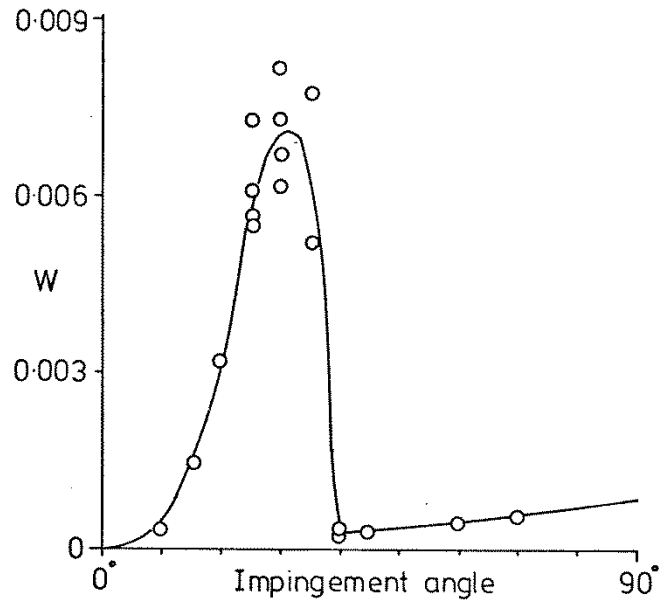


Figure 2.1

Variation mass loss/mass of impacting sphere with angle of impingement for 9.5 mm steel spheres striking steel at 270 ms-1 (Hutchings, Winter, & Field, 1976).

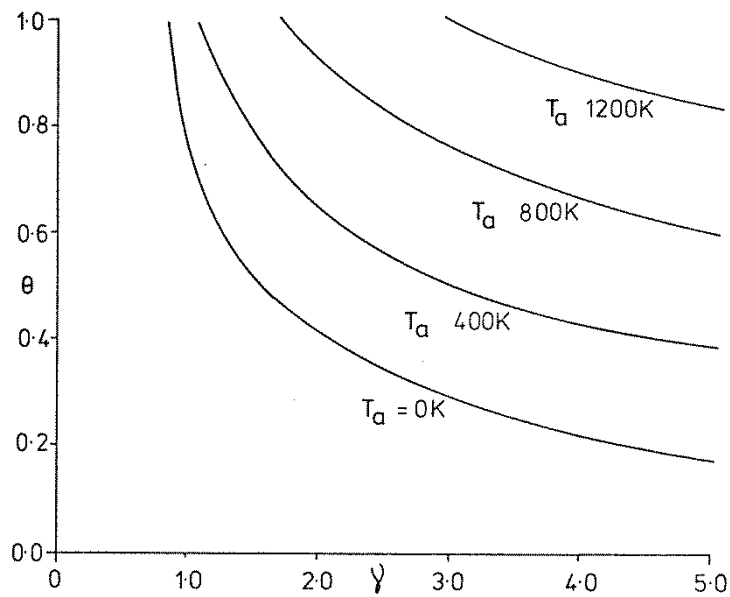


Figure 2.2

Variation of homologous temperature rise, θ , which results from a single impact, with γ the crater volume factor. The plot is for a range of ambient target test temperatures, T_a , for a strong nickel alloy.

The following list of materials has been made in descending magnitude of γ . A large value of γ indicates that the material can lose a larger amount of material by melting as a proportion of the

impact crater volume. Therefore, a low value of γ implies that the material is relatively more resistant to erosion by melting.

Material	γ , Proportion of crater volume heated (Temperature = 300 K)	γ , Proportion of crater volume heated (Temperature = 1300 K)
Strong nickel alloy	1.09	4.3
Titanium	0.37	
Bismuth	0.29	
Mild steel	0.19	1.17
Stainless steel	0.11	
Gold	0.08	
Copper	0.06	0.68

Table 2.1 Susceptibility to Melting

This kind of calculation has its limitations and I do not suggest that any quantitative significance should be attached to the numerical values of γ which have been obtained. However, I do suggest that by listing the metals according to their value of critical γ at a given temperature it is possible to assess their relative susceptibility to melting during impact.

It must be conceded by the advocates of the melting theory of erosion that cutting does occur in erosion - this fact has been well established. What remains obscure is the conditions under which melting becomes important. It may be the case that melting accounts for a negligible mass loss when compared to the mass lost by cutting. If the melting hypothesis is to become established then research should be directed towards examining the temperature dependence of erosion, and in particular towards the study of single particle impacts at high temperatures on metals like the strong alloys of nickel (for example: Inconel, Nimonic). It is interesting to note here that the Nimonic alloys (produced by Messrs. Henry Wiggin) are used in the turbine stages of gas turbine aero-engines because of their strength at high temperature, yet it would seem that it is their high strength that is responsible for producing the concentrated strain fields necessary for melting to occur. This paradox is exacerbated when one considers that one of the mechanical properties of this alloy is its good erosion resistance; perhaps the solution to this conundrum is that these alloys are so resistant to erosion by cutting that it is now only possible to observe the effects of erosion by melting.

A few experimental and theoretical estimates have been made of the temperature rise accompanying impact by single particles, these range from 800°C to 3000°C. Is it correct to assume that the melting temperature of the target metal remains constant while it is being impacted? The Clausius-Clapeyron equation relates the change in melting point with the hydrostatic stress in the following way:

$$\frac{dT}{dP} = \frac{\Delta V}{\Delta S} = \frac{T_m \Delta V}{L}$$

where ΔV is the volume change on melting, L is the latent heat of fusion, and T_m is the melting temperature under conditions of zero hydrostatic pressure. Thus the homogeneous melting temperature T'_m is a function of hydrostatic stress, σ_o , in the following way:

$$T'_m = T_m \left\{ 1 + \frac{\Delta V}{L} \sigma_o \right\}$$

Equation 2.3

For most metals $\Delta V > 0$, $\Delta S > 0$ during melting, exceptions to this are bismuth, gallium, germanium and silicon, none of which shows very good resistance to erosion (some of these are shown in Figures 1.6, 1.7 and 1.8). Bismuth was the least resistant to erosion of all the metals studied by Finnie et al (Finnie, Wolak, & Kabil, Journal of Materials (2), 1967). Bismuth, in addition to possessing $\Delta V < 0$ on melting, also has a fairly low melting temperature (544 K) and this may play a dominant role in its erosion resistance at room temperature.

Values of ΔV and L are well tabulated, for example Smithells (Smithells, 1962), however, there are no good estimates of the hydrostatic pressure generated in a target during impact. It is possible to make a rough calculation of a representative range of values. In an indentation experiment it is well known that the mean pressure applied to the indenter, P , is equal to approximately three times the yield stress, σ_y , that is $P = 3 \sigma_y$. This is because about two-thirds of the applied pressure goes into creating a hydrostatic component of stress, σ_I .

It follows that for a given metal

$$\sigma_I \cong 2\sigma_y$$

Equation 2.4

If a spherical projectile of mass m , travelling at velocity v , strikes a target and rebounds with velocity $-v$ in a time Δt , and if the radius of the sphere is r , then the average pressure σ_d , experienced by the target under the sphere will be given by the following expression:

$$\sigma_d = \frac{2mv}{\pi r^2 \Delta t}$$

Equation 2.5

The hydrostatic pressure generated during impact will be bounded below by equation 2.4 whilst equation 2.5 can be turned into an upper bound by substituting an extreme value of v (say, 500 ms^{-1}). In the case of copper, $\sigma_I = 150 \text{ MPa}$. For a 5 mm diameter hardened steel ball travelling at 500 ms^{-1} the impact duration is about $100 \mu\text{s}$ (Tabor, 1951), from which it can be calculated that $\sigma_d = 250 \text{ MPa}$.

The Clausius-Clapeyron equation 2.3 predicts

$T'_m = 1.005 T_m$ for copper, in the case of impact, and $T'_m = 1.003 T_m$ in the case of quasi-static indentation. The range of values of T'_m for copper is typical of the metals, which is of the order of 2°C to 10°C . In the hyper-velocity range ($>1000 \text{ ms}^{-1}$) the Clausius-Clapeyron effect becomes important. Under such conditions a full treatment involving Hugoniot curves would become necessary (Duvall & Graham, 1977).

The foregoing analysis shows that under the conditions of erosion described in this work it is a good approximation to assume that the melting temperature is constant. In subsequent chapters I will discuss the behaviour of mild steel, copper, titanium, Nimonic alloy (Ni-Cr based strong alloy) and bismuth under conditions of impact by single ball bearings over a wide range of their homologous temperatures.

Since melting metal requires energy and in erosion the only source of energy is the kinetic energy of the impacting particle, it seems logical to assume that target melting will be most likely to occur when the transfer of energy from the particle to the target is a maximum - this will be under conditions of high velocity and normal impact. It seems reasonable to assume that the dependence of energy transfer on impingement angle will be roughly sinusoidal over the range $0^\circ \leq \alpha \leq 90^\circ$. Hutchings et al. (Hutchings, Winter, & Field, 1976) have studied the variation of target mass loss with impingement angle (see Figure 2.1) for impact by spheres. There is a strong peak in this curve at about 20° but the peak falls away abruptly at 40° ; over the range $40^\circ < \alpha < 75^\circ$ there is a small monotonically increasing mass loss which presumably continues on to $\alpha = 90^\circ$ - it may be that this is a contribution arising from melting.

Hutchings (Hutchings I. M., PhD Thesis, 1974) has also studied normal indentation craters arising from both standard quasi-static loading and dynamic impact. He observed in sectioned specimens a marked difference between the strain fields in the two cases. In the case of dynamic impact a fine coronet of target metal was extruded around the side of the ball in a manner reminiscent of the coronet formed when a liquid drop falls onto a flat liquid surface. I will describe at a later stage a set of experiments to study this phenomenon using high-speed photography.

It is my hope that these studies will demonstrate target melting is an important mechanism of erosion. If impact by single particles can cause the target to melt then it is likely that bombardment by many particles will also cause melting.

The role of adiabatic shear in target melting is unresolved. Winter and Hutchings (Winter & Hutchings, 1975) and Hutchings (Hutchings I. M., 1975) have observed subsurface bands of intense shear under the impact craters of spheres and around punched holes in metals. They suggest that these bands are the result of localised heating or adiabatic shear. Apparently adiabatic shear is common in high-strain rate deformation, however, it is difficult to prove the existence of adiabatic shear. It is also uncertain how adiabatic shear, which is commonly associated with localised bands of intense shear, can be connected with melting over a large volume.

Bismuth had the lowest resistance to erosion of all the metals and alloys tested by Finnie et al. (Finnie, Wolak, & Kabil, Journal of Materials (2), 1967). Bismuth has one unusual thermal property: when it melts its volume decreases. It is unlikely that this has any significant effect upon its erosion properties or its susceptibility to melting. It will be of interest to discover why bismuth has poor resistance to erosion.

2.4 (a) Statistical Nature of Erosion - II

Various authors, including Bitter (Bitter, 1963), Hutchings (Hutchings I. M., 1979) have attempted to relate erosion to the continuous bombardment a target receives during impact. This view of the cooperative effect of impact has given rise to its own mechanisms of wear, sometimes known as *deformation wear* or erosion by fatigue. The following section describes a statistical analysis of erosion, which would seem to be called for in view of the very large number of particles responsible for erosion.

A flux, F , of erosive particles, each particle of average cross-sectional area σ , streams out of an orifice of cross-sectional area A and subsequently erodes a target. It is assumed that the particles all travel at the same velocity and in a direction perpendicular to the plane of the cross-sectional area of the orifice. The flux, F , is measured in units of $\text{kg m}^2 \text{s}^{-1}$.

If the average mass of an eroding particle is m then the number striking the target per second, κ , is given by,

$$\kappa = \frac{FA}{m}$$

Equation 2.6

The area of the target surface which will be eroded is $A/\sin(\alpha)$, where α is the angle of impingement. When a single particle strikes the target it will produce a strain field of an approximate surface area $\sigma/\sin(\alpha)$.

$$\text{Characteristic area of a single impact} = \sigma/\sin(\alpha)$$

Equation 2.7

The target surface may be considered to consist of a number of impact zones each of characteristic area given by equation 2.7.

$$\text{Number of impact zones} = A/\sigma$$

Equation 2.8

The average number of particles striking a given impact zone in unit time is given by κ_z

$$\kappa_z = \frac{F\sigma}{m}$$

Equation 2.9

The probability that a given impact zone will receive r impacts in the time interval $[0,t]$ is given by the Poisson distribution. It is assumed that the probability of an impact occurring in a small time interval $[t_1, t_1 + \delta t_1]$ is $\kappa_z \delta t_1$ and it is certainly true that this probability is unaffected by the pattern of events before t_1 . If we choose δt_1 to be sufficiently small ($\delta t_1 \ll 1/\kappa_z$) then the probability of two or more impacts occurring during the interval is negligible. It follows that under these conditions the timing of impacts will be described by the Poisson distribution. Lastly, let us assume that the eroded

area is composed of A/σ non-interacting impact zones. The probability of r impacts occurring on a given zone in a time interval $[0,t]$ is given by

$$P(r \text{ impacts}) = \frac{(\kappa_z t)^r}{r!} \exp^{-\kappa_z t}$$

Equation 2.10

The next stage in the argument is less well-founded. If it is possible to equate mass loss, z , to the number of impacts occurring in $[0,t]$ then it will be possible to calculate the expected mass-loss in the usual manner of statistics. However, it is not possible to equate mass loss to the number of impacts with any degree of confidence, and it is at this stage that the reasoning must become hypothetical. Consider the following three possibilities (i), (ii) and (iii):

(i)

$$z = m_c r$$

Equation 2.11

a linear relationship between mass loss and the number of impacts.

It is this kind of relationship that might be expected from a theory which takes no account of target material properties, for example: strain hardening, thermal conduction, thermal expansion, melting temperature. The mass of material removed per impact is m_c .

The expected mass loss from one zone follows directly from the property of the mean of the Poisson distribution.

$$\text{Expected mass loss per impact zone} = m_c \kappa_z t$$

The expected mass loss from the whole of the eroded area follows directly.

$$\text{Total expected mass loss} = FA \frac{m_c}{m} t$$

Equation 2.12

(ii)

$$z = m_s r^{1/p}$$

Equation 2.13

where p is a constant.

This relationship between mass loss and the number of impacts is the kind that might be expected from a strain-hardening metal with infinite strain-hardening ability when $p > 1$. In this case the total expected mass loss from the target will be

$$\text{Total expected mass loss} = A \frac{m_s}{\sigma} \exp^{-\kappa_z t} \sum_{r=0}^{\infty} r^{1/p} \frac{(\kappa_z t)^r}{r!}$$

Equation 2.14

The infinite series of equation 2.14 is certainly convergent for all values of p (ratio test on successive terms). Figure 2.3 shows equation 2.14 plotted for various values of p . In the case of $p = 1$ the curve becomes linear and is identical to the form of equation 2.12; in all other cases it is non-linear. The curves are strongly dependent upon the value of p .

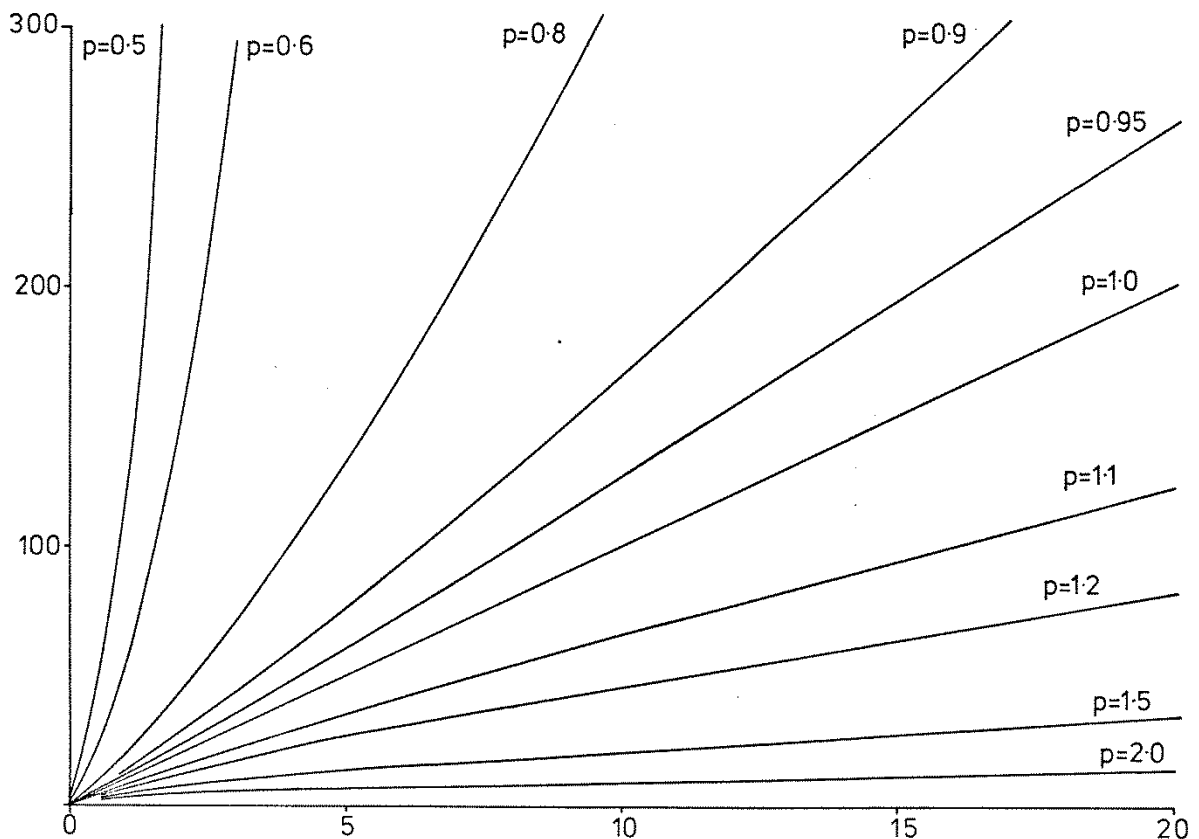


Figure 2.3

Plot of the important part of the function in equation 2.14.

The function plotted against time, t , in figure 2.3 is

$$\exp^{-\kappa_z t} \sum_{r=0}^{\infty} r^{1/p} \frac{(\kappa_z t)^r}{r!}$$

(31)

(iii)

$$\begin{aligned} z &= m_t(r - r_o) && \text{for } r > r_o \\ z &= 0 && \text{for } r \leq r_o \end{aligned}$$

Equation 2.15

Where r is a threshold number of impacts which must occur during the interval $[0,t]$ to raise the temperature of a surface layer of the target to its melting point, T_m . Under conditions of melting the cohesive forces of the target surface are very small and it will be possible to remove material at a much greater rate than if the target temperature was lower than T_m .

It is straightforward to calculate the expected mass loss from the target.

$$\text{Total expected mass loss} = A \frac{m_t}{\sigma} \exp^{-\kappa_z t} \sum_{r=r_o}^{\infty} (r - r_o) \frac{(\kappa_z t)^r}{r!}$$

Equation 2.16

Note the change in the lower limit in the summation. The value of this sum is strongly dependent on the relative values of r_o and $\kappa_z t$. Two cases arise, namely:

- (a) $\kappa_z t < r_o$
- (b) $\kappa_z t \geq r_o$

Figure 2.4 is a schematic representation of these two cases. Unless $\kappa_z t \geq r_o$ that is case (b), the probability of there being $r > r_o$ impacts in $[0,t]$ will be very small and therefore the probability of the target surface melting will be correspondingly small. Clearly it is important to know r_o or, more correctly, r_o/t for it is the frequency of impacts which is important. Before examining in detail this frequency, which is essentially the limiting case of $t \rightarrow \infty$, it should be noted that there will also be no melting in the limit of $t \rightarrow 0$ even when $\kappa_z \geq r_o/t$. This is because the temperature of the target surface must first be raised to the melting temperature from the ambient temperature, T_a . Thus two new effects emerge from considering the target melting model of erosion: a threshold frequency of impacts (and therefore a threshold flux) and an incubation time. Material removal by target melting is unlikely to occur unless both the threshold flux and the incubation time have been exceeded. To combine these two effects it is necessary to have a formula for r_o

$$r_o = r_1 + \omega t$$

Equation 2.17

In which r_1 is a threshold number of impacts and ω is a threshold frequency of impacts.

Now

$$\lim_{t \rightarrow 0} r_o = r_1$$

$$\lim_{t \rightarrow \infty} \frac{r_0}{t} = \omega$$

Unfortunately, both r_1 and ω are likely to be dependent upon several variables, for example: particle size and thermal and mechanical properties of the target.

The following discussion concerns the temperature profile beneath an impact zone resulting from a pulsed input of heat. From the analysis it is possible to relate the heat generated by impact and certain material properties to the threshold frequency and incubation time for target melting to become important.

Consider the target beneath one impact zone. Let the target be of thickness L , with a coordinate system set up along its thickness, $0 < x < L$. A single impact zone will be a small part of the plane $x = 0$. Let the target and the environment at its surfaces be initially at temperature T_0 . It is assumed that neighbouring impact zones are thermally non-interacting, which is likely to be a good approximation on average - this is equivalent to there being no heat transfer between adjacent zones. Neglecting perimeter edge-effects of the target, the heat diffusion equation in one dimension will apply to every zone.

$$\frac{\partial T}{\partial t} = \beta \frac{\partial^2 T}{\partial x^2}$$

$$0 = < x = < L$$

where $\beta = K/C\rho$, K = thermal conductivity of the target, C = specific heat capacity per unit mass, ρ = density and $T(x,t)$ = temperature at time t and point x . This equation can be solved for the radiation-type of boundary conditions (Carslaw and Jaeger (Carslaw & Jaeger, 1947).

$$-\frac{\partial T}{\partial x} + h(T - T_0) = 0$$

$$\text{At } x = 0$$

$$\frac{\partial T}{\partial x} + h(T - T_0) = 0$$

$$\text{At } x = L$$

where $h = H/K$, H = radiation constant. Note these conditions are not black-body radiation conditions which are non-linear conditions of the form:

$$\pm \frac{\partial T}{\partial x} + h'(T^4 - T_0^4) = 0$$

It is more difficult to find an analytic solution in this case, however, in the limit of $T \rightarrow T_0$

$$\lim_{T \rightarrow T_0} h'(T^4 - T_0^4) = 4h'T_0^3(T - T_0) = h''(T - T_0)$$

Where h' and h'' are constants. Proceeding with the linear boundary conditions and assuming the initial condition

$$T(x) = f(x)$$

The solution is the following:

$$T(x, t) = 2 \sum_{n=1}^{\infty} \exp^{-\beta \alpha_n^2 t} \left\{ \frac{(\alpha_n \cos(\alpha_n x) + h \sin(\alpha_n x))}{(\alpha_n^2 + h^2)L + 2h} \right\} \int_0^L f(\xi) (\alpha_n \cos(\alpha_n \xi) + h \sin(\alpha_n \xi)) d\xi + T_o$$

where α_n are roots of the transcendental equation

$$\tan(\alpha_n L) = \frac{2\alpha_n L}{(\alpha_n^2 - h^2)}$$

excluding $\alpha_n = 0$.

The plastic deformation under a zone resulting from a single impact generates a temperature profile beneath that zone. The impacting particle will have a representative size, $\nu\sigma$ (see equation 2.7). In general the duration of an impact is so short that there is negligible heat flow within that time. In most examples of erosion $\nu\sigma \ll L$ and a simple form of $f(x)$ is the following:

$$f(x) = T'$$

$$\text{for } 0 < x \leq \nu\sigma$$

$$f(x) = 0$$

$$\text{for } \nu\sigma < x \leq L$$

Equation 2.18

Now the modified Fourier coefficients in equation 2.17 can be calculated

$$T(x, t) = 2T' \sum_{n=1}^{\infty} \exp^{-\beta \alpha_n^2 t} B_n(x) + T_o$$

where

$$B_n(x) = \frac{(\alpha_n \cos(\alpha_n x) + h \sin(\alpha_n x))}{(\alpha_n^2 + h^2)L + 2h} \left\{ \sin(\alpha_n \nu\sigma) - (\cos(\alpha_n \nu\sigma) - 1) h/\alpha_n \right\}$$

If impacts occur at a frequency $1/\lambda$ then the temperature profile as a result of m impacts is the sum of similar contributions:

$$T(x, t) = 2T' \sum_{p=0}^m \sum_{n=1}^{\infty} \exp^{-\beta \alpha_n^2 (t-p\lambda)} B_n(x) + T_o$$

Equation 2.19

Reversing the order of summation and using the results for a geometric progression it is possible to simplify equation 2.19.

$$T(x, t) = 2T' \sum_{n=1}^{\infty} \exp^{-\beta\alpha_n^2(t-m\lambda)} \left\{ \frac{(1 - \exp^{-\beta\alpha_n^2 m\lambda})}{(1 - \exp^{-\beta\alpha_n^2 \lambda})} \right\} B_n(x) + T_o$$

Equation 2.20

It is understood that

$$m\lambda \leq t < (m + 1)\lambda$$

In the limit of $t \rightarrow \infty$ and hence $m \rightarrow \infty$

$$T(x, t) \rightarrow 2T' \sum_{n=1}^{\infty} \exp^{-\beta\alpha_n^2(t-m\lambda)} \left\{ \frac{1}{(1 - \exp^{-\beta\alpha_n^2 \lambda})} \right\} B_n(x) + T_o$$

Equation 2.21

To find the minimum frequency of impacts able to produce melting it is necessary to solve (21) for $t = m\lambda$, $T = T_m$ somewhere inside $0 < x < \sqrt{\sigma}$ that is solve for λ in

$$\frac{T_m - T_o}{2T'} = \sum_{n=1}^{\infty} \frac{B_n(0.5\sqrt{\sigma})}{(1 - \exp^{-\beta\alpha_n^2 \lambda})}$$

Equation 2.22

Here $x = 0.5\sqrt{\sigma}$ has been substituted which will be a sufficiently accurate estimate of the position of maximum temperature rise; it is tedious to find this point by solving $\frac{\partial T}{\partial x} = 0$ for x . Unfortunately, convergence is slow in equation 2.22 because the n^{th} term of the series, in the limit of $n \rightarrow \infty$ looks like

$$\lim_{n \rightarrow \infty} n^{\text{th}} \text{ term} \sim \frac{1}{n\pi} \cos\left(\frac{n\pi\sigma}{2L}\right) \sin\left(\frac{n\pi\sigma}{2L}\right)$$

Figure 2.5 shows the right hand side of equation 2.22 plotted against λ for chosen values of thermal constants and for a range of radiation constants h .

If an eroding stream of particles has an impact frequency κ_z which exceeds the critical frequency then erosion by melting will commence after an incubation time. The Poisson distribution allows for the possibility of erosion by melting to commence before any given finite time, so the use of the word *commence* must be interpreted as meaning on average, that is where melting occurs over the majority of the impact zones. To find this incubation time set $t = m\lambda$, $x = 0.5\sqrt{\sigma}$ and solve equation 2.20 for m with $T = T_m$ that is

$$\frac{T_m - T_o}{2T'} = \sum_{n=1}^{\infty} B_n(0.5\sqrt{\sigma}) \frac{(1 - \exp^{-\beta\alpha_n^2 m\lambda})}{(1 - \exp^{-\beta\alpha_n^2 \lambda})}$$

Equation 2.23

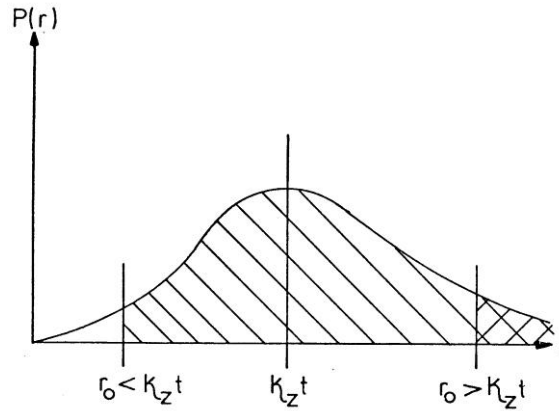


Figure 2.4

Sketch of the Poisson probability distribution ($P(r)$). The mean of the distribution is $k_z t$. If $r_0 > k_z t$ then the probability of melting is low. If $r_0 < k_z t$ then the probability of melting is high because the total probability of melting is the integral

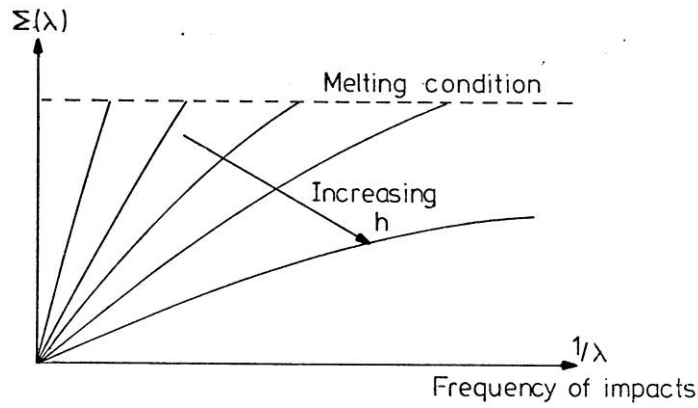


Figure 3 Variation of $\Sigma(\lambda)$, which is a measure of the target sub-surface temperature, against $1/\lambda$ the frequency of impacts. h is the radiation constant governing the rate of loss of heat from the target surfaces.

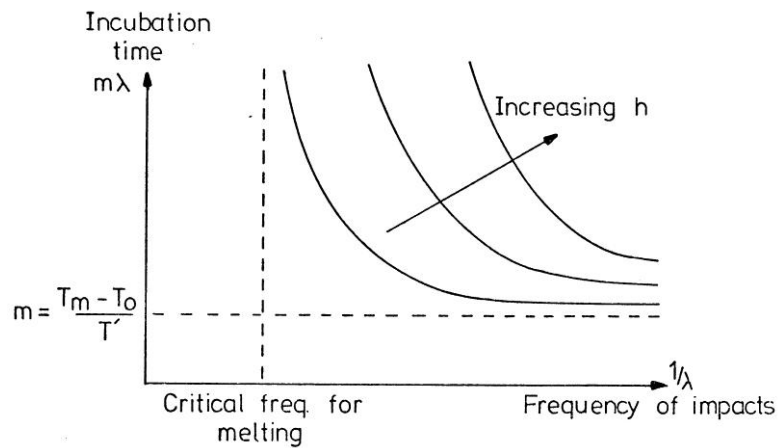


Figure 2.6

Variation of the incubation time ($m\lambda$), the time before target melting commences, plotted against the frequency of impacts ($1/\lambda$). The asymptotes of the plot are shown.

Figure 2.6 shows the variation of incubation time with impact frequency $1/\lambda$. These curves have asymptotes which are the critical frequency for melting and the minimum number of impacts to produce melting assuming no heat conduction or radiation.

It is not always possible to insert values of T' and $v\sigma$ into equations 2.20 to 2.23 with great confidence. $v\sigma$ corresponds to the characteristic size of the impacting particles, however, T' can only be deduced. The energy lost ΔE , by an impacting particle per impact can be equated to

$$\Delta E = \rho C T' \sigma^{3/2}$$

Equation 2.24

Hutchings (Hutchings I. M., PhD Thesis, 1974) has indicated how to scale impacts according to particle size and velocity. In principle, therefore, it is possible to calculate T' for a single impact. Results detailed in Chapter Four of this work show that T' is of the order of 200°C for a copper target at an ambient temperature of 900°C impacted by a 5 mm diameter steel sphere travelling at 130 ms^{-1} .

The parameter h is critical in determining the frequency for the onset of melting, however, for every value of h there exists a frequency of impact which will initiate melting. In the limit of $h \rightarrow 0$ the boundary condition becomes one of no heat flow across the ends; this is unlikely to be the case except for the erosion of low melting point materials (for example plastics) under vacuum conditions. In the limit of $h \rightarrow \infty$ the boundary condition becomes $T = T_o$ at the ends $x = 0, x = L$. Under usual erosion conditions the erosive jet will be propelled by a gas and, therefore, forced-convection will take place at the eroded surface. Unfortunately, the rate of heat loss by forced-convection is controlled by several factors, including: gas velocity and surface roughness, and it is not possible at this stage to give typical values of h for a prescribed set of conditions.

Figure 2.7 shows equation 2.16 plotted for chosen values of: κ_z, r_1, ω against time, t . The plot has been arranged to illustrate the effect of varying flux on incubation time.

Using the approach outlined in this section it is possible to construct a combined machining and melting theory for erosion. Unfortunately, the most obvious way to develop this theory is through knowledge of erosion rates for varying values of the erosive flux, however, there is very little data of this kind available. Uemois and Kleis (Uemois & Kleis, 1975) have pointed out anomalous erosion behaviour dependent on particle flux (see figure 2.8), however, they appear to report that the maximum rate of erosion occurs at zero flux (or concentration) - this is impossible. There can only be zero rate of erosion at zero flux, however it may be that some of their observations can be explained in terms of the target melting. Tilly (Tilly, 1969) has noted incubation times.

One further topic for discussion which emerges when one considers the flow of heat in an eroded target is the effect of cyclic erosion. Many erosion tests subject the target to cyclic erosion, for example a *whirling-arm* type of erosion test, Goodwin et al. (Goodwin, Sage, & Tilly, 1969) rather than continuous erosion. If the duty-cycle is small, that is the ratio of the eroding time to the cycle period, then the foregoing analysis must be modified, however, it will certainly be non-trivial to relate cyclic-erosion to continuous- erosion type tests. This final aspect may prove to be important

because it is often difficult to relate the erosion results of one group of workers to those of another - the answer to this problem may only be a difference in the type of test which has been used.

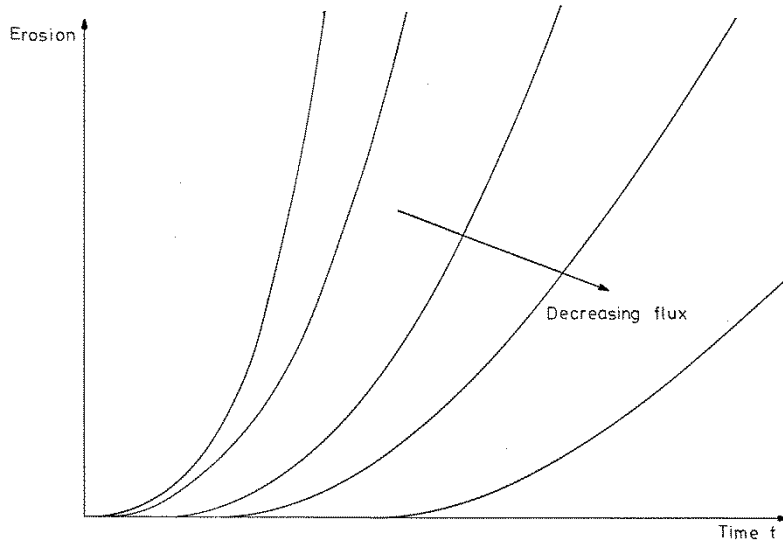


Figure 2.7

Plot of the function below (see equation 2.16) against time, t . The function predicts erosion as a function of time, flux and target mechanical and thermal properties. The curves are families for different fluxes, κ_z . An incubation time before erosion can commence is a result of the melting theory of erosion [$r_0 = r_1 + \omega t$].

$$\exp^{-\kappa_z t} \sum_{r=r_0}^{\infty} (r - r_0) \frac{(\kappa_z t)^r}{r!}$$

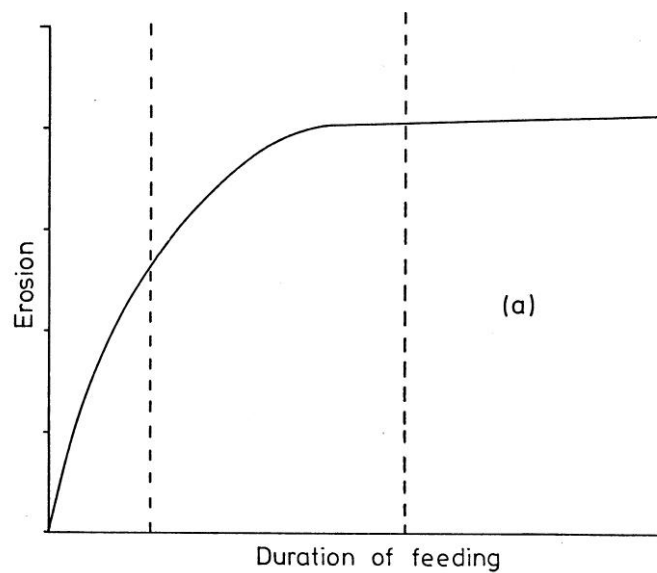


Figure 2.8a

Typical erosion rates versus particle concentration and duration of feeding (Uemois & Kleis, 1975); erosion rate versus duration of feeding.

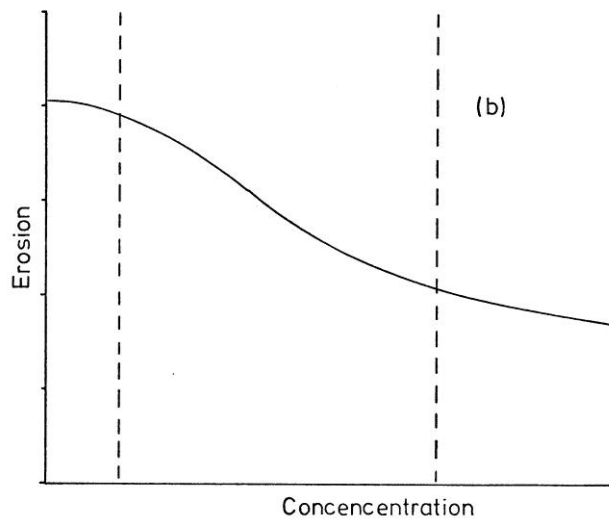


Figure 2.8b

Typical erosion rates versus particle concentration and duration of feeding (Uemois & Kleis, 1975); erosion rate versus particle concentration.

2.5 Forces Experienced by a Sphere during Impact

When a hard sphere strikes a ductile surface it produces a crater, the shape of this crater can be deduced largely if one considers the form of its orthogonal sections. An obvious set of Cartesian coordinates suggests itself: the z-axis placed perpendicular to the target surface, the x-y plane lying on the un-deformed target surface, and the y-axis aligned perpendicular to the velocity vector of the sphere. Sections of the crater in the y-z plane will always be arcs of circles, and it will be assumed that sections in the x-z plane are parabolic. This last assumption may be only approximately correct. However, in the limit of a sufficiently small surrounding region all minima approximate to a parabola, so it is likely to be correct for some values of x - certainly it is as good a starting place as any in modelling the crater shape.

If the deepest point of the crater is a distance d below the un-deformed surface and if the crater dimension measured along the x-axis is $2a_0$, then the two sections will be of the following forms:

$$y^2 = r^2 - (z + d - r)^2$$

Equation 2.25

$$z + d = \frac{dx^2}{a_0^2}$$

Equation 2.26

where r is the diameter of the sphere.

These equations will be used in Chapter 4 to form a function to model the shape of the crater with the intention of calculating the volume of craters by optimising the values of d and a_0 using the method of least squares. The treatment ignores any lips raised above the un-deformed target surface.

Newton's laws relate the acceleration of a particle of mass m to the force \underline{f} which it experiences.

$$m\ddot{\underline{r}} = \underline{f}(t)$$

Equation 2.27

where \underline{r} is the position vector of the particle in the chosen co-ordinate system at a time t and the usual dot convention has been used to indicate differentiation with respect to time. For the case of a sphere impacting a semi-infinite perfectly plastic half-space the resultant force will be zero in the y -direction. Re-writing equation 2.27 in terms of its components yields,

$$m\ddot{x} = f_x(t)$$

$$m\ddot{y} = f_y(t)$$

Integrating these equations with respect to time gives the following:

$$m\dot{x} = \int_0^t f_x(\xi)d\xi$$

$$m\dot{z} = \int_0^t f_z(\xi)d\xi$$

Equations 2.28

If $\underline{f}(t)$ is unknown then there exists no solution to the problem. If, however, the trajectory of the centre of the sphere is known, say $z = g(x)$ for $0 \leq t \leq T$ (where T is the duration of contact of the target and sphere), then

$$\dot{z} = \dot{x} \frac{dg}{dx} \Big|_t$$

It is possible to use this result to equate the integrals in equations 2.28

$$\int_0^t f_z(\xi)d\xi = \frac{dg}{dx} \Big|_t \int_0^t f_x(\xi)d\xi$$

or

$$\int_0^t f_z(\xi)d\xi - \frac{dg}{dx} \Big|_t \int_0^t f_x(\xi)d\xi = 0$$

Equation 2.29

The parabolic x-z section of the crater formed by the sphere describes the trajectory of the last point of the sphere to be in contact with the target (assuming no elastic recovery). The tangent to this curve will be parallel to the velocity vector of the centre of the sphere. Recall equation 2.26

$$z + d = \frac{dx^2}{a_0^2}$$

then

$$\frac{dg}{dx} \Big|_t = \frac{2d}{a_0^2} x(t)$$

Substituting this result in equation 2.29

$$\int_0^t f_z(\xi) d\xi - \frac{2d}{a_0^2} x(t) \int_0^t f_x(\xi) d\xi = 0$$

Equation 2.30

Unfortunately, it is not possible to gain further insight into the problem without some knowledge of either f_z or f_x .

It will be an aim of single particle experiments to examine how reasonable it is to assume parabolic and circular crater sections.

2.6 Erosion at Normal Impingement

The popular theories about the way material is removed from a metal surface are predominantly concerned with cutting mechanisms (Finnie I. , 1958), some authors have suggested fatigue is responsible (Bitter, 1963), (Hutchings I. M., 1979). Finnie's theory has received more attention because of its superior quantitative predictions, however, this theory predicts zero rate of erosion at normal impingement. At the present time all metals and alloys for which erosion data is available have been found to lose mass at the normal impingement angle.

Various authors have tried to reconcile this apparent contradiction between theory and fact by suggesting that the rate of erosion is indeed zero during normal impact, but that either particles fragmenting (Tilly, 1973) or aerodynamic forces (Finnie I. , 1972) help eroding particles strike the target obliquely.

Hutchings et al. (Hutchings, Winter, & Field, 1976) have found that there are small losses of material from targets when single spheres strike them nearly normal. Furthermore, the spheres were sufficiently large and strong to withstand disintegration during the impact and they were unlikely to be deviated by aerodynamic forces.

I will re-examine erosion at normal impingement using large, single spheres as projectiles. In particular I will study the impact event in close detail using a high-speed camera to try to isolate the mechanism of material removal.

2.7 Improving the Erosion Resistance

Metallurgists have put considerable effort into improving the strength, ductility and hardness of metals. The technique of ion-implantation has recently been applied to help improve the general wear resistance of some metal surfaces - this has met with some success (Dearnaley, 1978). The effect which an ion-implanted species has on the erosion resistance of a metallic surface is unknown. Ion-implanting affects the surface layer of the material to a depth of only about 200 μm . It seems unlikely that this technique can make any significant change in the erosion characteristics of materials which are bombarded by particles greater than 200 μm in size. It would be interesting to look at the effects of this treatment on metal surfaces subsequently eroded by small particles (less than 200 μm).

2.8 Apparatus

I have examined erosion by studying the impact of single particles on metallic surfaces. Chapter three describes the apparatus I used to perform the experiments described in this work. Chapter eight describes a design for a multiple particle erosion rig which will be capable of continuously eroding a target surface under precisely controlled conditions. Chapter four describes the techniques used to quantify the results of experiments.

Chapter 3 Single Particle Erosion Rig

3.1 Design Specification

An experimental study of any physical phenomenon must have at its disposal a source of data of sufficient accuracy with which to test a hypothesis connected with that phenomenon. In the case of the phenomenon of erosion by single, solid particles it was considered desirable to be able to alter the following set of variables during experiments.

- Projectile: A solid particle with maximum size not greater than 1 cm and hardness greater than that of the target specimen.
- Velocity: Variable within the range 20 ms^{-1} to 500 ms^{-1} .
- Specimen: A rigidly mounted solid with at least one flat face, the surface to be impacted.
- Temperature: The specimen temperature should be variable within the range 80 K to 1400 K but constant over the impact surface.
- Environment: The gaseous environment of the specimen should neither influence the mechanical process involved in the erosion of the specimen surface nor should it introduce a mass change of the specimen commensurate with any mass change brought about by the erosion.
- Impingement angle: The angle subtended by the projectile velocity vector and the specimen surface should be variable between 0° and 80° .

Previous workers (Barkalow & Pettit, 1979) have failed to put restrictions on some of these variables, in particular specimen environment, or have elected to study instead the more applied problem of simultaneous erosion and corrosion of metal surfaces. Some investigators have included other variables in the study of erosion, for example: state of surface stress of the material (Finnie I. , 1972), albeit at the exclusion of other, perhaps, more dominant factors such as temperature.

The list given above formed a rigid specification for the experiments I intended to perform.

Hutchings and Winter (Hutchings & Winter, 1975) describe the design and operation of a simple laboratory gas gun. This design was adopted for the acceleration of projectiles in the experiments described here. In order to satisfy the remaining details of the specification, a sturdy specimen chamber was constructed of stainless steel into which the gas gun could be fired. In addition, the chamber could be evacuated by a rotary vacuum pump to a pressure of 10^{-3} Torr or purged with an inert gas, to prevent oxidation or nitridation of the specimen surface that might occur in air at elevated temperatures (see figure 3.1).

The remainder of this chapter is devoted to the discussion of various aspects of the design, construction and testing of the single particle impingement apparatus.

3.2 Gas gun

Newton's laws tell us how to calculate the acceleration of a body of a given inertial mass, m , under the action of a set of forces. In a smooth bore gas gun, the projectile, mounted onto a cylindrical polyethylene sabot vehicle inside a steel tube, is accelerated down the tube by a gas pressure differential, P , acting across the sabot length. This is the basic operation of any smooth-bore gun.

A complete theoretical treatment of the operation of such a gun has yet to be proposed. Perfect (Perfect, 1966) has developed a theory based on the adiabatic expansion of the propellant gas from a driving reservoir into the acceleration tube. Seigel (Seigel, 1965) proposes a theory which takes into account the finite amplitude pressure waves propagating within the gas during the firing period. Both approaches indicate that the projectile muzzle velocity should depend upon the ratio of P/m , the ratio of the initial reservoir pressure to the mass of the projectile and sabot, as would be expected from a more straightforward constant pressure consideration of Newton's laws. Hutchings (Hutchings I. M., PhD Thesis, 1974) has tested the veracity of Seigel's theory and concludes that the discrepancies which arise can be attributed mainly to turbulence in the propellant gas flowing from the reservoir into the acceleration tube. In all cases, Seigel's theory predicts a useful upper limit to the projectile velocity which is never more than 12% in error for nitrogen gas and 6% for helium gas.

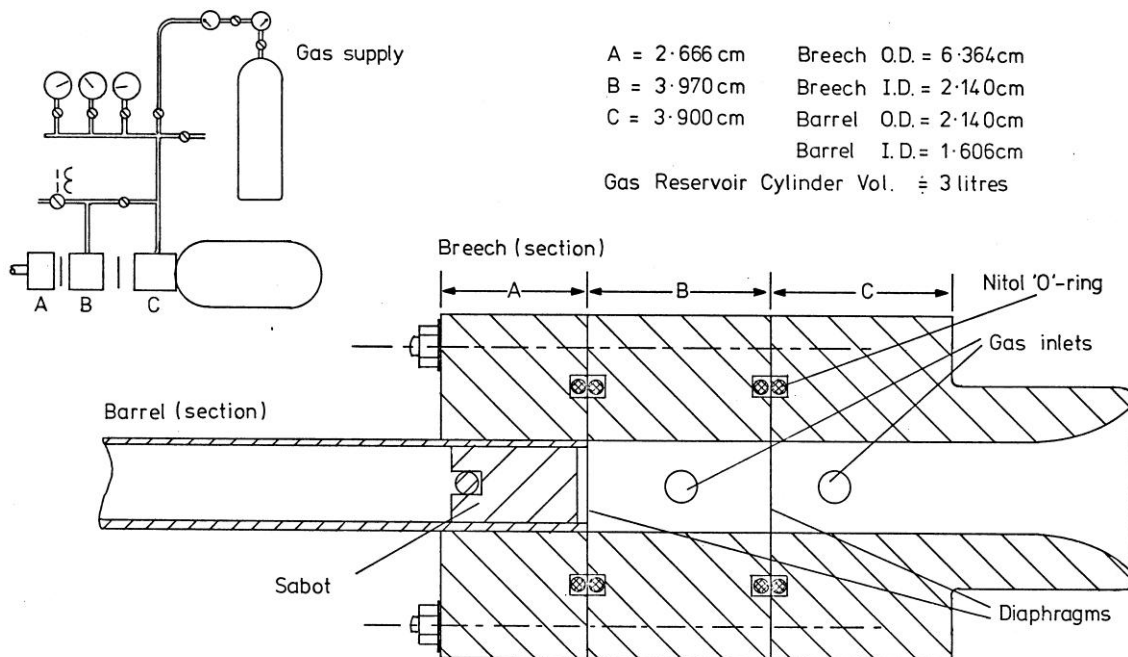


Figure 3.1

Schematic diagram showing the arrangement of the gas gun and specimen chamber.

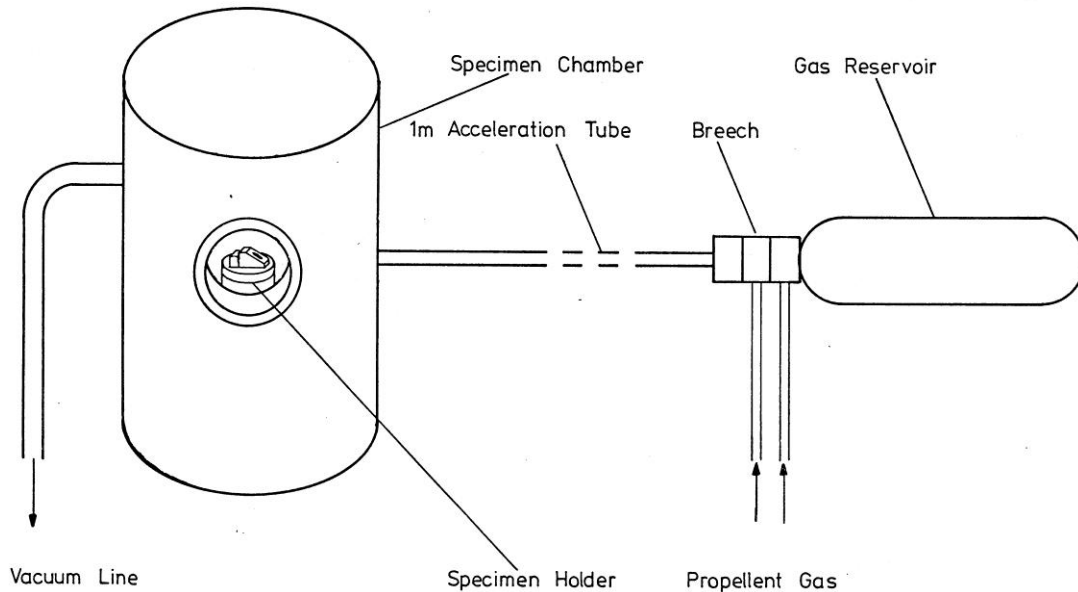


Figure 3.2

Sketch of the breech mechanism of the gas gun showing the sabot and projectile in a position prior to acceleration. The inset diagram, top left, shows the valving, metering and piping which supplies the gas to the gun.

The projectile and sabot must be loaded into the gun barrel at the end nearest the gas reservoir through a breech mechanism(see figure 3.2). The breech mechanism splits into three sections : the barrel end ,the reservoir end, and a middle section for loading the projectile mounted onto the sabot. All three sections are coaxial brass cylinders with Nitol O-ring gas seals sliding on six long screws. The split breech arrangement allows for two foils or diaphragms, usually of metal, to be inserted into each gap of the breech and to be sealed and gripped by the O-rings under compression from the six screws. The gun is now primed ready for firing by pressurising the reservoir with a charge of inert gas, either argon or helium, and applying this charge “quickly” to the rear end of the sabot. The charge is applied by bursting the two foils in sequence, the foil nearer the reservoir being burst first.

Table 3.1 lists typical foil materials and thicknesses used in experiments along with their characteristic bursting pressures. The mechanism of foil bursting is not well understood yet - there are wide variations in characteristic bursting pressures of various foils, for example $\pm 15\%$ between foils from the same production batch and up to $\pm 50\%$ variation between batches. This variation could make for uncertain muzzle velocities if it were not for the use of two foils acting in cascade, the so-called *double diaphragm breech* arrangement. The small inter-diaphragm space within the breech is pressurised to a value less than its characteristic bursting pressure then, assuming both diaphragms are the same type of foil, the reservoir may be pressurised to a value in excess of its normal characteristic bursting pressure without bursting. If the inter-diaphragm space is now vented to atmospheric pressure both diaphragms will burst in cascade. The breech mechanism now acts as a valve to control the application of the reservoir gas to the rear of the sabot.

The efficacy of the gas gun will be impaired if the valve action is *slow*, especially when trying to attain high projectile velocities ($\sim 500 \text{ ms}^{-1}$). In this context *slow* should be interpreted as meaning an opening time commensurate with or greater than the time taken for the sabot to reach the muzzle end of the gun barrel, a time usually of the order of $10 \times 10^{-3} \text{ s}$ and never less than $4 \times 10^{-3} \text{ s}$.

I have measured the bursting time of a single 0.025 mm thick copper foil by using a light source located inside the gas reservoir and a photo-diode placed at the muzzle end of the barrel, coaxial with the barrel (see figure 3.3). With the foil intact no light falls upon the photo-diode, but when the foil ruptures the light passes unimpeded down the barrel illuminating the photo-diode. A single-sweep storage oscilloscope displays the current in the photo-diode which increases with increasing illumination as a function of increasing time. Figure 3.4 is a sketch of the form of the oscilloscope display at the time of bursting, from which it can be seen that it takes approximately $250 \mu\text{s} \pm 50 \mu\text{s}$ for the light incident upon the photo-diode to reach a maximum. Since the turn-on time of the photo-diode is less than 10^{-3} s it is safe to conclude that the characteristic bursting time of this foil is about $250 \mu\text{s}$ at an excess pressure of 3.4 bars.

The breech mechanism uses two diaphragms. Although the opening time of both foils acting together is probably in excess of $500 \mu\text{s}$, the effective opening time of both foils is still only $250 \mu\text{s}$. This is because the time taken by the second foil to burst is the time it takes to develop the full pressure behind the sabot, which is of primary importance in determining the subsequent acceleration of the sabot. The bursting time of the first diaphragm acts merely as a delay in initiating the firing event. This value for the opening time confirms the excellence of the double (and single) diaphragm technique as a fast acting pneumatic valve.

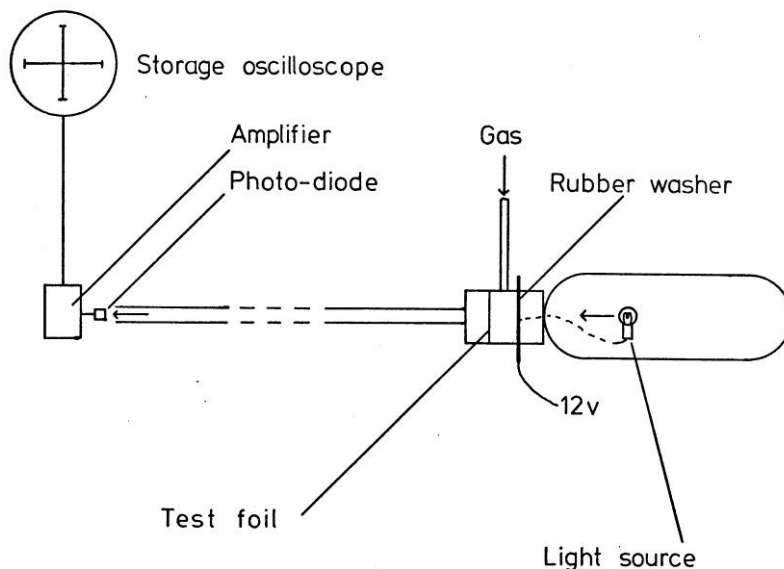


Figure 3.3

Optical arrangement inside the gun used to determine the opening time of the test foil diaphragm.

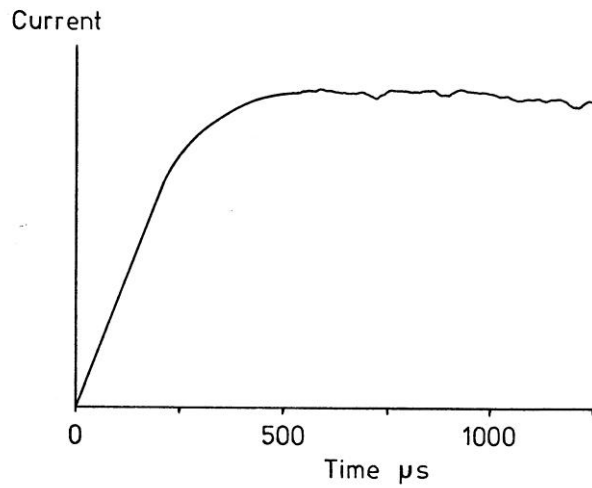


Figure 3.4

Sketch of the oscilloscope trace resulting from the test foil bursting at a pressure of 3.4 bar. Opening time $\sim 200 \mu\text{s}$.

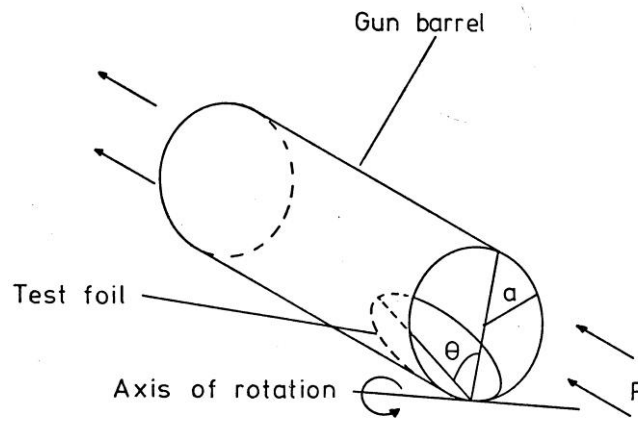


Figure 3.5a

Sketch showing the proposed mechanism of the bursting of the test foil.

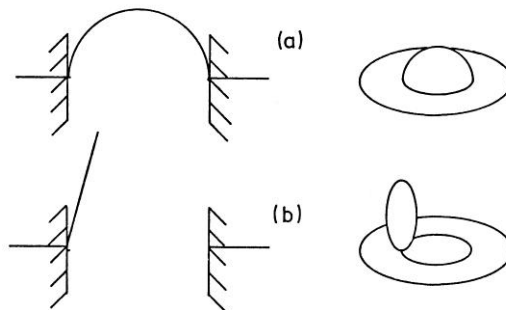


Figure 3.5b

Foil shape is shown for: (a) pressure just less than bursting pressure, (b) after bursting.

Prior to rupture the diaphragm will have deformed into the shape of a dome (see figure 3.5a). Along the circumference of the base of the dome there exist large shear stresses because of the discontinuity of slope measured along a radius; this circle will be most liable to failure. At the onset of rupture, tears or cracks will be initiated at points of microscopic weakness which will run around the base of the dome. The gas pressure can now act on the central section of the foil and start to open it like a door, hinging about any un-torn thread of foil. As the foil *door* rotates about this axis it will experience a decreasing force until it has opened fully when it will experience zero force.

If the foil is of thickness L , density ρ , and the gun barrel diameter is $2a$, then the moment of inertia, I , of the disc of foil sealing the barrel, about an axis perpendicular to the barrel axis through a point on the circumference, will be

$$I = \frac{\pi}{4} a^2 L \rho \left\{ \frac{L^2}{3} + 5a^2 \right\}$$

The parallel axes theorem has been used.

The couple, G , that the disc experiences after it has rotated through an angle of θ radians about the same axis under a constant pressure, P , is given by,

$$G = \pi a^3 P \cos \theta$$

The equation of rotation of the disc is now,

$$I \ddot{\theta} = \pi a^3 P \cos \theta$$

In which the usual dot notation has been adopted to represent differentiation with respect to time.

This non-linear second-order differential equation can be solved by multiplying by the first derivative with respect to time of θ and integrating directly. The constant of integration disappears when boundary conditions are applied:

$$\dot{\theta} = 0|_{t=0}$$

One further integration over the interval $[0, T]$, where T is the time taken by the disc to rotate from $\theta = 0$ to $\theta = \pi/2$ yields the result:

$$\int_0^{\pi/2} \frac{d\theta}{\sqrt{\sin \theta}} = \sqrt{\frac{2\pi P a^3}{I}} \int_0^T dt$$

Thus, the opening time is:

$$T = \sqrt{\frac{I}{2\pi P a^3}} \int_0^{\pi/2} \frac{d\theta}{\sqrt{\sin \theta}}$$

The remaining integral is of the general form of an elliptic integral, however, with the present limits it is a Beta function, $B(0.25,0.50)$, which can be written in terms of the Gamma function, $\Gamma(m)$. Finally, substituting for I we obtain the compact form:

$$T = \sqrt{\frac{5La\rho}{8P} \frac{\Gamma(0.25)\Gamma(0.5)}{\Gamma(0.75)}}$$

Or

$$T = 4.12 \sqrt{\frac{La\rho}{P}}$$

For the case of the gas gun described here the following value applies: $a = 0.8$ cm. For a copper foil of thickness, $L = 0.025$ mm, and density, $\rho = 8 \times 10^3$ kg m⁻³, bursting at a pressure of approximately 4 bars, the predicted opening time, T , is

$$T = 275 \mu\text{s}.$$

This value is in good agreement with the observed value of $250 \mu\text{s} \pm 50 \mu\text{s}$. This value also indicates that the mechanics of the tearing process of the foil is not an important factor in governing the opening time of the valve but that the inertia of the foil alone is important.

I have tried using a single diaphragm as a valve that was ruptured externally by a spring driven needle. This method has a certain attractiveness from the point of view of ease of use and high pressure bursting it proved to be erratic and unreliable compared to the double diaphragm method. After a series of initial tests this method was not pursued further.

Material	Thickness (mm)	Bursting Pressure (Bar)
Polyethylene	0.025	1.0
Polyethylene	2 x 0.025	1.7
Aluminium	0.025	2.5
Copper	0.025	3.2
Aluminium	2 x 0.025	5.2
Copper	2 x 0.025	6.0
Aluminium	3 x 0.025	7.0
Copper	0.05	10.0
Copper	0.075	15.5
Stainless steel	0.025	17.0
Copper	0.1	22.0
Mylar	0.1	24.0

Table 3.1

Characteristic bursting pressures of various diaphragms

Projectiles that can be delivered by the gun may vary in size up to 1 cm. They may be attached to the sabot either by gluing with *Durofix* glue, which breaks easily when the sabot is arrested, or by inserting the projectile into a machined hole in the front end of the sabot.

Polyethylene was favoured as a sabot material because of the low sliding friction between steel and polyethylene. High density polyethylene is preferred to the low density variety because it extrudes less when it is arrested at the muzzle of the gun, an important consideration when removing the sabot after it has been used.

3.3 Projectile Velocity Measurement

The projectile and sabot accelerate to the end of the one metre long barrel until a constricted orifice abruptly arrests the sabot, while the projectile detaches and travels on at constant velocity until it strikes the target specimen surface. During the period of free flight the projectile velocity is determined by measuring its time of flight across a set distance: 40 mm in this case. An electronic timer measured this time of flight (see figures 3.6 and 3.7).

A 10 MHz quartz controlled oscillator was started and stopped by the passage of the projectile across two focused light beams. The light sources used were light emitting diodes (LEDs), Fairchild type FLV104, which were positioned perpendicular to and shining across the projected axis of the barrel (see figure 3.6). Two photo-transistors, BPX25, similarly positioned to the LEDs, receive the un-deflected light from the LEDs.

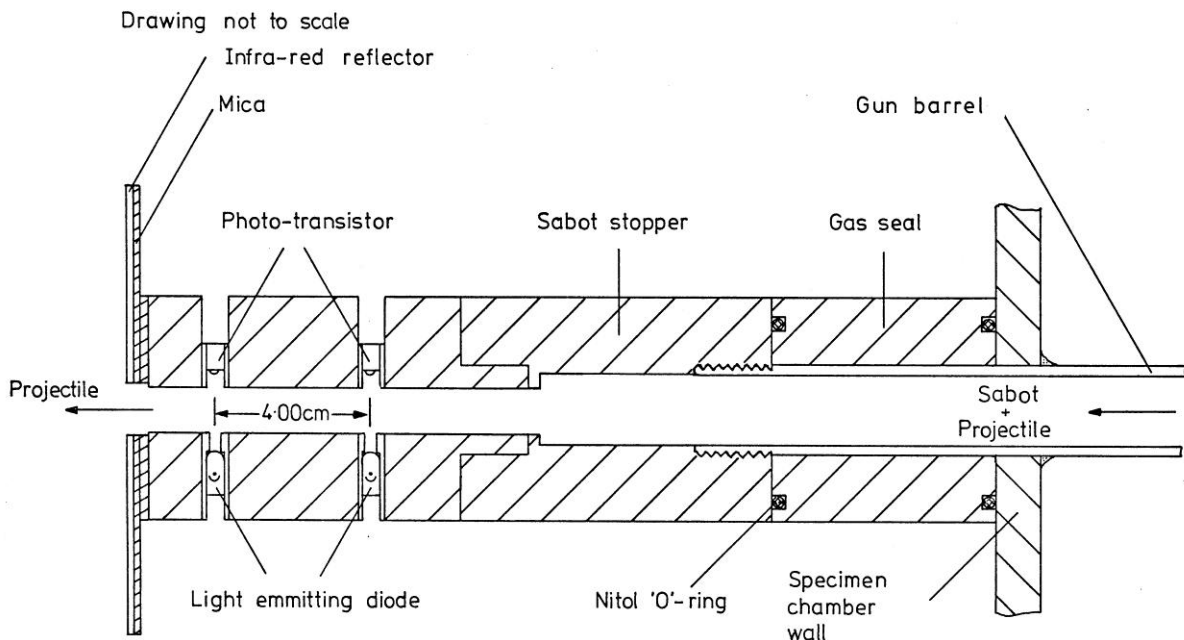


Figure 3.6

Sketch of the muzzle of the gun showing: the velocity measuring section (the head amplifier has been removed for clarity); the sabot stopper; and a block to act as a seal against propellant gas escaping behind the arrested sabot.

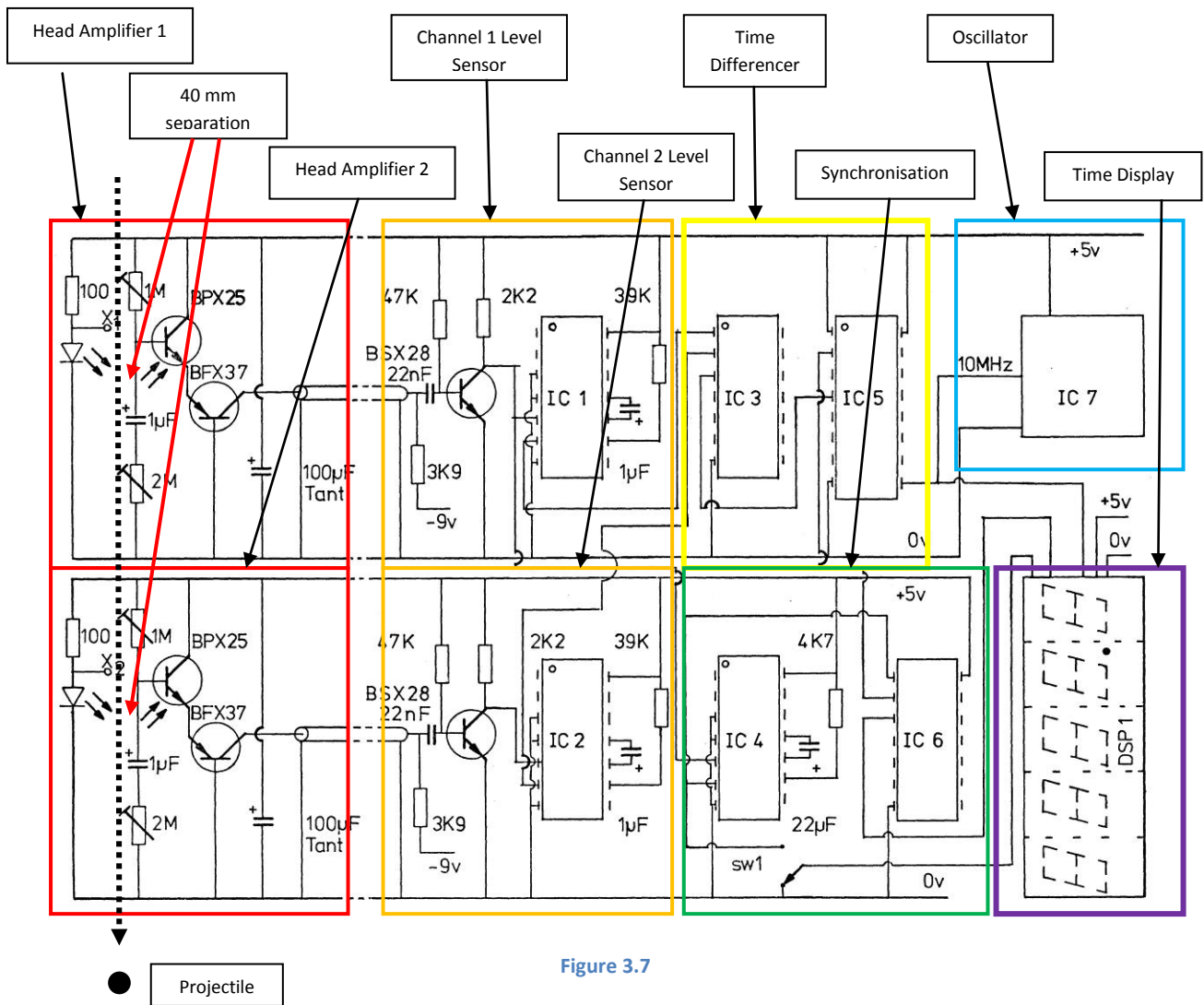


Figure 3.7

Circuit diagram of the velocity measuring timer.

Unlisted components:

- IC1, IC2, IC4 - 74121 monostables.
- IC3 - 7486.
- IC5 - 74175.
- IC6 - 7400.
- IC7 - 10 MHz quartz clock oscillator with TTL output.
- DSPI - 5 off TIL307.

The shadow cast on the photo-transistors by the projectile produces minute current changes ($\sim 10^{-6}$ A) in the base-emitter junction of the photo-transistors; these currents are amplified and processed to control the timer. The timer and photo-transistors' head amplifier were connected electrically by three, four-metre long cables. Mechanically, the velocity sensor section consisted of a mild steel block mounted onto the exit end of the gun barrel muzzle.

The unaided photo-transistors would find it an impossible task to drive an electric current down such long cables. In addition, photo-transistors are inherently slower than is actually sufficient to give the

timing accuracy wanted in the experiments; photo-transistors turn-off, delay and switch-on in about 8 μs (propagation time) which could represent $\pm 8\%$ uncertainty in timing. This reasoning is unduly pessimistic of course because both photo-transistors will experience roughly the same delay tending to cancel-out most of the possible error, however, variations between the characteristics of the photo-transistors will introduce errors, the magnitude of which is likely to be dependent upon the magnitude of the propagation delay time. Fortunately the head amplifier serves a dual purpose; firstly, of speeding-up the photo-transistors to propagation times less than 1 μs , thereby reducing the uncertainty to less than $\pm 1\%$ for a projectile velocity of 200 m s^{-1} and secondly, of being capable of driving long cables. The head amplifier circuit has one more useful feature: it can be adjusted in sensitivity to give good discrimination against smaller sized particles in free-flight with the projectile - Appendix A lists the procedure for optimising this circuit with the aid of a novel testing circuit.

Timer Circuit Operation

When the projectile in turn eclipses the two LEDs the currents in the base-emitter junctions of the photo-transistors (BPX25) are reduced in magnitude. This change of current turns off the BFX37 transistor which acts to speed-up the photo-transistor by its common-base amplifying action; both transistors are directly coupled. The 1 μF capacitor and 2 $\text{M}\Omega$ variable resistor de-couple the base circuit of the photo-transistor; zero resistance and hence maximum de-coupling would make the base voltage almost immune to any light level changes except very large, slow changes. It is this mechanism which allows for a variable degree of discrimination against particles smaller than the projectile from triggering the action of the photo-transistor and hence the velocity measurement. The 1 $\text{M}\Omega$ variable resistor in the same circuit sets the correct DC level of both the BPX25 and BFX37.

The BFX37 transistors drive their 3.9 $\text{k}\Omega$ output resistors through the long cables into a nine volt negative bias provided by a small battery. The circuit action forces up the collector of the BSX28 transistor to nearly five volts positive, a condition which is sensed in each channel by the Schmitt trigger inputs of the monostables IC1 and IC2. The Schmitt action gives a high degree of discrimination against noise. Once triggered, the monostables time their one-shots, a period of not less than 30 ms each, in which they are immune to further input transitions.

The voltage input to IC1 also triggers the monostable IC4 which has a period of about 20 ms , which is a period less than the period of IC1.

IC3 is an exclusive-OR gate; it generates pulses of lengths equal to the difference in periods of IC1 and IC2, therefore, it will always generate two such pulses. The first pulse is of a duration equal to the time of flight of the projectile, this is the pulse required to be measured, the second pulse is unwanted, generated at the end of the timed periods of IC1 and IC2. This second pulse cannot begin earlier than 30 ms after the start of the first pulse, and it is inhibited from reaching the counter section of the timer by IC4 which only allows pulses to pass within the 20 ms period of IC4 (see Figure 3.8).

IC7 is the master clock oscillator of 10 MHz frequency. The pulses from IC7 are counted by the decade counters in DSP 1 for the period of projectile flight. Five cascaded decades are employed in

the counter circuit and each decade is displayed making a timer showing a maximum counting period of 9999.9 μs .

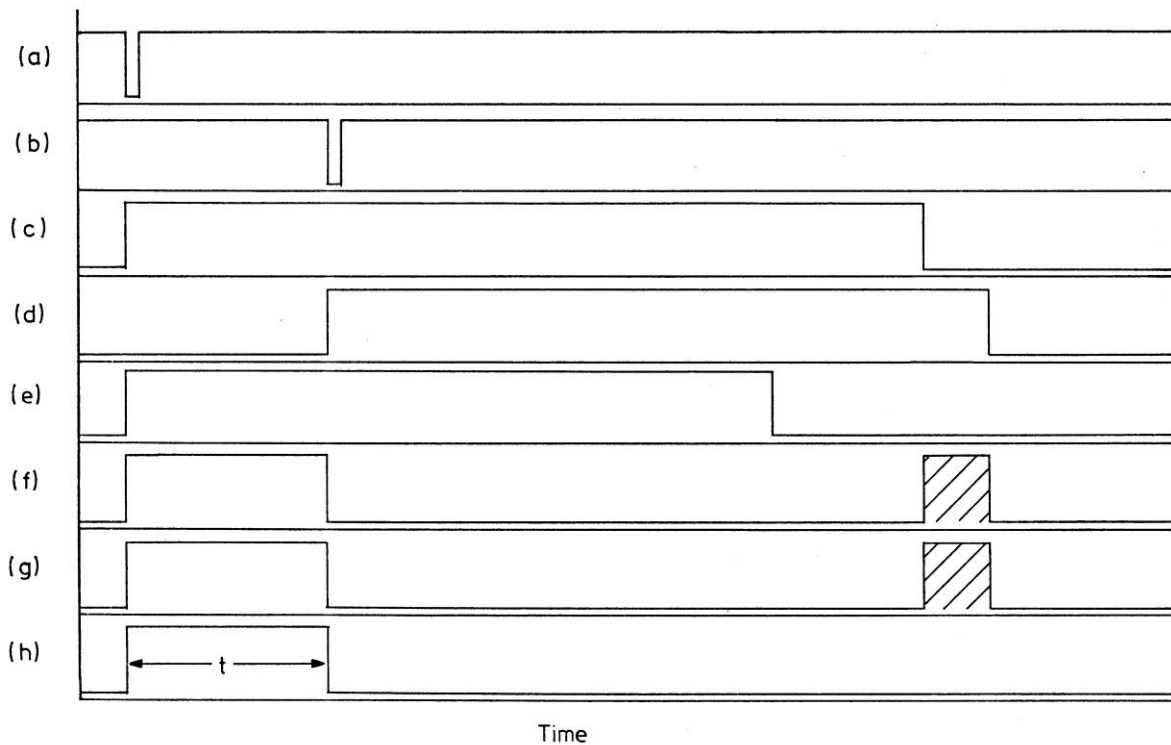


Figure 3.8

Pulses within the timer circuit (not to time scale).

Explanation of pulses shown in figure 3.8:

- (a) Projectile arrives at first photo-transistor (voltage on first BSX28 base).
- (b) Projectile arrives at second photo-transistor (voltage on second BSX28 base).
- (c) IC1 monostable output.
- (d) IC2 monostable output.
- (e) IC4 monostable output.
- (f) Output of differencer 1C3. Difference of pulses of IC1 and 1C2. (Hatched pulse is unwanted.)
- (g) Pulse after synchronization with 10 MHz oscillator. (Course scale of diagram does not show changes.)
- (h) Output to enable counter/timer. Period t is the time of flight of the projectile across 40 mm measuring distance.

IC5 is included for the purpose of synchronising the timed pulse to the start of one of the master oscillator pulses - this avoids spurious counting in the timer. Figure 3.8 shows the chronological sequence of the pulses within the circuit (not to time scale).

It is not possible to attach full significance to the last digit displayed (0.1 μs) for reasons already discussed in this section. It is only included for the purpose of rounding up or down the next digit.

The circuit works well and has been checked, both for operation and timing accuracy, with artificially generated pulses (see Appendix A) against a commercial timer device and a single sweep storage oscilloscope. It showed repeated accuracy in tests of better than $\pm 1 \mu\text{s}$.

This method of measuring velocity requires no calibration or corrections because the projectile is in free-flight. Occasionally errors in timing do occur but this is nearly always due to electrical interference, as the device must operate within an electrically noisy environment.

3.4 Specimen Heating

In an earlier section of this Chapter the specification of the experimental conditions was listed, the temperature range was 80 K to 1400 K. Low temperatures were produced by cooling with liquid nitrogen and the elevated temperatures were produced by heating with radio frequency magnetic induction (RF heating). Although it was anticipated that some ferromagnetic materials would be tested it was required that the apparatus should work equally well with a non-ferromagnetic target specimen. For that reason a nickel alloy (Inconel 601) specimen holder was constructed which, beneficially, also maintained considerable structural stability up to 1400 K.

The choice of R.F. Heating was based on the availability of a suitable generator, in this case a Radyne set with maximum output power of 25 KW.

Figure 3.9 is a sketch of the specimen holder and column. The Inconel 601 specimen holder and top block were located on four, long, Inconel 601 screws - screwing into a mild steel column which was spaced from the top block by a non-magnetic stainless steel cylinder and two thermally-insulating, mica washers. The column is mounted on a movable screw-driven, carriage allowing the target specimen position to be adjusted. The column is split part way down its length, across a diameter, and separated by a rotatable collar which has the effect of altering the apparent length of the column or the position of target specimen. The target specimen can be moved by these two screw adjustments, acting in orthogonal directions, until accurately positioned impacts can be made. It proved possible to position impacts to within 0.5 mm on a target inclined with its surface normal at an angle of 70° to the projectile velocity vector.

The mica washers were included in the column to reduce heat losses from the specimen holder by conduction down the column. At the top of the mild steel section, below the lower mica washer, a copper tube was silver soldered for the purpose of water cooling.

The specimen holder and upper section of the column could be heated to a varying extent by altering the magnetic flux density generated by a coaxial induction solenoid. This coil was also made from copper tube wound into about five turns. Cooling water circulated through this coil fed directly from the RF generator. Care was taken to ensure that the coil never touched the column and that the coil windings would not be struck by the projectile either before it impacted the target or after rebounding. The power entering the heated section of the column could be controlled very precisely because the Radyne set was regulated by a saturable reactor, which was in turn controlled by a small, multi-turn potentiometer connected via a long cable.

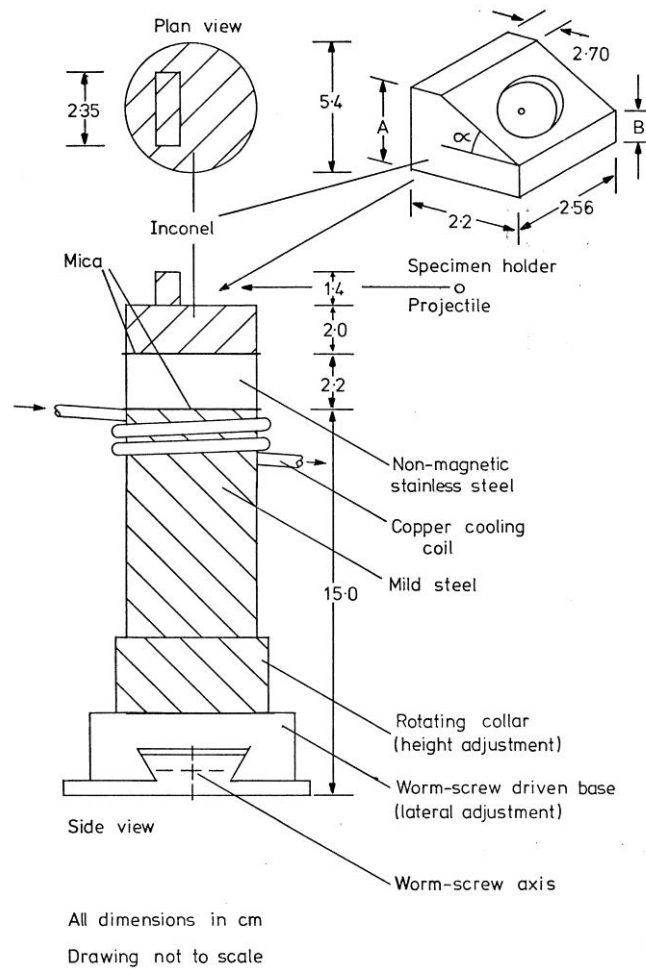


Figure 3.9

Sketch of the specimen column and holder.

Table showing the dimensions of the specimen holder for various angles.

Angle α (degrees)	A (cm)	B (cm)
10	1.514	1.067
15	1.555	1.023
20	1.601	0.916
25	1.697	0.825
30	1.795	0.715
35	2.515	0.610
40	2.047	0.449

Table showing the dimensions of the specimen holder for various angles.

Note that the complementary angles shown in the table above are also available for each block. These were designed to impact the central point of the target even when turned through a right angle.

It proved to be a straightforward operation to remove the R.F. coil and connect instead of it a tight fitting cooling coil around the top of the column, for the circulation of liquid nitrogen and cooling of the target specimen. The liquid nitrogen was pumped around the cooling coil by the pressure generated inside a Dewar flask from heating and boiling small quantities of the liquid. In order to reach the range 130 - 80 K it was found necessary to spray liquid nitrogen onto the specimen surface.

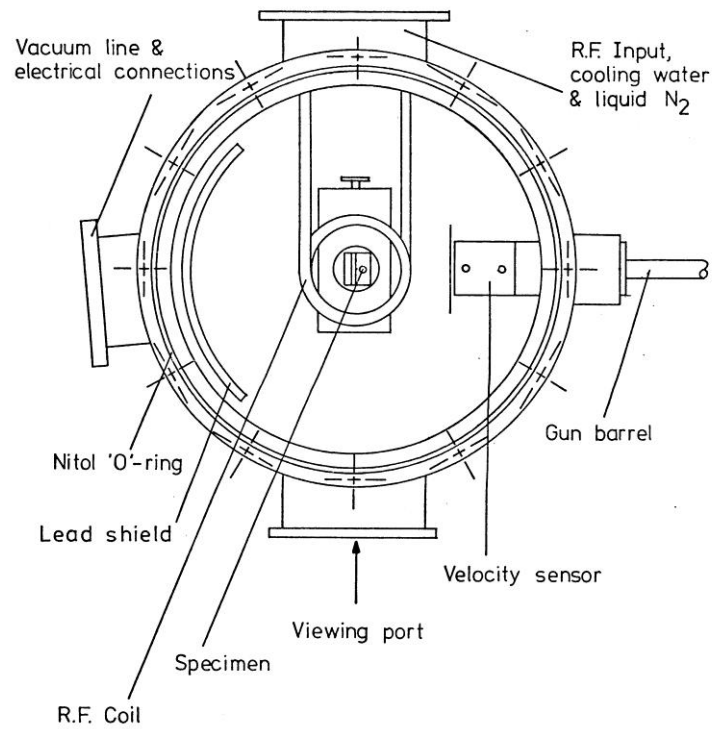
Specimens were discs of diameter 12.8 mm and thickness 3.2 mm.

The velocity measuring block, onto which was mounted a die-cast aluminium box containing the head amplifier, was only three centimetres distant from the target specimen surface and was subject to considerable radiation heating especially at target specimen temperatures in excess of 800 K. In order to help combat this unwanted heating it was thought judicious to fit a polished aluminium reflector backed with a mica strip onto the projectile exit end of the velocity measuring block. A hole was made in the heat shield to allow the free passage of the projectile.

The target specimen surface temperature was measured directly by using a nickel/chromium-nickel/aluminium thermocouple held in place by the resilient force of its bent wires. The thermocouple temperature was displayed in degrees centigrade by a Comark 5001 digital device. No linearising was necessary with this device and quoted accuracy is $\pm 0.5^\circ\text{C}$ over the full range of temperature which covered the range studied in the experiments. One disadvantage with this technique of temperature measurement compared to an optical pyrometer for example was that the RF magnetic field induced currents in the thermocouple wires producing an erratic, erroneous display of temperature. Therefore, accurate measurements of temperature were always made with the RF field switched off.

3.5 Specimen Chamber

In experiments concerning only mechanical erosion, it is important to remove any possible effects due to corrosion. In the set of experiments described in this work it is most undesirable to have corrosion or oxidation accompanying the effects of erosion. The specimen environment best satisfying this requirement is of course a good vacuum, better than 10^{-6} Torr. But it is impossible to accelerate a projectile by pneumatic pressure without some of the propellant gas entering the specimen chamber and degrading the vacuum. In the equipment described here inert propellants were used exclusively: either argon gas or helium gas, and the specimen chamber was purged with the same gas. Only negligible specimen surface discolouration resulted in heating the specimen inside the chamber after it had been thrice evacuated to a pressure of 10^{-2} Torr and purged with the appropriate gas - this was the case for temperatures even in excess of 1200 K. The efficacy of this procedure was verified by periodic control-type experiments performed under identical conditions to standard experiments except that no projectile was mounted onto the sabot. In all cases the change of mass of the specimen was less than 5×10^{-8} Kg for an average specimen mass of 3.5×10^{-3} Kg, which in any case was less than the quoted accuracy of the laboratory balance used to determine the mass changes.



Plan view (Top plate removed)

Chamber O.D. = 36.0 cm
Chamber I.D. = 31.0
Chamber height = 38.0
Viewing port diameter = 10.5
Locating screws (12) diameter = 0.940
Top plate, thickness = 2.00
Base plate, thickness = 3.00

Drawing not to scale

Figure 3.10

Plan view sketch of specimen chamber.

The specimen chamber (see figure 3.10) was of a very sturdy design having a thick, double walled, stainless steel cylinder. The cylinder and top plate were both cooled by water flowing inside the cavity.

The cylinder had five access ports other than the top and bottom plates:

1. One to allow the entry of the gas gun barrel.
2. Another for low current electrical connections (e.g. thermocouple wires, head amplifier cables).
3. A third as an outlet to the vacuum line.
4. The fourth was fitted with a thick Pyrex glass viewing window suitable for external photography.
5. The last port was for inlet and outlet pipes for the cooling water, liquid nitrogen and high-current RF power.

Both the top plate and the bottom plate could be removed, the latter only infrequently as would have required dismantling the entire chamber, but the former was removed frequently for changing specimens and performing minor adjustments and repairs. Both plates were held in place by twelve stainless-steel Allen screws. The ports were all TIG welded and sealed with Nitol O-rings.

The chamber was evacuated using a single action Edwards' rotary pump (high volume pumping rate type).

The chamber and gun were mounted on a 3 m long steel framework (made of Dexion), with the gun sitting directly on a steel I-beam to aid rigidity.

The rotary pump sat upon a low trolley and was cushioned by thick foam to help isolate its vibrations from the rest of the apparatus; in addition a short, flexible rubber hose was included in the vacuum line piping for the same reason. The desire for small vibrations was two-fold: to minimise noise and to reduce the possibility of the RF coil coming into contact with the specimen column.

The source of propellant gas was a high pressure cylinder (170 bar when full). The gas was fed via flexible hoses to pressure gauges mounted on the framework, placed at a convenient level for the operator, and then piped to the breech inlets (see inset diagram in figure 3.2). An electrically actuated solenoid valve was used to vent the inter-diaphragm space in the breech when firing the gun. Since this space was vented to atmospheric pressure it was advantageous to fire the gun into a chamber pressure also of one atmosphere (~ 1 bar). Chamber pressure was measured with two gauges, one for the range 1 to 10^{-3} Torr, a Pirani gauge, and the other covering the range of 1 to 760 torr. The latter gauge was monitored while re-pressurising the chamber.

It became necessary to add a two metre long extension to the frame work to accommodate the multiple particle erosion rig. This is explained in Chapter seven.

3.6 Safety Considerations

Operator safety should always be of paramount importance in the design and operation of any piece of equipment. I view it as a poor reflection on our present-day society and especially on the scientific community in general that the importance of safety is only now being stressed.

Safety features or checks which were implemented are listed below.

1. The gas reservoir for the gun was tested for its susceptibility to fracture by filling it with oil C (not gas) and increasing its pressure to 200 bars. No cracks or oil seepage were visible.
2. A heavy duty earth of copper braid was fitted to the specimen chamber. All electrical mains powered equipment was earthed.
3. A thick PMMA screen was fixed over the glass windows of the pressure gauges of the gun.
4. A sturdy, thick-walled metal construction was employed for the specimen chamber.
5. The viewing port into the specimen chamber was made of 13 mm thick Pyrex glass which was thicker than that recommended to withstand evacuation.

6. Lead shields were placed at suitable positions inside the specimen chamber to absorb the kinetic energy of the rebounding projectile. The rationale behind this feature was not out of consideration for the chamber walls but an attempt to reduce the possible risk of puncturing one of the copper cooling water pipes while the specimen was at high temperature, which otherwise could have lead to the catastrophic vapourizing of the inflowing water.

3.7 Performance

The apparatus meets the specification set out at the start of this Chapter. There is only one part of the specification that has proved difficult to meet, that is attaining very low test temperatures 80 to 130 K. Over the temperature range 1100 to 1400 K the target specimen radiates a considerable amount of energy (upwards of 4KW) which has three detrimental effects:

1. The one metre distant sabot is warmed to such an extent that it starts to soften, this increases the frictional drag on the sabot and results in an erratic final muzzle velocity.
2. Radiation heating starts to melt the insulation of wires and soften any poorly cooled O-ring seals, which requires both careful shielding of the wires with aluminium foil where possible and regular checking of the seals to prevent damage.
3. For reasons already discussed it is necessary to switch-off the magnetic field which heats the specimen before an experiment can be performed. Unfortunately, this results in a specimen cooling rate of more than 1° K per second which increases the error in measuring the temperature in this elevated range.

Chapter 4 Quantitative Observations of Single Impacts

4. 1 Introduction

The development of the cutting theory of erosion has benefited greatly from studies involving the impact of single particles onto ductile surfaces (Hutchings, Winter, & Field, 1976) (Hutchings I. , 1977). The impact of a sphere onto a ductile surface has only been studied theoretically for the case of normal impact (Davies, Proceedings of the Royal Society A (197), 1949); a complete theoretical treatment of oblique impact still remains to be made. However, the experimental study of oblique impact by spheres has obtained rather more attention. These studies have considered the effects of the size and density of the sphere and its velocity and angle of impingement on the subsequent deformation of the target (Hutchings I. M., PhD Thesis, 1974). Shewmon (Shewmon, 1979) has shown that overlapping impacts are an important consideration in erosion.

Some of the quantitative measurements which can be made of single impacts are the following: mass loss, the volume of the crater formed, and the change of kinetic energy of the ball resulting from impact. Mass loss can be determined by weighing the target specimen before and after impact. The accuracy of this measurement is limited by the mass changes which can be detected and the best accuracy is reached when target specimen masses are of the same order of magnitude as the mass of the impacting projectile. This condition cannot be implemented in experiments but it is possible to arrange that the target mass is only an order of magnitude, or so, greater than that of the projectile.

In the experiments described in this chapter, 5 mm diameter hardened steel spheres were fired at target discs which were 12.7 mm in diameter and 3.5 mm thick. The mass of each sphere was 0.50972 ± 0.00002 gm whilst the mass of each target sample was in the range 1.7 to 3.5 gm. The spheres were fired at the target samples at a constant angle of impingement, $20.0^\circ \pm 0.5^\circ$, and at a constant velocity 130 ± 20 ms⁻¹. Experiments were performed on a variety of metals and alloys over a range of temperatures 120 K to 1350 K. At elevated target temperatures it proved to be difficult to accelerate the projectile to the same velocity for every test (hence velocity range ± 20 ms⁻¹, the reason for this is obscure but it may be due to thermal radiation softening the sabot plastic thereby increasing the friction between the sabot and the acceleration tube.

I have not performed any experiments to measure the kinetic energy change of projectiles resulting from impact. These experiments would be interesting because, from them and knowledge of the crater volume, it would be possible to calculate the dynamic hardness of the metal as a function of temperature. This is an important parameter in simple theories of erosion, for example, equation 1.2. Experiments of this type will be performed at a later stage.

The volume of the crater produced by the impact can be measured by two methods. Firstly, by machining away the material pushed-up around the crater to the level of the un-deformed surface, filling the remaining depression with Plasticene, and weighing the Plasticene when it has been picked out. This method works well when the crater is more than a few cubic millimetres in volume

but becomes very inaccurate for the volumes produced in these experiments ($0.1 \times 10^{-9} \text{ m}^3$ to $2.0 \times 10^{-9} \text{ m}^3$). The volume of a crater produced on the surface of a mild steel target at a test temperature of 983 K was measured ten times by this method resulting in an average value of $1.4 \times 10^{-9} \text{ m}^3$, the standard deviation of this figure was $0.2 \times 10^{-9} \text{ m}^3$, which represents a measurement accuracy of $\pm 15\%$. It proved to be impossible to measure the volume of a smaller crater ($0.2 \times 10^{-9} \text{ m}^3$) by this method to within a set of values ranging over less than $\pm 50\%$.

4.2 Moiré Topography

The second method to be described here, and the one which was used in experiments, is based upon the technique of moiré contour topography (see figure 4. 1). White light from a point source illuminates the crater and un-deformed surface of the target through a coarse-ruled grating (19.67 lines per mm). The grating was positioned so that it was parallel to and nearly touching the target surface. The target surface and crater had been coated previously with a thin layer of nickel (thickness less than 1000 \AA), which was applied uniformly by evaporation. The surface finish was similar to white silk and was produced by evaporating under poor vacuum conditions (10^{-2} Torr instead of the customary 10^{-6} Torr) - this produces a surface with good light scattering properties. The shadow of the grating cast on the target surface forms a moiré interference pattern when it is viewed through the same grating and gives rise to contrast fringes corresponding to contours on the surface (Theocaris, 1969). The image of the fringes must be observed with a long focal length lens (80 mm) set with a small aperture ($f/16$) so that the depth of focus is greater than the distance from the grating to the deepest point of the crater.

The clarity of the moiré pattern is undiminished by moving the grating whilst observing, provided it is only moved in its plane, indeed Takasaki (Takasaki, 1970) advocates this movement for photographic observation because it removes unwanted high-frequency (aliasing) components of the interference pattern. This was adopted as standard in these experiments. Figure 4.2 shows an impact crater photographed under moiré topography conditions, the contour fringes are clearly visible and show considerable detail about the surface. The contours are all closed although the contours are so closely concentrated around the edge of the lip that they appear to be discontinuous. The highest complete contour in the crater, which is the same shade as the un-deformed surface, marks the boundary of the region which will be modelled in the following analysis.

The crater contours are elliptical to a good approximation and it is possible to construct a function which can represent the crater shape below the un-deformed surface. For a contour at a given depth below the target surface

$$\frac{x^2}{a^2} + \frac{y^2}{b^2} = 1$$

Equation 4.1

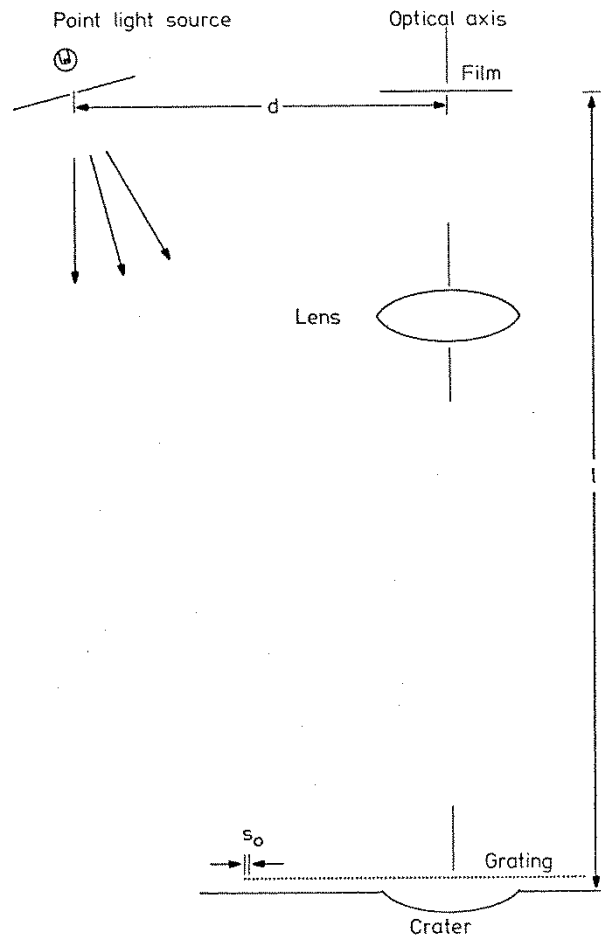


Figure 4.1

The geometry of the moiré topography method. Fringes are observed in the crater with spacing, Δh , given by $\Delta h = s_o l/d$.

In Chapter 2 the form of orthogonal crater sections was discussed - recall equations 2.25 and 2.26:

$$y^2 = r^2 - (z + d - r)^2$$

Equation 2.25

$$z + d = \frac{d}{a_o^2} x^2$$

Equation 2.26

where r is the diameter of the impacting sphere. The lengths of the major and minor axes of equation 4.1 are points on these two sections and so it is possible to replace a and b by

$$a^2 = \frac{a_o^2}{d} (z + d)$$

$$b^2 = r^2 - (z + d - r)^2$$

Equation 4.1 now becomes

$$\frac{d}{a_o^2(z+d)}x^2 + \frac{1}{r^2 - (z+d-r)^2}y^2 = 1$$

Equation 4.2

This equation is remarkably compact, it has only two independent parameters, a_o and d , which correspond to half the crater length and the crater depth, respectively. The area of an ellipse is πab , therefore the volume of the crater is given by

$$Crater\ volume = \pi \int_0^{-d} a_o \sqrt{\frac{z+d}{d}} \sqrt{r^2 - (z+d-r)^2} dz$$

Equation 4.3

This integral is most easily evaluated numerically using (say) Simpson's rule. The value of the parameters, a_o and d , can be measured directly from a moiré topograph of a crater or, alternatively, they can be optimised using the method of least squares so that the function in equation 4.2 best represents the observed contour pattern. It is possible to estimate the depth of a crater to a quarter of a fringe which, under certain circumstances, may represent an accuracy of only $\pm 12\%$ in this measurement. Although this is still a basis for a more accurate estimate of volume than by the Plasticene method, it is possible to estimate the volume by optimising the parameters resulting in a range of values inside $\pm 2.5\%$ (standard deviation) of the average. For example, a mild steel specimen impacted at 983 K had a crater volume measured by fitting parameters of $1.43 \times 10^{-9} \text{ m}^3 \pm 0.01 \times 10^{-9} \text{ m}^3$ averaged over four measurements (compare with the value obtained by the Plasticene method already described). For smaller crater sizes the measurement becomes less accurate, for example, a mild steel specimen impacted at 300 K had a crater volume of $0.128 \times 10^{-9} \text{ m}^3 \pm 0.003 \times 10^{-9} \text{ m}^3$. However, inaccuracy arises in measuring the depth and an accuracy of only $+5\%$ in measuring the volume is to be expected.

The method of optimising parameters achieves a smaller spread of values of volume (and presumably increased accuracy) at the expense of increased complexity when compared to direct measurement of parameters. In this case the moiré topographs were digitised along contours and the function in equation 4.2 fitted to the digitised points. The procedure is an elaborate one and can only be performed by computer program which is listed and described in Appendix B. Figure 4.3 shows the digitised points (crosses) of the contours of a crater whilst the family of concentric ellipses are contours fitted to these points by the method of optimising the parameters. Once the parameters have been calculated it is possible to draw the crater in perspective using another computer program (3-dimensional hidden line plot). Figure 4.4 is a computer re-construction of the same crater drawn by the hidden line plot. The function does not model the shape of the crater lip.

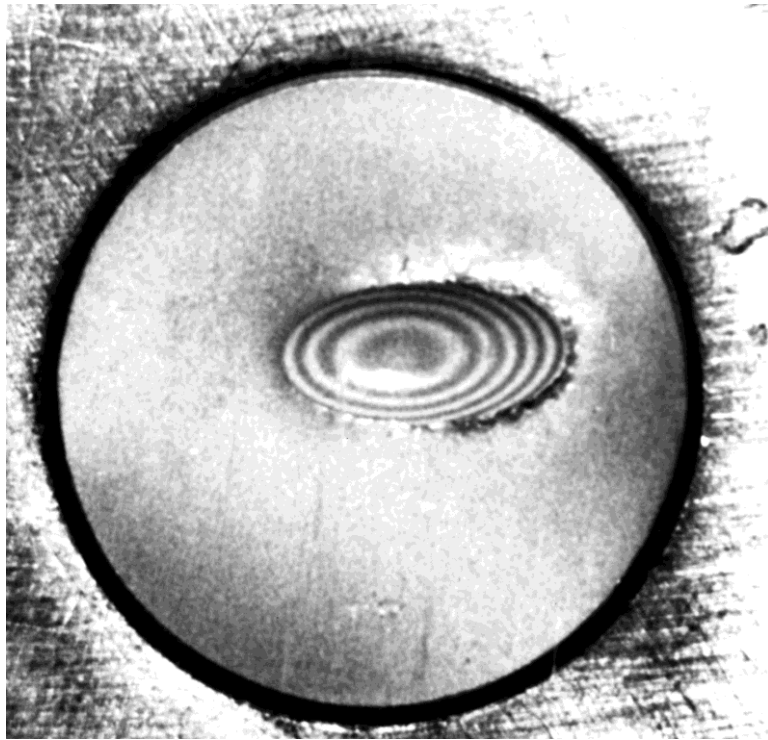


Figure 4.2

A typical moiré topograph of a crater in a copper target. The fringe spacing is $103 \mu\text{m} \pm 1 \mu\text{m}$.

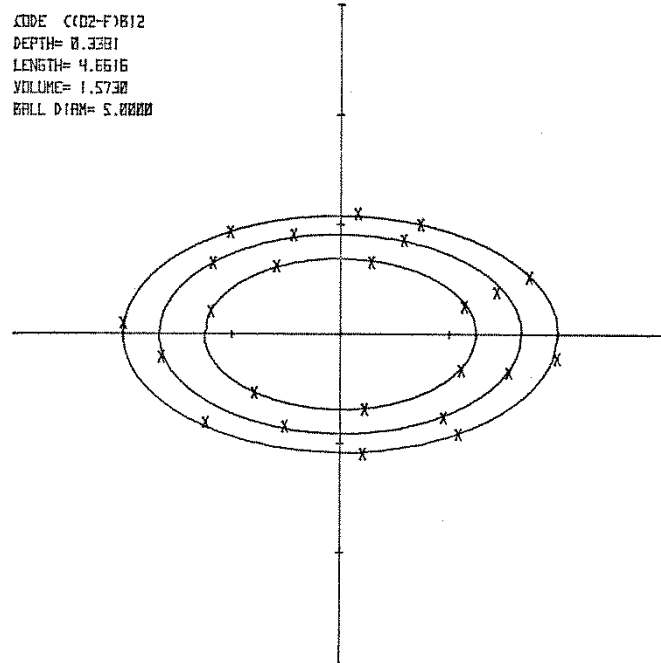


Figure 4.3

The crosses are digitised points from fringes of the previous moirégraph. The concentric ellipses are derived from a mathematical expression fitted to the digitised points, they correspond to the fringes in the moirégraph.

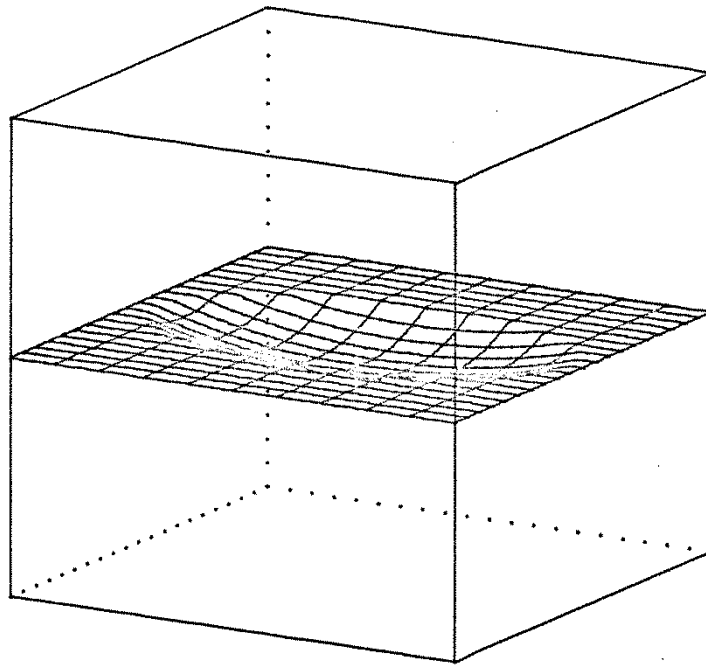


Figure 4 Computer 3-dimensional hidden-line plot of the mathematical expression fitted to the moirégraph of figure 4.2. The lip of the crater has been suppressed.

The spacing of the contours in this technique, and hence the sensitivity, can be varied by re-positioning the light source and camera.

$$\text{Moiré contour spacing} = \frac{(\text{line separation of grating}) \times (\text{grating to film distance})}{\text{point light source to optical axis distance}}$$

Typical values of contour spacing, which can be set up using a grating of 19.67 lines to the millimetre, range from about 50 μm to 500 μm . This range can be extended by using a grating with fewer lines to the millimetre which will result in a smaller value of the contour spacing. Diffraction effects limit the usefulness of the technique for contour spacing below about 50 μm but in that regime it is better to use an optical microscope with an interfering objective lens. Laser holograms can be made which possess similar contour patterns. If a hologram is made of a surface with two light beams of slightly differing wavelengths then there will be interference fringes present in the final image. The fringes will be contour lines with spacing related to the two wavelengths of light. The measurement of volume in this way is more difficult than by the moiré method.

4.3 Specimens

The following metals and alloys were used as targets in experiments:

- Mild steel (EN1A).
- Oxygen-free copper (fully annealed at 1170 K for two hours).
- Titanium (annealed at 1170 K for two hours).

- Bismuth.
- Nimonic 105T alloy (manufactured by Henry Wiggin and Company).

The Nimonic alloy was taken through a careful heat treatment prior to experiments: heated for 4 hours at 1420 K then allowed to cool in air, heated for 16 hours at 1320 K then allowed to cool in air and, finally, heated for 16 hours at 1250 K then allowed to cool in air.

Every target surface which was to be impacted was prepared by grinding using a series of grades of wet-grinding papers and polished to a final finish with 3 μm diamond paste. All of the results presented in this chapter come from experiments in which 5 mm diameter hardened steel balls were used as projectiles. The balls travelled at a velocity of $130\pm 20\text{ ms}^{-1}$ immediately before the impact at an angle of $20\pm 0.5^\circ$ to the target surface.

4.4 Results

Most of the results in this section are presented in the form of graphs rather than tables. To try to simplify the appearance of the graphs I have omitted drawing curves through any of the points or marking error bars on all of the points. The random error in measuring the change of mass is constant and is shown for one point only on each of the mass loss plots.

All of the impacts took place within an argon atmosphere to help reduce oxidation at high temperatures. In addition to this, control experiments were performed on all of the materials tested, especially at high temperatures, to check for any mass changes in the absence of an impact. The control experiments were performed in exactly the same way as the standard experiments except that no projectile was placed in the sabot. Mild steel and Nimonic targets showed extremes of behaviour in the control experiments: no detectable mass change up to 1150 K was found for Nimonic whereas mild steel showed a systematic increase of mass up to 1150 K. The results of the control experiments are shown in figure 4.5.

It is difficult to assess the error involved in measuring the volume of craters because of the complexity associated with the moiré method. The error is expected to be about 5% of the measured volume. Points with extremes of measured volumes have representative error bars superimposed on them.

The measurement of temperature is accurate in principle to $\pm 0.5^\circ\text{C}$. At high test temperatures it is likely that this figure is greater; at 1150 K the error is probably $\pm 10^\circ\text{C}$ (deduced from considering the rate of cooling of the target). A representative error bar is included on the absolute temperature plot for high temperatures only.

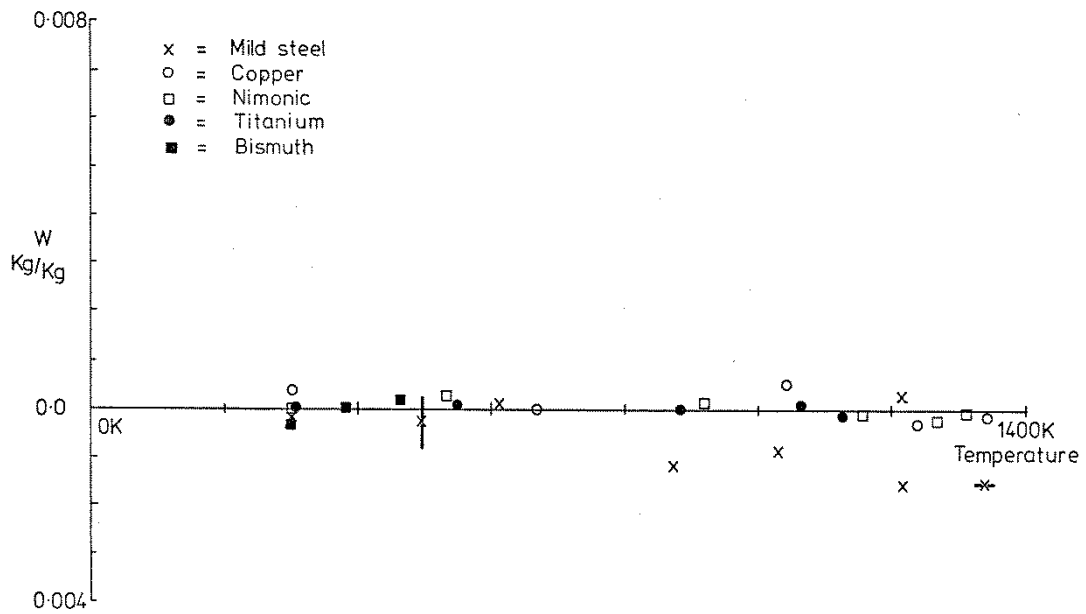


Figure 4.5

Variation of relative mass loss with absolute temperature. These results are for no impacts, they are control experiments. For all metals, except mild steel, no correction to the results is required.

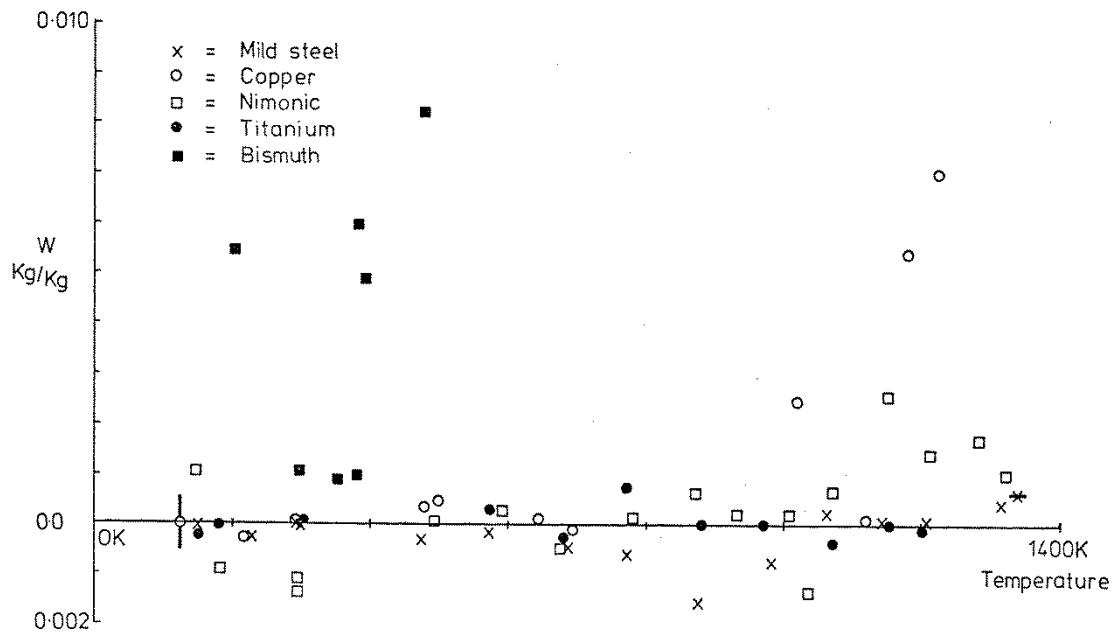


Figure 4.6

Variation of relative erosion, W, with absolute temperature for impact by single 5mm diameter steel spheres (approximately 0.5 gm). No correction to these results has been made.

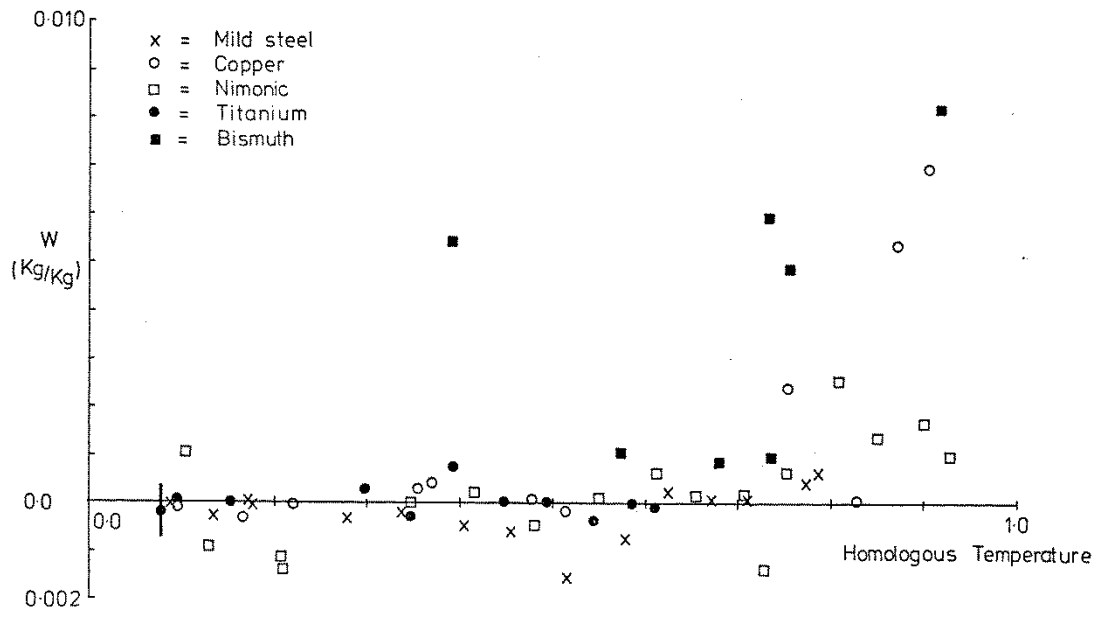


Figure 4.7

Variation of relative erosion, W , with homologous temperature ($\theta = 1.0$ is melting).

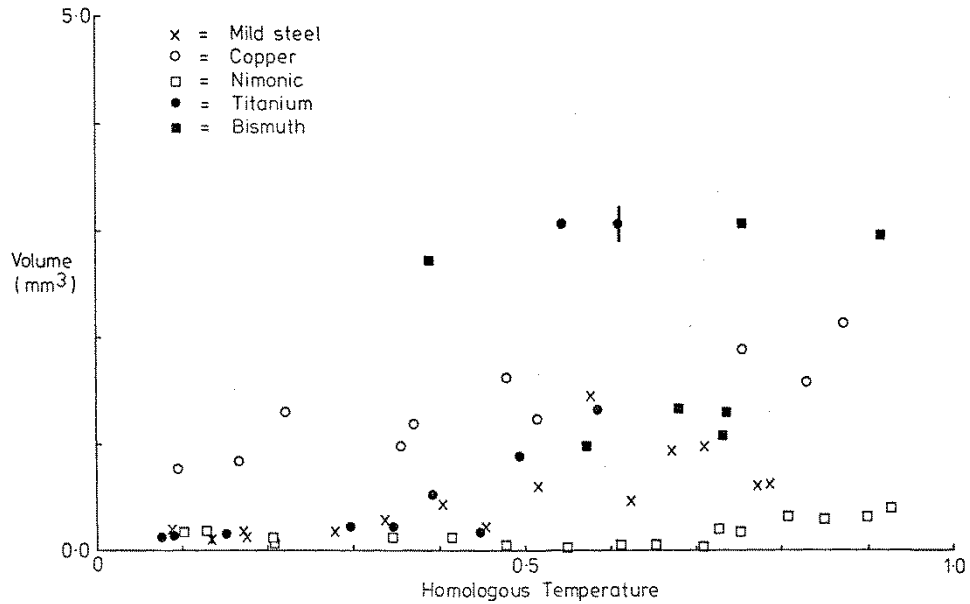


Figure 4.8

Variation of crater volume with homologous temperature.

4.5 Change of Mass as a Result of Impact

Figure 4.6 is a plot of relative mass change (mass change divided by the mass of the projectile) versus absolute temperature for all five materials. No correction for oxidation has been made to any of the points. Note the erratic behaviour of bismuth which is a consequence of its brittle-ductile behaviour. Bismuth has an open structure and appears to fracture easily at high-strain rates; the large losses of mass are due to the target spalling. One of the data points for bismuth has been omitted because it lies well outside the limit of the plot.

Notice that at higher temperatures mild steel, copper and Nimonic alloy all show significant decreases in mass. When the likely effects of oxidation are taken into account the losses of mass are greater for mild steel. The way in which each material loses mass will be dealt with in chapter Five.

Figure 4.7 is a plot of the same data given in Figure 4.6 but in this case the data are plotted against homologous temperature (1.0 = melting temperature). The graph appears to indicate that all of the materials correspond to approximately the same behaviour. For homologous temperatures of about 0.6 to 0.8 the removal of material starts to increase rapidly. This statement cannot be applied to titanium because for this material the experimental temperatures only reached 0.6 on the homologous scale. When a correction for the likely amount of oxidation is made to the data for mild steel they appear to conform more exactly to the hypothesis. Conversely, Nimonic and titanium do not appear to suffer any oxidation over the whole range of temperatures studied. Copper appears to oxidise only negligibly and it is not possible to draw any conclusion for bismuth. The oxidation-rate for mild steel in air at elevated temperatures is several orders of magnitude greater than the one shown here.

Figure 4.8 shows the volumes of the craters formed on the targets as a result of the impact. The data in this case are plotted only against homologous temperature. For all of the materials studied there is an increase of volume with increasing test temperature. Nimonic alloy showed the least significant change of crater volume with temperature (about +100%) whilst, paradoxically, titanium showed the most significant change (about +1500%). Titanium changes its crystal structure from hexagonal close-packed to body-centred cubic at a temperature of 1158 K; perhaps this effect decreases the dynamic hardness of titanium at that temperature. There is no need to make a correction for oxidation in figure 4.8.

There is only a small change of crater volume with temperature for Nimonic, perhaps this is a result of current trends in the design philosophy of materials used in gas turbine engines. Nimonic is used to make rotor blades in the turbine section of aero-engines; it is designed to withstand large centrifugal forces at high temperatures - of primary importance is its creep behaviour at elevated temperatures. Figure 4.8 shows Nimonic is still a hard material even at high temperatures, however, this only appears to have a limited influence on its erosion resistance in this regime.

The reader will recall that equations 2.1 and 2.2 in section 2.3 deal with the volume of target material which could be melted during an impact. γV is the volume of melted material and V is the crater volume. Let us assume that the mass loss, Δm , at high temperature occurs entirely by target melting. Then it is possible to calculate γ from the mass loss and volume plots,

$$\gamma = \frac{\Delta m}{\rho V}$$

Equation 4.4

Material	γ measured	γ^\dagger calculated
Nimonic alloy (strong nickel alloy)	0.3	4.3
Mild steel	0.09	1.2
Copper	0.08	0.7

Table 4.1

Comparison of measured values of γ against calculated values of γ^\dagger . Calculated values are based on data from Smithells (Smithells, 1962), measured values come from data shown in this chapter. Ambient temperature for both sets of data is 1300 K. See sections 2.3† and 4.4.

Notes on table 4.1:

1. γV is the volume of metal which could/was melted during impact.
2. V is the volume of crater formed by the impact.
3. γ measured is the average of two or three results.

Table 4.1 shows some typical measured values of γ for: mild steel, copper and Nimonic alloy. The results are for an ambient temperature of 1300 K, alongside them are corresponding calculations for γ at 1300 K taken from table 2.1. The figures show a fair degree of consistency. Firstly, the order of the measured and calculated values of γ is approximately correct. Secondly, there is only an order of magnitude difference between the observed and calculated values, which is surprising considering the crude approximations made in support of the calculated values. Finally, the measured values are consistently lower than the calculated values, which is certainly expected. If this was not so then more energy would be going into melting the target material than was actually lost by the impacting sphere, alternatively the material constants would be incorrect.

Dynamic hardness is known to decrease with increasing temperature and there has been no allowance for this in the calculated values of γ . If the change of yield strength was to be included then the measured and calculated values of γ would be more nearly equal.

4.6 Conclusion

The data presented in this chapter show that the temperature of a metal target can influence the amount of erosion which it suffers when it is hit by a single hard sphere. The volumes of craters produced by impacts increase with increasing temperature and the extent of the increase depends strongly on the target material. There appears to be a similarity of behaviour between the materials studied when the data for their erosion are plotted against homologous temperature. This suggests that the melting temperature of the target is important in governing its resistance to erosion.

A fair agreement has been found between a simple theory predicting the loss of mass by target melting and the results of the experiments. However, the evidence is not sufficient to support the

hypothesis that target melting has occurred. The conclusion of this chapter is that results only suggest that target melting may have taken place during impacts; furthermore, this is only likely to be true at test temperatures near to the target melting point.

Chapter 5 Qualitative Observations of Single Impacts

5.1 Introduction

Microscopic examination of target craters cannot be made easily with an optical microscope. This is because the depth of focus of a high magnification objective lens is limited by diffraction effects arising from the objective aperture. A large depth of focus, and therefore a small aperture, is essential when examining the craters produced in these experiments (length and depth of the order of millimetres). In general, it will usually be advantageous to use a Scanning Electron Microscope (SEM) because of its great depth of focus.

Specimens were circular and made 12.7 mm in diameter and 3.5 mm thick so that they would fit directly onto standard SEM specimen stubs without any preparation; a Cambridge Instruments S4-10 SEM was used in the observations described in this chapter. It is worth re-iterating at this point that considerable care must be exercised when interpreting micrographs, it is easy to ascribe certain features as the result of a certain process or mechanism when this is not the case.

5.2 Strain Fields

When a hard sphere strikes the surface of a ductile metal forming an indentation or crater the material around the crater is displaced which can result in work-hardening. In general, at a sufficiently large distance from the crater there will be no deformation resulting from the impact - there will be a localised strain field. This field will be three dimensional; it can be examined in the bulk of the material by sectioning.

Although no complete analysis has yet been published of the strain field around an impact site, various workers (Tabor, 1951) (Calladine, 1969) give an indication of what can be expected using the slip-band field analysis. Plastic deformation is produced by shear stresses and it is independent of the state of hydrostatic stress within the deforming body. The shearing action is manifested in crystals by either slip or twinning. Both deformation modes result in a surface change that is evident by either direct observation or can be made evident by etching. It has not been necessary to etch specimens in the work described here.

Figure 5.1 is a SEM micrograph of an impact site on a copper target (annealed and oxygen free) which was at a temperature of 1183 K when it was hit by a 5 mm diameter hardened steel sphere. The angle of impingement of the sphere onto the specimen surface was $20.0^\circ \pm 0.5^\circ$ whilst its velocity was $130 \pm 20 \text{ ms}^{-1}$. The region of deformation is typical of an annealed face-centred cubic structure metal because the material around the entrance end of the crater shows signs of sinking-in. Paradoxically, the exit end shows signs of piling-up which is characteristic of a work hardened metal, this is most likely to be the result of the direction of material transfer during impact rather than work-hardening of the material at the exit end of the crater. The grain size is large in this specimen (2 mm); individual grains can be seen quite clearly. Notice also the smooth regular form of

the crater; this is not surprising because the crater was formed by a sphere - the moiré topography method described in Chapter 4 illustrates the symmetry of these craters.



Figure 5.1

Crater in a copper target which was formed at a test temperature of 1180 K by a 5 mm diameter sphere travelling at $130 \pm 20 \text{ ms}^{-1}$ at an angle of $20.0^\circ \pm 0.5^\circ$ to the target surface. The sphere travelled from left to right.



Figure 5.2

Crater in a copper target which was formed at a test temperature of 130 K by a 5 mm diameter hardened steel sphere travelling at $130 \pm 20 \text{ ms}^{-1}$ at an angle of $20.0^\circ \pm 0.5^\circ$ to the target surface. The exit end of the crater is at top right of the photograph.

Figure 5.2 is a higher magnification view of a copper target which was hit whilst at a test temperature of 130 K. The field of view is a small region around the crater lip in which slip lines can be seen quite clearly. There are one or two surface scratches evident which must have been present prior to the impact, the deviations of these lines indicate the degree of strain which has been introduced.

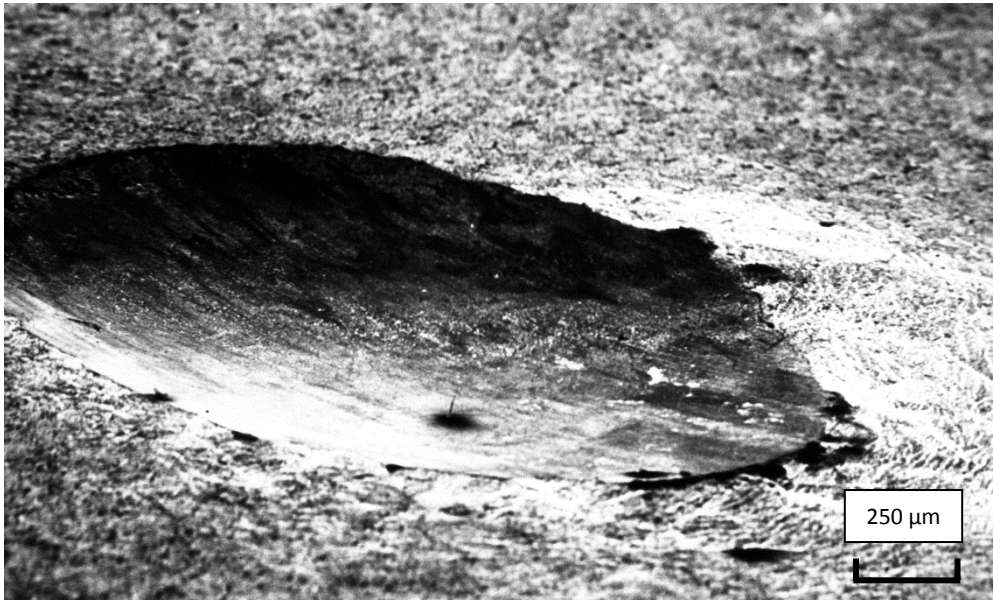


Figure 5.3

Impact crater in a Nimonic 105T target which was formed at a test temperature of 300 K by a 5 mm diameter hardened steel sphere travelling at a velocity of $(130 \pm 20) \text{ ms}^{-1}$ at an angle of $20.0^\circ \pm 0.5^\circ$ to the target surface. The sphere travelled from left to right.

Figure 5.3 is a micrograph of an impact site on a Nimonic target which was at a test temperature of 300 K when it was impacted by a 5 mm diameter hardened steel sphere. The angle of impingement of the sphere on the surface was $20.0^\circ \pm 0.5^\circ$ and its velocity was $130 \pm 20 \text{ ms}^{-1}$. The crater is considerably smaller than the craters produced in copper, this reflects the difference in hardness between the two materials. There is no evidence of either sinking-in or piling-up at the entrance end of the crater and only a slight indication of piling-up at the exit end. The latter observation is certainly due to the transfer of material rather than work-hardening of the surface during the impact because the material was in its fully hardened form - there is only slight piling-up so it is safe to conclude that there has been little target material transfer. Notice that bands of deformation are evident around the crater at the exit end.

Figure 5.4 is a higher magnification view of some of these bands; they do not appear to be as regular as those in copper. The slip lines in copper form parallel arrays whereas those in Nimonic appear to be intersecting. These bands appear to be inter-granular fracture bands.

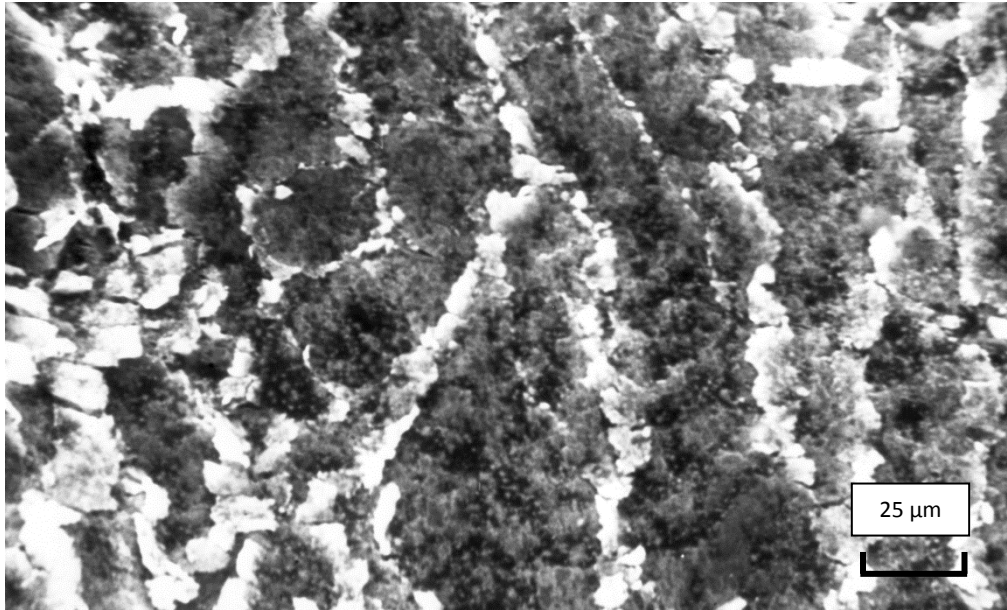


Figure 5.4

High magnification view of region around the crater in figure 5.3 showing deformation bands. The target material is Nimonic 105T.

5.3 Features of Copper Deformation

Figure 5.5 is a SEM micrograph of a copper target which was impacted whilst at a temperature of 1230 K. This crater is remarkable because of the scarring which is evident at its exit end while the rest of the crater is smooth. This scarring is incompatible with the concept of crater formation being due to the transit of a smooth sphere across the surface of a ductile metal, compare with figure 5.1 and with Hutchings et al's work (Hutchings, Winter, & Field, 1976), but this crater was formed by a sphere. Note also in figure 5.5 the particles on the surface of the target around the crater, these appear to be concentrated around the crater exit. This target suffered a substantial mass loss as a result of the impact. I suggest that this scarring is the result of some of the target material melting, in part adhering to the surface of the sphere and being removed with it, in which case the debris around the crater would be the solidified form of particles of molten ejecta which had travelled only a short distance after impact. Many of these particles are partly spherical and all of them are well attached to the surface, which was brushed before examining. Figure 5.6 is a higher magnification view of the crater lip showing a large surface slip line and details of the scarring.



Figure 5.5

View of a crater in a copper target which was at a test temperature of 1230 K. Note the severe scarring at the exit end of the crater.

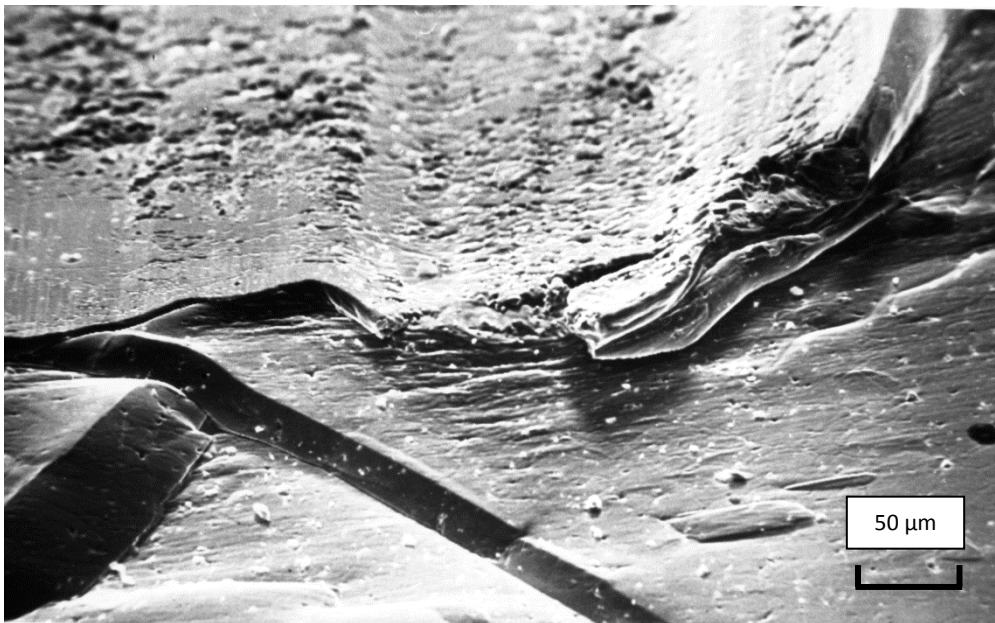


Figure 5.6

Magnified view of figure 5.5 showing region of severest deformation at the exit end of the crater. There was a mass loss from the target as a result of impact.



Figure 5.7

View of the edge of a crater (exit end) showing spherical protrusions in cavities. The crater is on the left and the impacting sphere travelled from top left to bottom left. The crater was formed at a temperature of 230 K. Notice jog-less intersecting bands on the edge of the crater - these are due to twinning.



Figure 5.8

Magnified view of figure 5.7 showing spherical protrusions. The central sphere shows a vortex-like surface. The opposite surface of the cavity shows signs of twinning.

Figure 5.7 is a micrograph of the exit end of a crater in a copper target which was at a temperature of 230 K when it was impacted. Notice the slip lines inside the crater, these lines are not observed in

craters formed at higher test temperatures. Of particular interest are the spherical particles located along the edge of the crater inside a cavity which are found at similar positions in copper targets over a wide range of test temperatures up to half the melting temperature. Figure 5.8 is a higher magnification view of these particles. It would appear that these particles could only have been formed by molten extrusion from the subsurface into a cavity opened during the impact. This target had no measurable mass change as a result of the impact so that, although target melting appears to have taken place, it was insufficient to cause an appreciable loss of material.

The fact that melting appears to be confined to a subsurface location, in the case of low target temperatures ($\theta < 0.8$), has two possible explanations. Firstly, the impacting sphere, which does not deform and therefore generates little heat itself, quenches the surface layer of the target to a depth which depends upon the thermal conductivity of the target and the duration of the impact. Secondly, if the molten region were part of an adiabatic shear-band (Winter & Hutchings, 1975) then it is in this location that it would be expected to be found.

The SEM can be used in several modes. In addition to scanning the electron beam across a small region of the target surface and using scattered electrons to form an image, it is possible to form an image using an X-ray detector (the use of this technique will be discussed later in this chapter). It is also possible to defocus the beam onto one stationary point and scan through a range of target to beam angles- this is the basis of the SEM Selective Area Diffraction mode (SAD). SAD is a commonly used mode in transmission electron microscopy (TEM); when it is used in SEM an X-ray detector is required. The area of the target irradiated by the electron beam is usually ill-defined, in this case it was roughly circular and about 3 mm in diameter. The SAD mode gives rise to a Kossel X-ray pattern image.

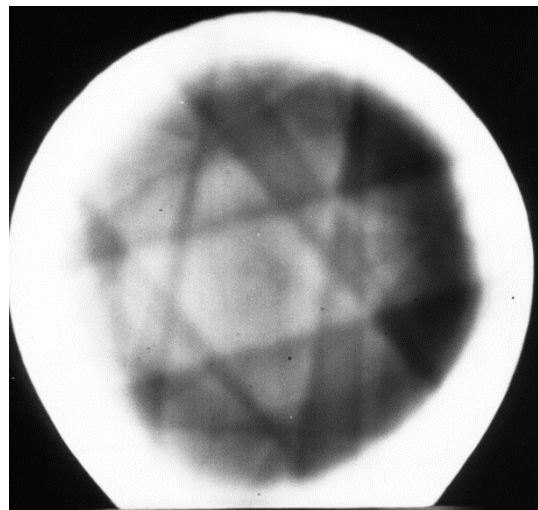


Figure 5.9

SEM Selective Area Diffraction (SAD) pattern from an un-deformed region of a fully annealed copper target. The target had been impacted at a test temperature of 1230 K. A single grain is irradiated by the electron beam and it is oriented with its (111) plane parallel to the surface.

Figure 5.9 is a SAD pattern obtained from a copper target impacted at a test temperature of 1230 K at a position away from the crater. The SAD pattern is characteristic of a single grain oriented with its [111] crystallographic axis normal to the target surface. Inside the crater the SAD pattern

disappeared indicating that the annealed un-deformed target had a grain size of at least three millimetres, whilst inside the crater either the grain size was smaller or the shape was altered.

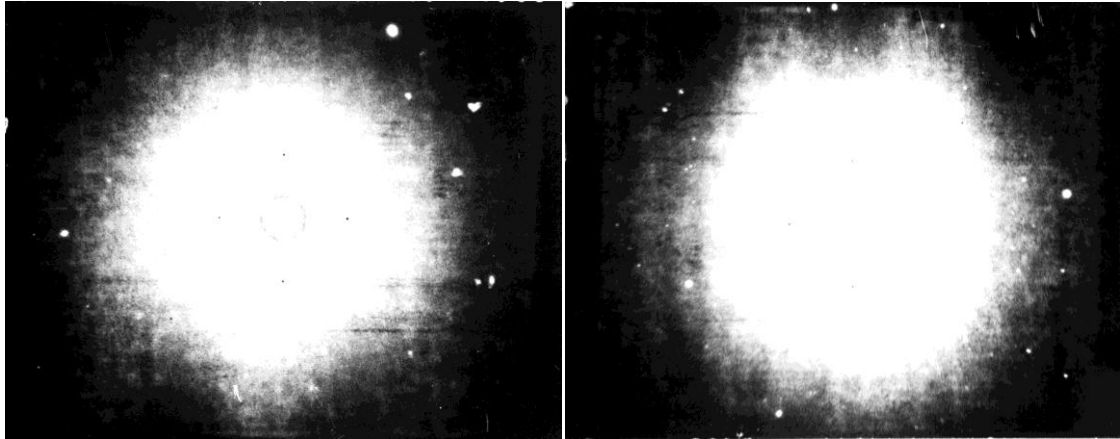


Figure 5.10

Laue diffraction patterns obtained by back reflection from an annealed copper target which was at a test temperature of 1230 K when it was hit by a single 5 mm diameter hardened steel sphere. The pattern to the left is from the undeformed region of the target whilst the pattern to the right is from inside the crater at the exit end.

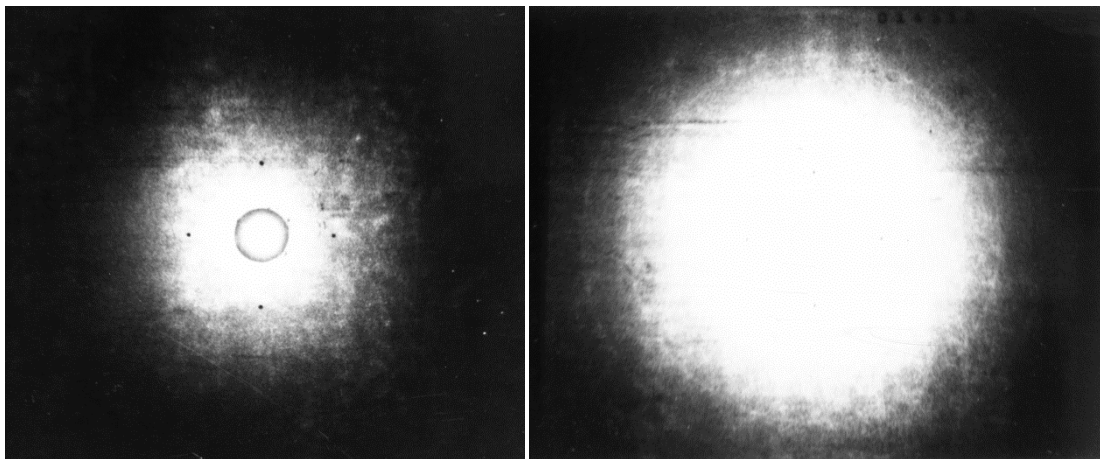


Figure 5.11

Laue patterns from the impacting sphere (left), and copper removed by the sphere (right), which produced the target featured in Figures 5.5 and 5.10. The upper pattern shows no diffraction spots whilst the lower pattern shows powder rings characteristic of very small grain size.

Figure 5.10 and 5.11 show a series of Laue X-ray diffraction patterns obtained by back reflection showing the patterns obtained from the same copper target. In this case the X-ray beam width was 1.0 ± 0.5 mm and the target to film distance was 30 ± 2 mm. The Laue pattern obtained from the undeformed target region indicates that a single grain was present in the beam - in agreement with the SAD result.

Inside the crater, at the entrance end, the Laue pattern is due to only one or two grains in the beam, which perhaps represents a slight refining of the grain size or, equally likely, is the result of the beam straddling a grain boundary. At the exit end of the crater the diffraction pattern was characteristic of

that of a sample of up to five grains - this is a true reduction of the grain size. The sphere which impacted the target was retrieved after the test and was found to have a piece of the copper target attached to it. This deposit showed a radically different Laue pattern, it was composed of a set of concentric Debye-Scherrer rings which is characteristic of a powder of small crystallites - it is unusual to observe such a small grain size in copper. The deposit on the sphere and the material still inside the crater had undergone very similar amounts of plastic deformation; it follows from this that the large difference in grain size can only be the result of their differing heat treatments after impact. The mass of the sphere increased by only 0.2% as a result of the impact, the deposit covered approximately 10% of the surface area of the sphere and it was firmly attached to it. The deposit was therefore in good thermal contact with the sphere and its thermal capacity was small compared to that of the sphere. The increased mass of the sphere accounted for 33% of the mass lost by the target. It follows that the deposit must have been rapidly quenched by the sphere after impact, which was at a test temperature of only 300 K, whilst the target material was allowed to cool slowly from 1230 K to 300 K over a period of one hour. The target material will have undergone considerable re-crystallization in this period and so it is not surprising that it should possess a large grain size.

If target melting had taken place as a result of the impact then this would account for the good mechanical bond between the copper deposit and the sphere. In addition, under the conditions of large super-cooling present on the surface of the sphere and because the surface would also act as a source of many nucleation points for copper crystals, a very small grain size would be expected in the deposit. Mechanical deformation can refine the size of grains, however, fully annealed copper requires a considerable amount of cold working to produce a small grain size. It is not possible that the small grain size present in the copper deposit on the sphere can be the result of mechanical deformation arising from a single impact on the target at 1230 K because Laue patterns from craters in copper targets which were formed at 300 K (that is below re-crystallization temperature) do not show the characteristic powder rings. The only conclusion which remains is that target melting had occurred as a direct result of the impact, that some of the target material was removed because of this melting and that some of it adhered to the surface of the impacting sphere. It is interesting to note that this target is also the one shown in figure 5.5 which has pronounced scarring in its crater - this is also concluded to be the result of target melting.

5.4 Features of Nimonic 105T Deformation

Copper and Nimonic alloy represent extremes of target hardness: annealed copper has a Brinell hardness of 42 whilst Nimonic has a hardness of at least 320. The impacting steel spheres also have a hardness which is commensurate with that of Nimonic: Brinell hardness value 200 to 400, data from Smithells (Smithells, 1962) and, therefore, the spheres will undergo plastic deformation during impact on Nimonic and generate heat.

Figure 5.12 is a SEM micrograph of a crater lip in a Nimonic target, it has three unusual features. Firstly, at the edge of the crater there are spherical particles whose appearance is consistent with the effects of surface tension on solidifying molten material. Their position, at the edge of the crater, is the position at which most shearing takes place and, therefore, also the position where most heat

is generated. Secondly, at the edge of the crater there is a darker band of material, the reason for this shading is not clear at present, however, it will be discussed at a later stage in this chapter. Thirdly, the crater appears to have smeared deposits of material inside it.

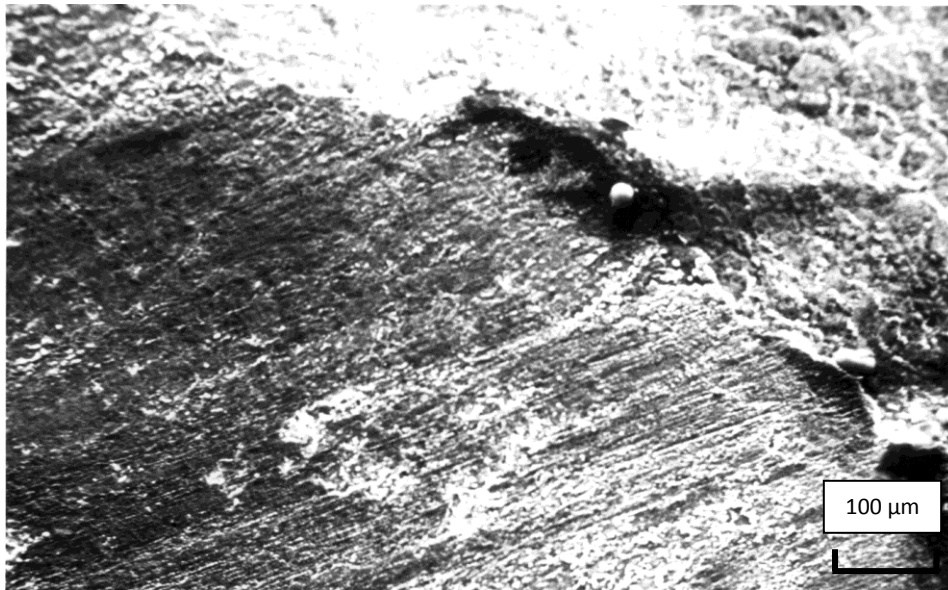


Figure 5.12

The exit lip of a crater produced in a Nimonic target which was impacted by a 5 mm diameter hardened steel sphere at a velocity of $130 \pm 20 \text{ ms}^{-1}$ and an angle of $20.0^\circ \pm 0.5^\circ$ to the target surface. The target was at a temperature of 300 K when it was impacted. Notice the particles grouped at the edge of the crater and the light material adhering to the inside of the crater.

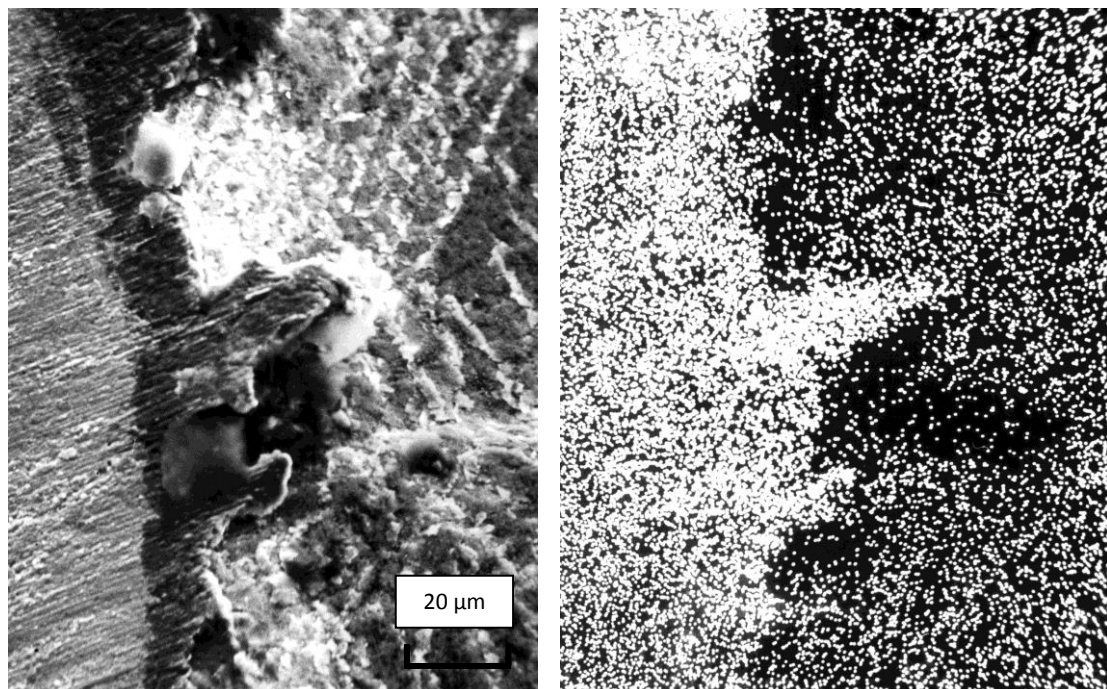


Figure 5.13

Left: higher magnification view of Figure 5.12. 20 μm . Right: X-ray scan showing the iron concentration on the surface of a Nimonic target. The view is identical to the view on the left. The iron deposit is due to material from the impacting steel sphere adhering to the target.

Figure 5.13 (left) is a higher magnification view of the crater lip which highlights some of these unusual crater-edge features. Figure 5. 13 (right) is a view of the same region of the crater but instead of forming the image with electrons scattered from the target surface the SEM displays a computer processed X-ray image from the surface. The computer has indicated on Figure 5. 13 (right) whenever the detector receives signals characteristic of the X-ray peak of iron, hence, the figure is a map of the occurrence of iron in the crater. Nimonic does not contain a significant proportion of iron. The leftmost region of the X-ray scan (the crater) is much lighter than the rest of the figure, however, in the rightmost darker region there appear to be two densities of iron — the lower being nearer to the crater edge.

The impacting steel sphere has undergone plastic deformation during the impact and partly adhered to the Nimonic surface. The sphere was examined after the impact and it appeared to be undamaged apart from a lightly abraded band covering about 10% of its surface area. The mass of the Nimonic target had not decreased but instead it increased slightly. The X-ray scan indicates that there is iron on the surface of the target both inside the crater and away from the crater. The particles on the edge of the crater appear to be regions which have melted and solidified. The darkest regions of the X-ray scans start at these particles and cover an area swept-out by the motion of the departing sphere. I suggest that these regions are relatively devoid of iron because the original target surface was removed by the sphere; the Nimonic could have been in a molten state at this time. The dark band found on the rim of the crater in Figure 5.13(left) has no counterpart in the Iron map of the same region. It may be a region of different microstructure as a result of heating.

Figure 5.14 is a SEM picture of a crater in Nimonic which was at a temperature of 1070 K when the crater was formed. At higher test temperatures, scarring develops within the crater - scarring is a characteristic of erosion by melting in copper targets.



Figure 5.14

A crater in a Nimonic target which was at 1073 K when it was struck by a 5 mm diameter ball travelling at $130 \pm 20 \text{ ms}^{-1}$. The ball has travelled from left to right. Notice the scarring inside the crater which is most noticeable at the exit end of the crater.

Figure 5.15 (left) is a SEM micrograph of the exit end of a crater in Nimonic which was made at a test temperature of 1320 K. Figure 5.15 (right) is an iron concentration map of exactly the same field of view. These two pictures were produced in the same way as Figures 5.13 (left) and 5.13 (right). The only difference between the targets was the temperature at which the test was performed. At the higher test temperatures there appears to be no iron adhering to the crater, which is certainly not the case at low test temperatures. It is unlikely that the hardness of the Nimonic decreases appreciably as the test temperature is increased because the volumes of the craters do not increase greatly. Similar sized craters can only be produced if the target dynamic hardness is constant. It is still likely that the impacting ball has been abraded as much at high temperatures as it was at low temperatures, but why is there no iron in the crater? I suggest that it is because the entire surface layer of the crater has been removed taking with it any abraded iron/steel coming from the ball; this is most likely to be the result of the target melting.

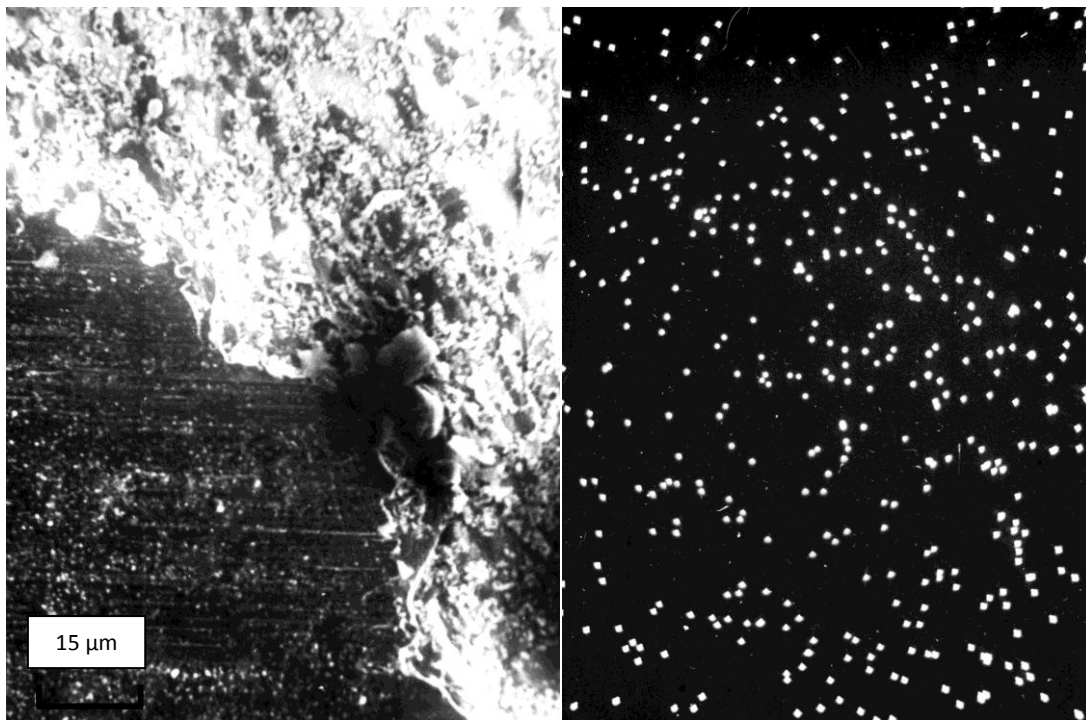


Figure 5.15

Left: view of the exit end of a crater in a Nimonic target which was produced by a ball striking the target (left to right) at a speed of $130 \pm 20 \text{ ms}^{-1}$. The target was at a temperature of 1323 K during the test. 15 μm . Right: X-ray analysis of the same view of the Nimonic target as in left. The white dots show the distribution of iron on the surface of the target. This map shows no localisation of iron.

5.5 Features of the Deformation of Mild Steel (ENIA)

Hutchings (Hutchings I. M., PhD Thesis, 1974) has studied extensively the craters produced in mild steel by the impact of single spheres. He showed that above a critical velocity, which was dependent on ball size and density, it was possible for a lip of target material to be detached. He called this type of erosion *ploughing*. At projectile velocities less than the critical the lip may be formed but it will

not detach; at projectile velocities much less than critical no lip will be formed. At low temperatures no lip was found to form around craters in the experiments which I have performed.

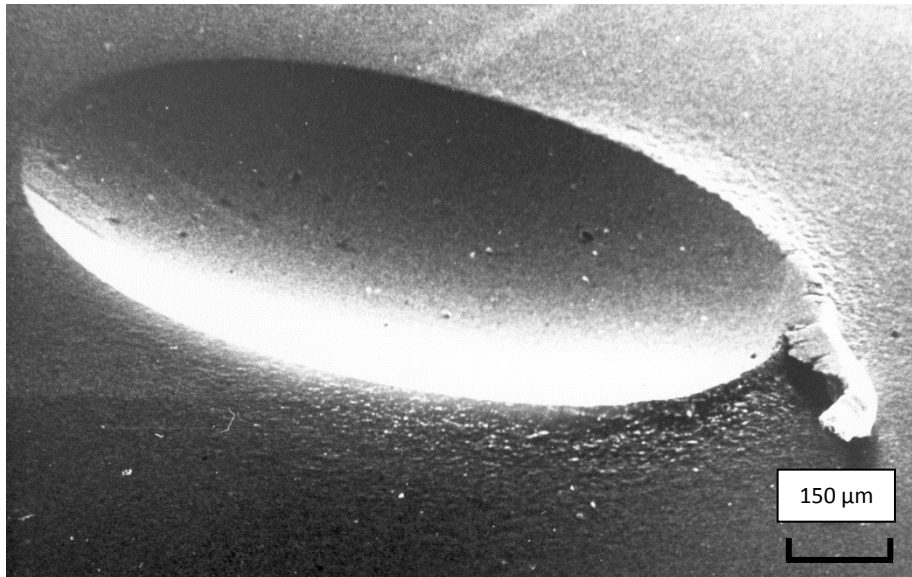


Figure 5.16

SEM view of a crater in a mild steel target which was at a temperature of 1143 K when it was struck by a ball travelling at $130 \pm 20 \text{ ms}^{-1}$ at an angle of 20° to the surface. The ball travelled from left to right. Notice the partly detached lip raised at the exit end of the crater. A lip is not raised by similar impacts at 300 K.

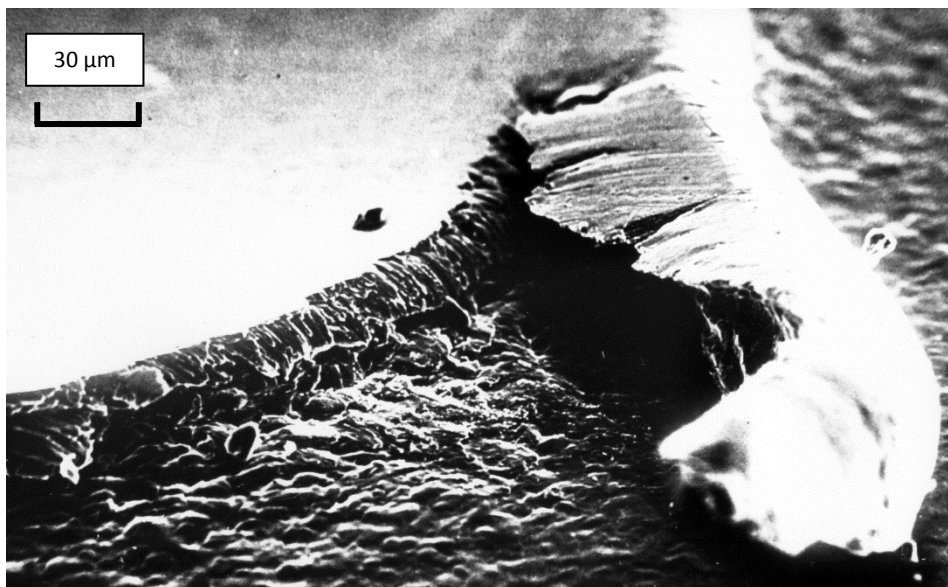


Figure 5.17

Higher magnification view of the partly detached lip in Figure 5.16. The process of detaching appears to have progressed from one side of the crater towards the other.

Figure 5.16 is a SEM picture of a crater in mild steel which was made at a test temperature of 1150 K. At the exit end of the crater, a partly detached lip is plainly evident; this lip does not form at low temperatures. Figure 5.17 is a closer view of the lip; it has started to detach by failing along the

length of a thin, extruded strip of material at the edge of the crater, identical to the failure mode found by Hutchings. This way of losing mass appears to be quite different to that found in copper and Nimonic at high test temperatures.

5.6 Features of Titanium Deformation

Titanium is remarkable among the five materials studied in this work. I have found no detectable loss of mass as a result of impacts over the whole range of test temperatures (150 k to 1250 K). However, the sensitivity to temperature of the crater volume in titanium was the greatest amongst the five materials. Perhaps titanium should only be compared to another simple metal such as copper. Unfortunately, there are significant differences between these two metals: firstly, titanium has a higher melting point than copper (1950 K compared to 1356 K); secondly, titanium changes from having a hexagonal close-packed lattice to being body-centred cubic at a temperature of 1158 K. Finally, titanium has a density roughly equal to half that of copper. Apparently, titanium is susceptible to shearing adiabatically (Winter & Hutchings, 1975).

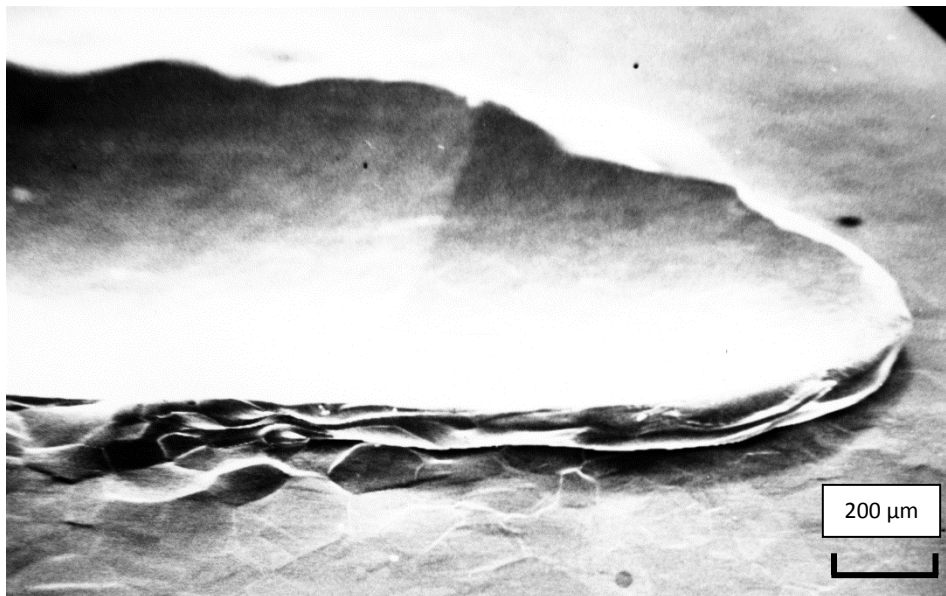


Figure 5.18

SEM picture of the exit-end of a crater in titanium which was at a temperature of 1200 K when it was struck by a ball travelling at $130 \pm 20 \text{ ms}^{-1}$. Craters produced in Titanium are very large at these elevated temperatures. The ball travelled from left to right.

Figure 5.18 is a SEM picture of the exit lip of a crater in a titanium target which was formed at a test temperature of 1200 K. The notable feature of this picture is the length of the lip of the crater; it is nearly equal to one third of the length of the crater. Titanium must be highly ductile at these temperatures. Notice also the ridge inside the crater, which is evident in Figure 5.18. The forming of such a ridge could be the result of either, the arrival of a stress wave in the target during the impact or, the lip relaxing after the impact and pivoting about the ridge. Figure 5.19 is a high-magnification view of a crater lip in titanium, the lip was produced by an impact whilst the target was at a temperature of 1160 K. Notice how the lip appears to be stratified and folded; it can be argued that such stratification is caused by adiabatic shearing.



Figure 5.19

Lip raised by the impact of a steel ball on a Titanium target. The 5 mm diameter ball was travelling (left to right) at a speed, prior to the impact, of $130\pm 20\text{ ms}^{-1}$ at an angle of 20° to the surface. The target was at a temperature of 1160 K when it was struck. Notice the stratified appearance of the lip, which is an indication that the lip material has been very highly sheared.

5.7 Features of Bismuth Deformation

Bismuth has an open structure which is rhombic. When bismuth melts its volume decreases; its melting point is low for a metal (544 K) and it has a high density (roughly equal to lead). It can deform in either a ductile or a brittle manner.

Figure 5.20 is a SEM picture of a crater of bismuth made whilst the target was at a temperature of 300 K. The smooth, regular outline of the crater can be seen quite clearly; this appearance is characteristic of ductile deformation. Also visible in the crater are a large number of cracks, the largest of which seem to be running in a direction perpendicular to the direction of travel of the ball during the impact. The pattern of cracking appears to be inter-granular. Large cracks can be seen on some targets which run across the diameter of the specimen. Figure 5.21 is a high-magnification view of one of the small cracks; it appears to be narrow and deep.

Some of the targets showed signs of losing material by spalling, which accounts for the large variation of mass-loss measurements. Spalling appeared to be more common at test temperatures near to the melting-point, however, it was not confined to this regime.



Figure 5.20

Almost a plan view of a crater in Bismuth produced by a ball travelling at $130 \pm 20 \text{ ms}^{-1}$ at an angle of 20° to the surface. The Bismuth target was at a temperature of 300 K when it was struck. Notice the unusual cracks in the target whilst the shape of the crater can still be seen - these are characteristics of both brittle and ductile behaviour.

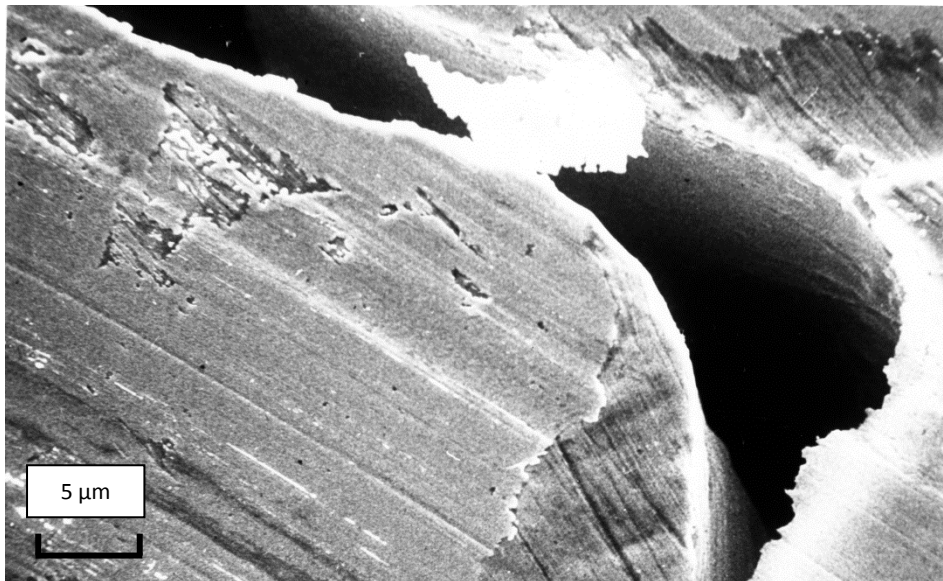


Figure 5.21

Higher magnification view of Figure 5.20. This shows a close-up of a crack in a Bismuth target. The crack is deep compared to its width and the walls of the crack appear to be very smooth.

5.8 Conclusion

The five metals studied in experiments have shown different behaviour in response to impact by hard spheres. Copper commences losing mass by target melting at elevated temperatures and it is likely that Nimonic alloy does the same (copper and nickel both have face-centred cubic lattice structures and nickel is the primary constituent of Nimonic alloy). There is a critical velocity for the formation and detachment of lips on mild steel targets, this velocity appears to be dependent upon temperature. At low temperatures no lips are formed on the craters, at high temperatures the lips form and can be detached during impact. Titanium appears to show a very high ductility which may be responsible for this material's negligible erosion over a wide temperature range. The size of craters produced in titanium is strongly dependent on the temperature. Bismuth exhibits both ductile and brittle response to impact, the brittle behaviour appears to be responsible for its very poor erosion resistance.

Chapter 6 Statistics of Real Erosive Particles: Towards a Geometric Classification

6.1 Types of Erosive Particles

Particles commonly responsible for causing erosion are usually angular in shape but recently considerable interest has centred on the study of spherical particles impacting metal surfaces, however, some work has also been carried out on the impact of square-sectioned plates onto metal surfaces. How do real erosive particles compare with these idealised forms?

Solid particle erosion is usually caused by sand, quartz, sea-salt grains, fly-ash or pulverised coal. Sizes of typical eroding particles can range from 1 to 500 μm or more and these can be either amorphous or crystalline. They are often harder than the surfaces they erode, although they may also be more brittle.

It is highly desirable to be able to classify a given sample of eroding material and thus predict its erosive capabilities according to its shape and mass. A common way of generating statistical data which indicates the average shape of a sample of grit is by using the following index:

$$\text{Shape Index} = \sum_{i=1}^n \frac{\text{Radius of corner}_i}{n(\text{Radius of largest circle})}$$

where there are n corners on the particle considered. Figure 6.1 is a pictorial representation of this index as it might be applied to a typical sand grain. The shape index has a value of 0.0 for perfectly angular particles and 1.0 for spheres. The average shape index of a sample of particles will be a good indication of the shape of an average particle.

Various authors have studied single impacts for two simple projectile shapes: spheres (Hutchings, Winter, & Field, 1976) and square—sectioned plates (Hutchings I. , 1977). Resulting in three categories of impacts:

1. Ploughing impacts - resulting from spheres.
2. Impacts of square-sectioned plates which forward rotate.
3. Backward rotation during impacts by square-sectioned plates.

Material removal has been observed for only two of these cases - no removal has been observed for impacts of forward rotating square-sectioned plates.

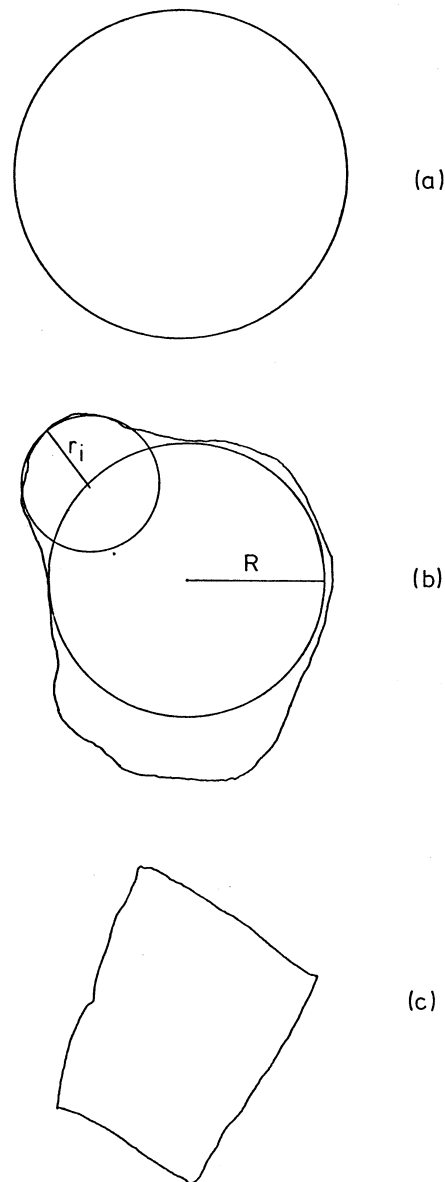


Figure 6.1

Sketches of typical erosive particles (magnified 100 times): (a) glass bead. (b) sand grain. (c) carborundum. A pictorial demonstration of how to calculate the shape index is shown in (b). The radius of the largest inscribed circle and the radius of corner i are superimposed.

6.2 Correlation between Shape Index and Impact

The number distribution of the shape index has been measured for three grits of broadly differing shapes; these grits were: glass beads (500 to 420 μm), sieved sand grains (500 to 420 μm), and sieved carborundum grains (420 to 353 μm). The grits were all of approximately equal sieved sizes. A good statistical sample of about 60 grains of each grit was used in each test. The grits were examined under a Vickers optical microscope operating in transmission mode and a sketch made of many of the grains in each sample. From these sketches the shape index distribution was plotted —

the results of this survey are shown in Figure 6.2 which shows three normalised histograms, one for each grit sample.

The glass beads were the most nearly spherical of the three grits that were examined having a mode of shape index of 1.0, carborundum was the most angular with an index of 0.15, sand had an index of 0.50 roughly half way between the other two samples. The glass beads were remarkable in that although the majority seemed to be perfectly spherical a small proportion were ellipsoidal giving rise to the rather unusual distribution of Figure 6.2.

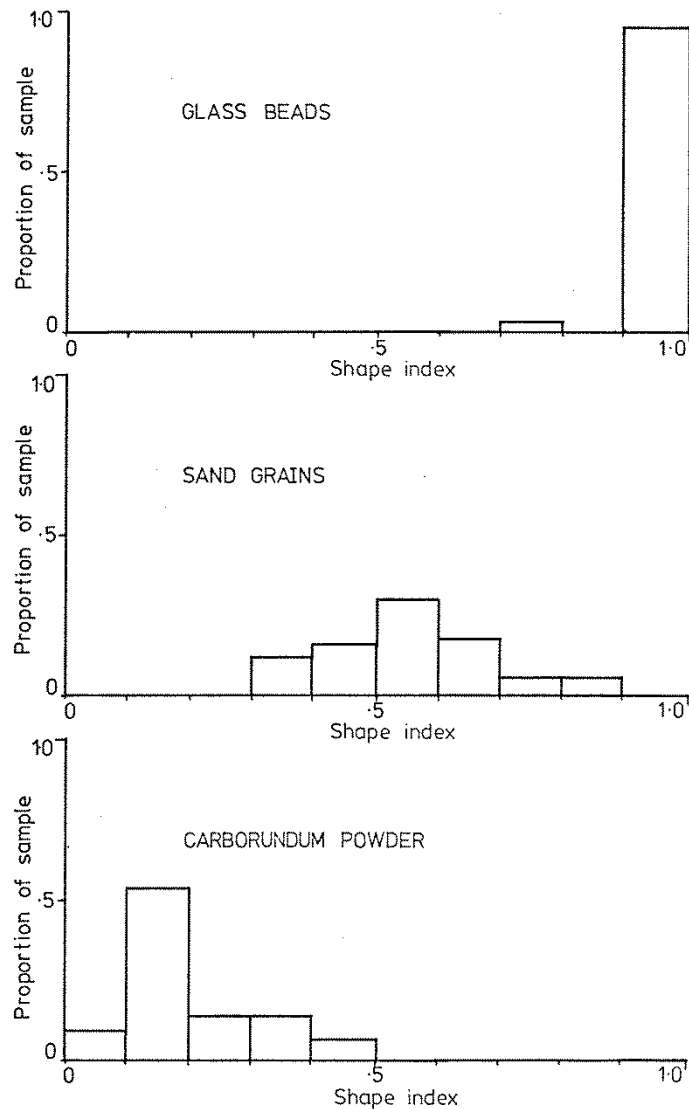


Figure 6.2

Three histograms which show the distributions (normalised) of shape index for the three sample grits studied. Shape index 1.0 = perfectly spherical, 0.0 = perfectly angular.

Next a small quantity of each sample was fired at a polished mild steel target at a velocity of approximately 100 m s^{-1} at an angle of impingement of 25° . The number of grains fired in each test was sufficiently small that the chance of overlapping impacts was negligible. The grains were fired at the target, which was at room temperature, using a laboratory gas gun similar to that described in Chapter 3. The damaged targets were then examined in a SEM to identify which type of impacts had occurred and their frequencies of occurrence.

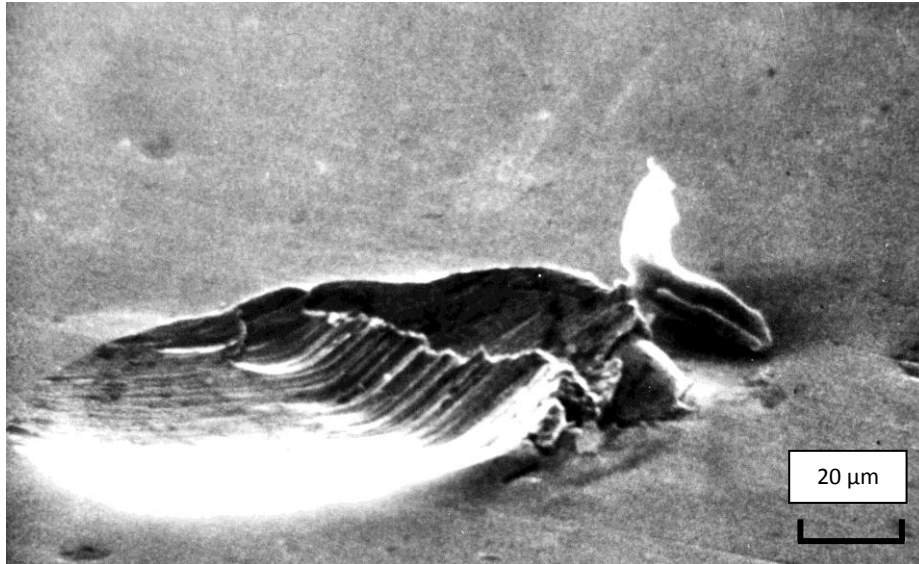


Figure 6.3

A typical ploughing impact produced by a glass bead ($500 \mu\text{m}$ diameter) impacting a mild steel target at 100 ms^{-1} at an impingement angle of 25° .

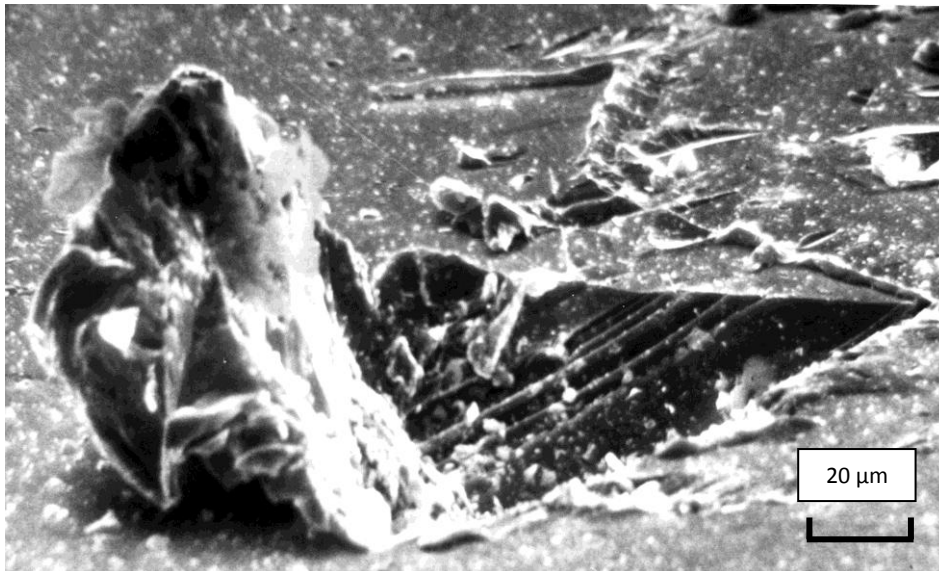


Figure 6.4

A crater produced by a carborundum particle striking a mild steel target at a velocity of 100 ms^{-1} and an angle of impingement of 25° . This crater is typical of the kind produced when the particle rotates forward during impact.

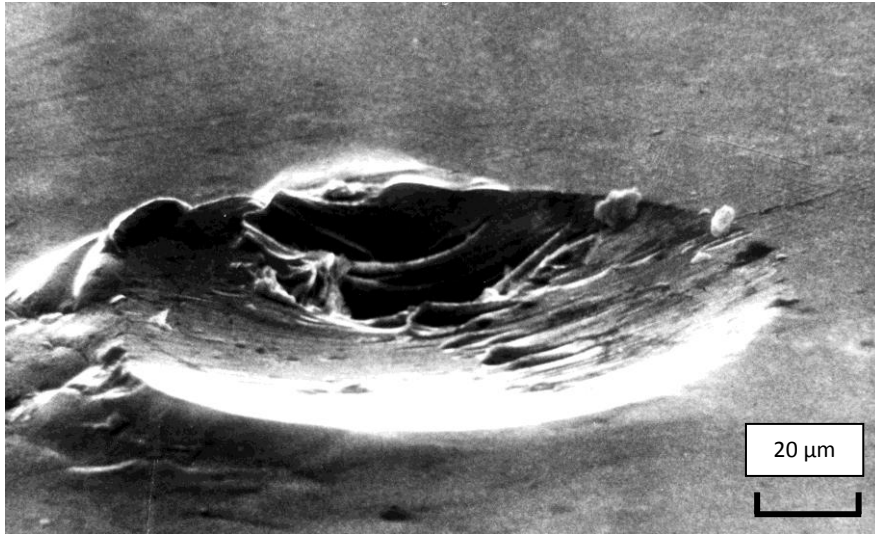


Figure 6.5

A crater produced by a sand particle striking a mild steel target at a velocity of 100 ms⁻¹ and an angle of impingement of 25°. This crater is typical of the kind produced when the particle rotates backwards during impact.

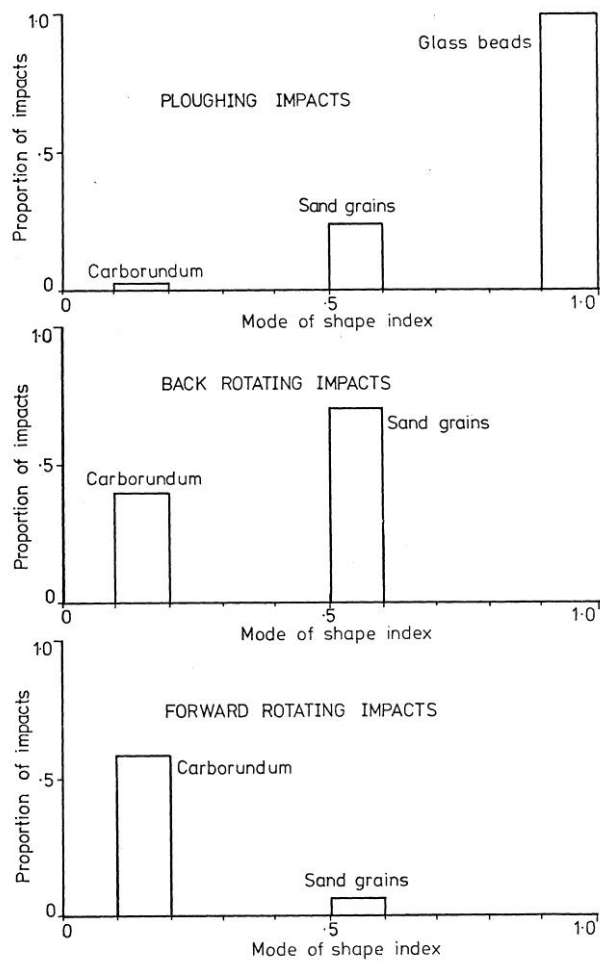


Figure 6.6

Three histograms which show the relative proportions of each class of impact versus the mode of the shape index for each of the three grits studied.

Craters that are typical of each category are shown in figures 6.3, 6.4 and 6.5. The results of the survey of frequency of occurrence have been normalised to show the proportion of the total number of impacts. The proportion of each type of impact has been plotted against the mode of the shape index of each grit, as was plotted in Figure 6.1.

6.3 Conclusion and Discussion

1. Glass beads had the narrowest distribution of shape index; all of the particles were nearly spherical and, without exception, they all produced craters typical of spheres.
2. Carborundum powder was the most angular grit studied; however, its shape index distribution was not narrow, overlapping with that of sand to a fair extent. Carborundum exhibited almost zero occurrences of ploughing impacts - the sample gave rise to almost equal numbers of forward and backward rotating angular impacts.
3. Sand had the broadest distribution of shape index and produced craters falling into all three categories listed in section 6.1, the majority of its impacts were of the back rotating type.

It should be pointed-out at this juncture that a degree of uncertainty existed in classifying some of the impact sites. It is not always possible to differentiate between ploughing type impacts and backward rotating angular impacts - there is a good deal of similarity between the craters of these two categories. The uncertainty might represent as much as $\pm 20\%$ of the proportion of impacts of these classes. That being the case, sand still exhibited a significantly larger proportion of backward rotating angular impacts than ploughing impacts.

The conclusions of this short study are perhaps not very surprising, however, the ramifications are of interest. Forward rotating impacts produce a damage crater without machining a chip out of the surface (unlike backward rotating impacts) and without raising a delicate lip that may be easily dislodged as in the case of ploughing impacts (Hutchings, Winter, & Field, 1976) (Hutchings I. , 1977). Therefore, one would expect, a priori, that if the cutting mechanism of erosion is the dominant one in this instance then carborundum should certainly exhibit a lower rate of erosion than sand, and possibly lower than glass beads - this hypothesis remains to be tested in experiments on multiple particle erosion. If, however, erosion is produced primarily by target melting then one would expect erosion to be independent of the shape index of the sample.

The frequency of occurrence of the two types of angular impact depends on the geometry of the particle at the start of impact. Hutchings suggests that for square-sectioned plates impacting a target the relationship between the rake angle and impingement angle is important in governing the subsequent type of impact (see figure 6.7); he has found that the rake angle is always slightly less than one half of the impingement angle. I have used Hutchings' original computer program, which accurately models the impact of square-sectioned plates onto a perfectly ductile surface, to study this relationship over a range of impingement angles - the results of this are shown in figure 6.8.

It is possible to apply a simple mechanics argument to the problem of the impact of angular particles. The initial rotation of a square-sectioned plate, with zero incoming angular momentum, will be governed by the couples acting on the particle during impact. The couples will act to produce backward rotation if the centre of gravity lies between the velocity vector and the target surface but

the rotation will be forward if the centre of gravity is higher than the velocity vector (see figure 6.7). The subsequent rotation of the particle cannot be so easily deduced because the couples no longer have their points of application at the corner tip. Square-sectioned plates possess fourfold symmetry about the centre of gravity and this means that the angle of rake, which marks the transition from forward to backward rotation (critical rake), is given by

$$\Omega_{critical} = \alpha/2$$

Equation 4.1

where α is the angle of impingement. For cases of initial rake less than this value ($\Omega < \Omega_{critical}$) the particle will start to rotate backwards.

This argument does help to explain the form of figure 6.8, it also gives an insight into what sort of behaviour we might expect from particles that are either less regular than square-sectioned plates or are a random ensemble of shapes. In this latter case, if the particles can be approximated by an ensemble of cubes then the number exhibiting forward rotation can be calculated from the following expression:

$$\text{Proportion of ensemble that rotates forwards} = 1 - \frac{\alpha}{\pi}$$

Equation 4.2

where α is now measured in radians.

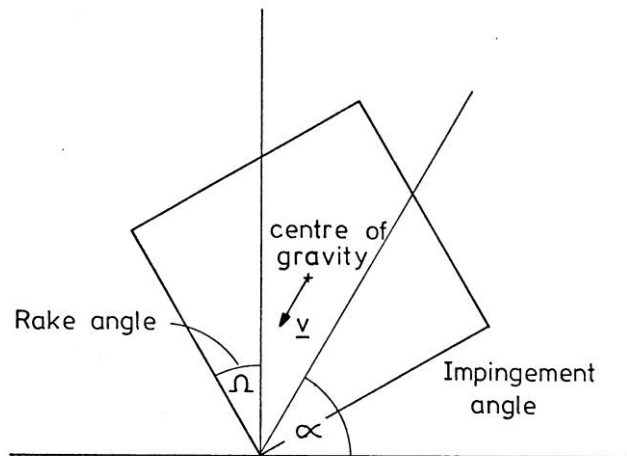


Figure 6.7

Sketch of a square-sectioned plate on the point of indenting a surface. The diagram shows α , the angle of impingement, Ω the rake angle of the leading edge, and the velocity vector v acting through the centre of gravity. Note. Using the engineering definition of rake this angle would be negative, however, the engineering convention is not used in this work.

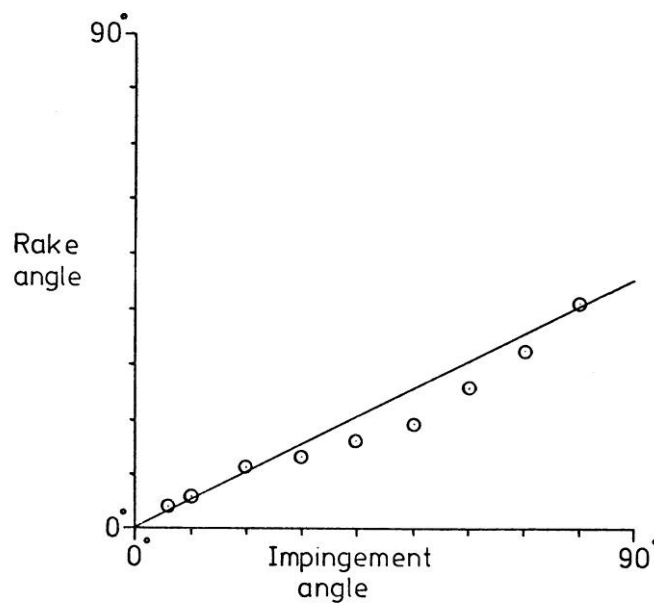


Figure 5.8

Plot of critical rake angle against angle of impingement. The data points were obtained by using a computer program which models the impact of 9.5 mm square-sectioned plates onto a perfectly plastic surface (program developed by I. M. Hutchings). The straight line is the line that would be expected by considering couples at the first point of impact. Note. Critical rake marks the transition from forward to backward rotation during impact.

It is assumed that the cubes strike the surface with random orientations but zero initial angular momentum.

The distributions shown in Figure 6.6 relate to an impingement angle of 25° , it follows that an ensemble of cubes would exhibit 0.86 proportion of forward rotating impacts and only 0.14 backward. Carborundum powder reflected a similar proportion of impacts, therefore, it seems reasonable to assume that at the lower values of shape index (less than 0.5) a sample will behave like a random ensemble of cubes. By way of contrast sand grains do not approximate to this type of particle - they appear to behave more like spheres, as do glass beads.

It is interesting to note that the maximum couple on a cube will only be produced when the impingement angle is very small, i.e. at grazing incidence, or when it is nearly 90° , which is during normal impact. In the latter case, however, there will quickly be reached a stage where the impact becomes like an indentation and the impact produces no mass removal from the target. For this reason all impacts will look like forward rotating impacts at normal incidence.

6.4 Summary

At an angle of impingement of 25° it is possible to correlate the type and relative frequency of occurrence of impacts which will occur if the average index of shape of the sample is known. Samples of particles with an average shape index in the range 0.5 to 1.0 will behave like spheres whilst samples with an index in the range 0.0 to 0.5 will exhibit behaviour normally associated with ideally angular particles, that is square-sectioned plates.

It is expected from this analysis that erosion caused by carborundum will be less severe than that produced by either sand or glass spheres given the same average size of grain and total mass of sample.

Chapter 7 Erosion at Normal Impingement Angles

Finnie's theory of erosion (Finnie I. , 1958) predicts zero rate of erosion at normal angles of impingement. It has been suggested that aerodynamic effects give rise to impingement angles less than 90° when the stream of eroding particles is directed normal to the surface (Finnie A. , 1960). Tilly (Tilly, 1973) has shown that fragmentation of the eroding particles can occur during impact. Both authors suggest that these processes are responsible for producing eroding particles which possess a non-zero component of velocity parallel to the target surface - these particles can now erode the surface in the mode envisaged by Finnie. Hutchings (Hutchings I. M., PhD Thesis, 1974) has looked at the craters produced by single spherical particles striking metal targets at normal impingement angles. The impacting balls were sufficiently massive not to be significantly deviated by aerodynamic forces, especially those near to the target. In addition to this the balls did not disintegrate as a result of the impact. Hutchings detected a loss of mass from the targets as a result of the impacts (see figure 2.1) and associated this with an extruded ring of target material around the impact crater which was not evident after a similar sized quasi-static indentation on the same material.

7.1 High Speed Photography

In this chapter I will describe experiments which are essentially extensions of Hutchings' work. These experiments go on to look at the impact event with a high-speed camera (Hadland Imacon). Figure 7.1 is a schematic diagram of the apparatus used in the experiments. 8 mm diameter hardened steel balls were used as projectiles and they were fired at the target by a gas gun similar to that described in Chapter Three. When the projectile was only a few millimetres away from the target it cut through a beam of light; this event was sensed by a photodetector and used to initiate a further sequence of precisely controlled events:

1. A high-intensity flash-tube was fired. The tube takes approximately $4 \mu\text{s}$ to attain its peak light output; it maintains this intensity approximately constant for about $50 \mu\text{s}$ and then the level of light decreases to zero. The sensing light beam was separated from the target surface by a distance which was sufficient to allow the flash-tube to reach its maximum output before the projectile hit the target.
2. After a delay of $4 \mu\text{s}$ produced by an electronic delay unit, the electronic high-speed camera was started and the subsequent impact was recorded. The axis of the beam of light from the flash-tube was collinear with that of the camera and perpendicular to the direction of motion of the projectile, therefore the photographs are back-illuminated, shadow pictures.

The camera can operate at several framing, rates, three rates were used in these experiments: 10^5 , 2×10^5 , 10^6 frames per second. The number of frames recorded by the camera is variable between approximately 2 and 20. In most of the experiments described here either 8 or 10 frames were recorded, which provides a record of, typically, the first $40 \mu\text{s}$ of an impact. It was usually arranged so that the first instant of contact would be recorded in the third frame.

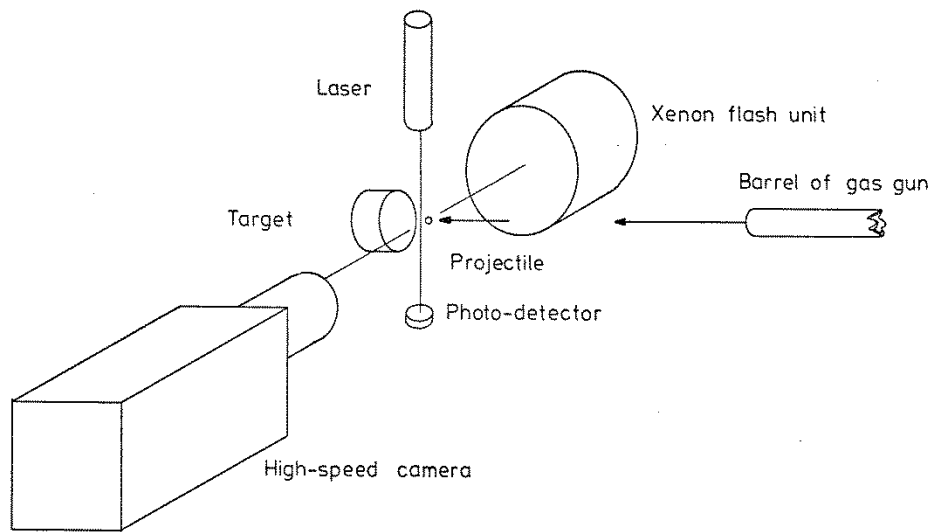


Figure 7.1

Schematic diagram of the equipment used to photograph impact events occurring at normal impingement.

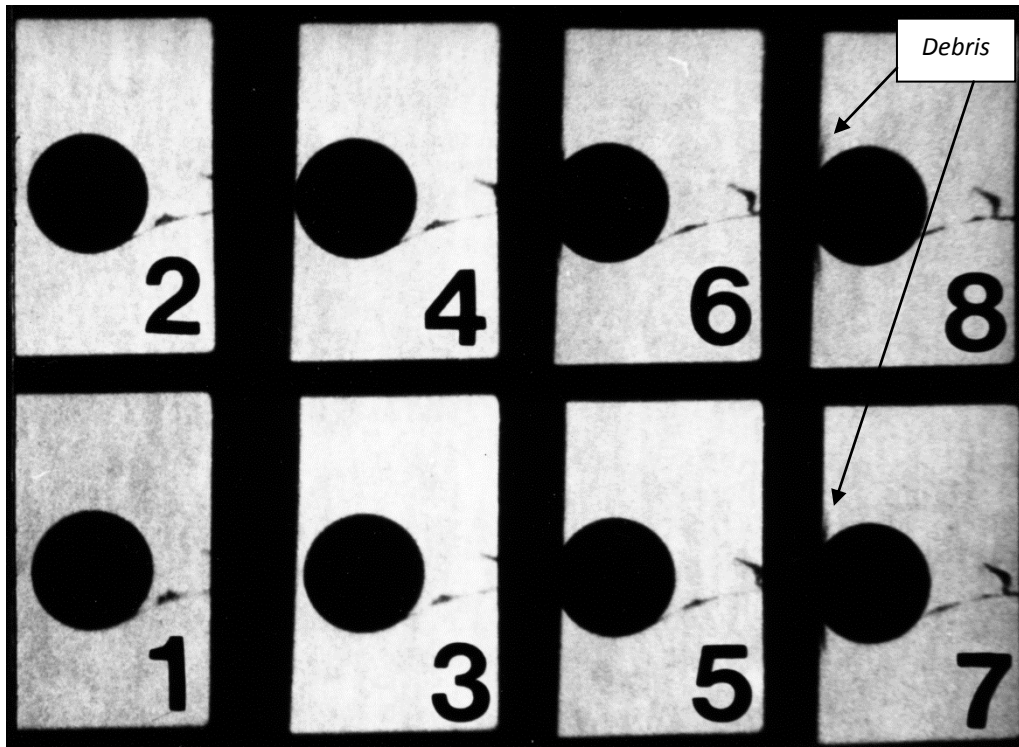


Figure 7.2a

An 8 mm diameter ball impacting a mild steel target. The sequence of pictures was taken with a high-speed camera running at $5 \mu\text{s}$ per frame. The incoming ball is travelling right to left at $107 \pm 20 \text{ ms}^{-1}$. In frames 6 to 8, debris can be seen detaching from the target surface. The debris is travelling at a speed of $320 \pm 150 \text{ ms}^{-1}$.

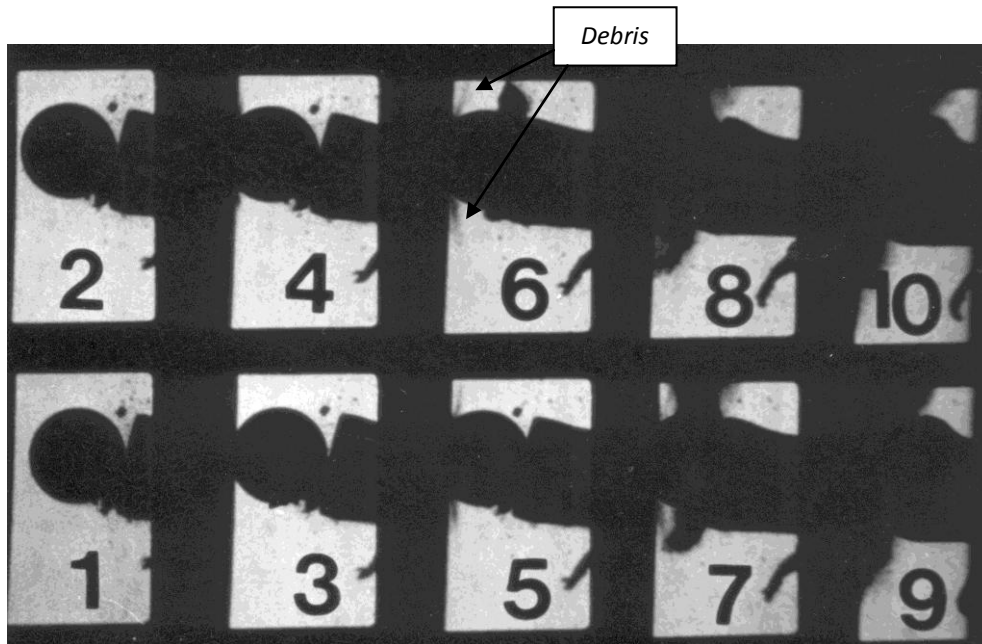


Figure 7.2b

An 8 mm diameter ball travelling right to left at $210 \pm 30 \text{ ms}^{-1}$ strikes a mild steel target. The camera was running at a rate of $5 \mu\text{s}$ per frame. Debris can be seen detaching from the target at a speed of $700 \pm 200 \text{ ms}^{-1}$ (frame 4 onwards).

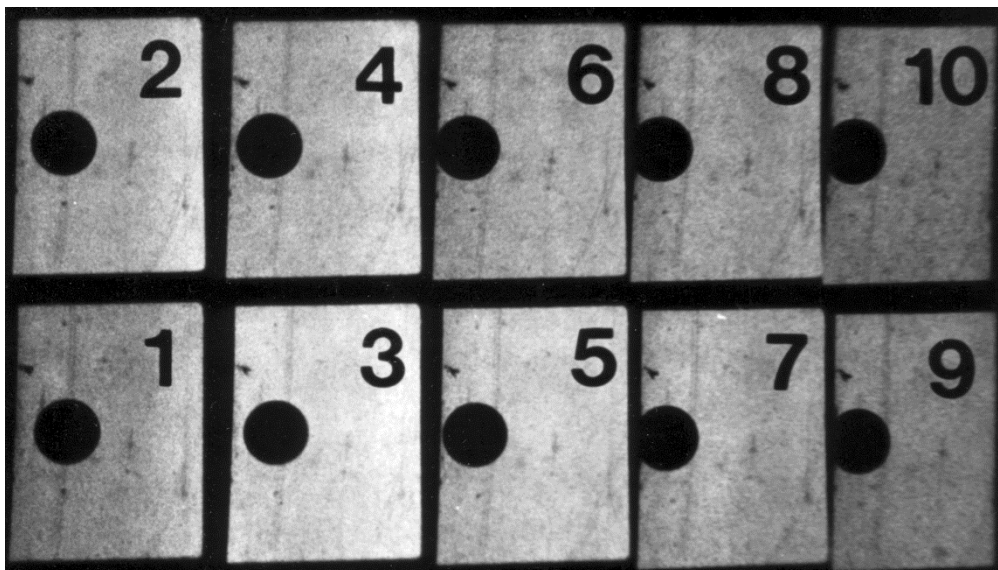


Figure 7.3a

An 8 mm diameter ball travels at $50 \pm 10 \text{ ms}^{-1}$ and impacts a mild steel target. The camera framing rate is $10 \mu\text{s}$ per frame. The debris is ejected from the surface at $200 \pm 100 \text{ ms}^{-1}$ (frames 7 to 10).

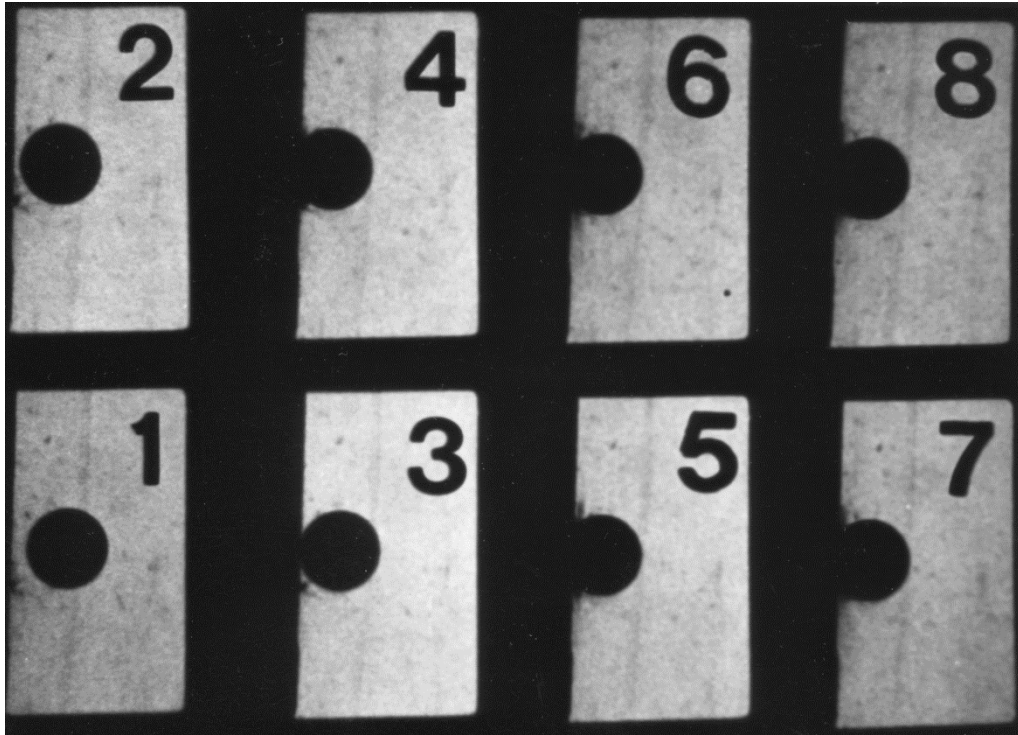


Figure 7.3b

An 8 mm diameter ball travelling at $200 \pm 30 \text{ ms}^{-1}$ strikes a mild steel target. The framing interval is $5 \mu\text{s}$. Debris can be seen detaching from the surface at a velocity of $400 \pm 150 \text{ ms}^{-1}$ (frames 4 to 8).

Two types of target material were used in the experiments: mild steel (ENIA) and annealed copper. In the case of mild steel a loss of mass was detected for all the velocities which were studied (50 to 200 ms^{-1}), however, in the case of copper no similar loss of mass could be detected either by weighing or from examining the photographs of the impact.

Figures 7.2 and 7.3 show four impacts occurring on mild steel targets; these photographs are represented schematically by figure 7.4. In all the cases of detectable mass loss material can also be seen to be ejected from the surface of the target. The target surfaces were roughly polished using wet-grinding papers in the usual manner and they were carefully degreased and dried before each impact. From these experiments it has to be concluded that the material which was lost from the surface was not dust residing there but was in fact target material.

The ejected debris travels at a speed greater than that of the incoming projectile and in a direction which appears to be tangential to the surface of the ball at the edge of contact with the target surface. Chaudhri (Chaudhri, 1980) has suggested that under similar conditions with a brittle target the ejected debris should travel in a direction inclined at 45° to the target surface. This he deduces from the slip-field theory of continuum plasticity; doubtless, however, the surface of the projectile forcibly modifies the direction in the early stages of impact. Chaudhri further argues, from the same basis, that the speed of the ejected material will be equal to $\sqrt{2}$ times the velocity of the incoming projectile. Unfortunately, with the results obtained here it is difficult to estimate the velocity to a good accuracy but it appears to lie within the range 2 to 4 times the velocity of the incoming projectile.

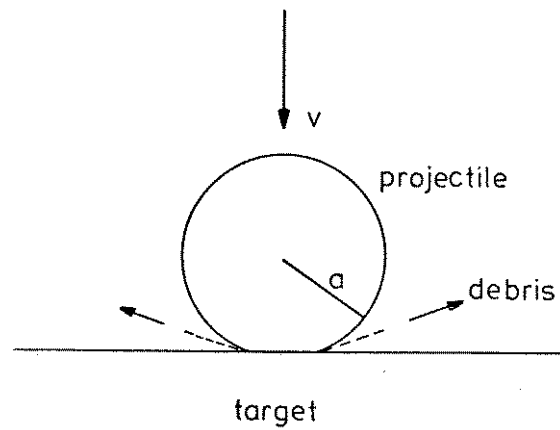


Figure 7.4

Schematic diagram representing how material debris is lost from a target during normal impact.

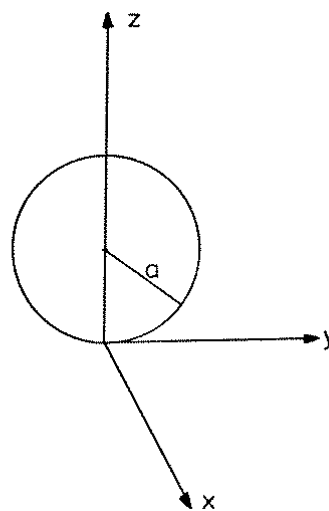


Figure 7.5

Arrangement of axes used in the analysis of a ball impacting a target surface. The ball is of diameter $2a$. The x - y plane is the un-deformed target surface.

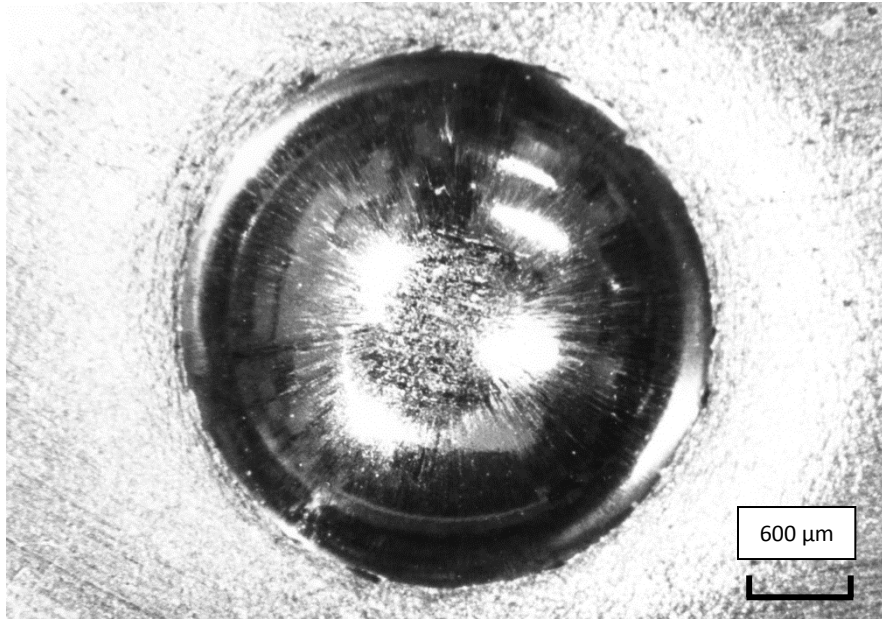


Figure 7.6

Plan view of a crater in a mild steel target produced by an 8 mm diameter steel ball travelling at $200 \pm 50 \text{ ms}^{-1}$. The ball struck the target at normal impingement whilst the target was at a temperature of 300 K. Notice the radial marks inside the crater and the roughly-circular, shiny, central region. Material was lost from the target as a result of the impact.

7.2 Theoretical considerations

It is instructive to consider the behaviour of the deforming region under the impacting sphere. At all times during the impact there will be a circular region of contact. A convenient system of coordinate axes is as follows (see figure 7.5):

- The origin is the first point of contact of the sphere on the target surface.
- The x - y plane is the target surface.
- The z -axis is anti-parallel to the direction of motion of the sphere and passing through its centre.
- Let the radius of the sphere be a .
- Let the speed of the incoming sphere equal v (it will be assumed that the velocity of the sphere during the initial stages of impact is also equal to v). Then the equation of the surface of the moving sphere is given by

$$r^2 + (z - a + vt)^2 = a^2$$

Equation 7.1

where t is the time and $t = 0$ corresponds to the time of first contact. Note that the x and y coordinates have been combined because of cylindrical symmetry, i.e.

$$r^2 = x^2 + y^2$$

Consider the perimeter of the circle of contact between the sphere and the target, this is given by setting $z = 0$ in equation 7.1.

$$r = \sqrt{vt(2a - vt)}$$

Equation 7.2

where the positive root has been interpreted.

$$\frac{dr}{dt} = \frac{v(a - vt)}{\sqrt{vt(2a - vt)}}$$

Equation 7.3

Equation 7.3 is an expression for the velocity of the expansion of the perimeter of contact. Note that in the limit of $t \rightarrow 0$ this velocity is infinite; in the initial stages of the impact the target will only respond elastically. In the limit of $vt \rightarrow 2a$ the velocity is also infinite but this has no physical significance. This expression further assumes v to be constant which will be approximately correct for the initial stages of the impact.

If $dr/dt < v_E$, where v_E is the elastic wave velocity of the target, then the target surface outside the circle of contact can respond elastically to the approaching ball. If $dr/dt < v_p$, where v_p is the velocity of plastic waves in the target surface, then the target surface outside the circle of contact can respond plastically to the approaching ball. For all ductile metals $v_p < v_E$.

Taylor (Taylor, 1946) gives an explicit form for the velocity of plastic waves

$$v_p = (1 + \epsilon) \sqrt{\frac{1}{\rho} \frac{d\sigma}{d\epsilon}}$$

Equation 7.4

where ϵ = strain, σ = stress, ρ = density of the target material and $d\sigma/d\epsilon$ is the slope of the stress-strain curve at the given value of ϵ .

Consider equation 7.3; if $vt \ll a$ then

$$\frac{dr}{dt} \cong \sqrt{\frac{av}{2t}}$$

Equation 7.5

When does

$$\frac{dr}{dt} = v_E$$

when

$$t = \frac{av}{2v_E^2}$$

Equation 7.6

For the case of a typical impact on steel:

$$v_E = 5 \times 10^3 \text{ ms}^{-1}, v = 100 \text{ ms}^{-1}, a = 4 \times 10^{-3} \text{ m}$$

Substituting on equation 7.6 gives $t = 8 \times 10^{-9} \text{ s}$.

The time is very short during which the circle of contact is advancing more rapidly than the elastic waves on the target surface - this time should be compared to the total duration of the impact which is 50 to 100 μs .

Figure 7.6 is a still-photograph of one of the impact craters in mild steel. Within the crater there is a central, roughly circular, region which is highly reflective. Outside of this area there is a region that has radial marks upon it: these appear to be associated with radial flow. It seems reasonable to link the marks with the mechanism for the loss of mass from the target. If this is the case then what significance should be attached to the central, unmarked region? I suggest that within this region the condition $dr/dt > v_p$ holds true and that at the perimeter of the region $dr/dt = v_p$. This assertion is made for the following reasons:

1. There must exist a central region where $dr/dt > v_p$.
2. If $dr/dt > v_p$ then there will be an opportunity for surface frictional forces to develop between the impacting sphere and the target. These forces may have been relieved by small elastic strains but not yet by the larger plastic strains so they will exert large surface tractions. Further deformation in the target surface will be resisted by these forces resulting in the shiny appearance.

If the radius of this central region is b then it is possible to calculate the velocity of the plastic wave. Equation 7.3 can be modified to the following form:

$$\frac{dr}{dt} = \frac{v}{r} \sqrt{(a^2 - r^2)}$$

Equation 7.7

There is a geometric effect which must also be included: the surface plastic wave will be travelling tangentially to the surface of the sphere. If θ is the angle between the tangent to the sphere and the target surface then

$$v_p = \frac{1}{\cos\theta} \frac{dr}{dt}$$

Equation 7.8

but

$$\frac{1}{\cos\theta} = \frac{a}{\sqrt{(a^2 - r^2)2}}$$

Equation 7.9

Combining equations 7.7 to 7.9 gives the result

$$v_p = \frac{av}{r}$$

Equation 7.10

When typical values are inserted into equation 7.10 such as: $v = 100 \text{ ms}^{-1}$, $r = b = 0.7 \text{ mm}$, $a = 4 \text{ mm}$ then the plastic wave velocity has a value of

$$v_p = 1150 \text{ ms}^{-1}$$

This result satisfies the condition $v_p < v_E$. Taylor's equation (equation 7.4) cautions care in attaching too much significance to this value because the velocity of the plastic wave need not be constant - the velocity is a function of both ε and $d\sigma/d\varepsilon$.

At present it is unknown how v_p is connected with the velocity of the ejected debris. Almost certainly the debris is ejected by extrusion and the plastic wave is likely to play an important role in this mechanism. The foregoing analysis is somewhat similar to that used for calculating the duration of the *water-hammer* pressure, which is generated by the impact of a liquid drop on a surface (Field, 1966). There is also a similar analysis for the case of solid projectiles which has been suggested by Hutchings (Hutchings I. M., 1979), however, he considers the effect of elastic waves only.

7.3 Conclusion

In conclusion, the results presented in this chapter isolate a separate mechanism of erosion which can occur at normal incidence. The mechanism operates even when a single spherical projectile strikes a mild steel target without disintegrating or machining material from the target surface. This mechanism is one which has certainly not been included in Finnie's (Finnie I. , 1958) theory of erosion which is concerned with cutting; the mechanism is much more a consequence of dynamic plasticity in the target material.

Chapter 8 Multiple Particle Erosion Rig

8.1 Introduction

In this chapter I will discuss the design and construction of an erosion rig capable of continuously eroding a target. There is much which has been learnt about the process of erosion through studying single impacts, however, erosion can be aided by the co-operative effect of many particles striking the target. The equipment described in this chapter has been designed to allow the co-operative effects to be studied more easily.

8.2 Acceleration Tube

There are several ways of performing continuous erosion experiments, however, the only truly continuous erosion test is by gas-blasting. All other experimental techniques generate cyclic-erosion data and I wished to avoid this type of experiment (see section 2.4 (iii)). In the gas-blast method it is necessary to accelerate the projectiles along a tube; how long should the tube be?

Finnie (Finnie A. , 1960) has solved the equation of motion of a single spherical particle, of diameter 250 μm and density 3 kg m^{-3} , accelerating from rest in an air stream with velocity equal to 150 ms^{-1} . He finds that the particle must travel a distance of 1.6 m before it has reached a velocity equal to 65% of that of the air stream. In general, he deduces that the distance, x , the particle must travel in order to achieve a velocity of v in an air stream velocity of u is given by,

$$x = \frac{1}{k} \left[\frac{v}{u-v} - \log_e \left(\frac{u}{u-v} \right) \right]$$

Equation 8.1

where

$$k = \frac{3C_d\rho_a}{8r\rho_p}$$

ρ_a = density of air; ρ_d = density of the projectile, of radius r ; and C_d is the drag coefficient. Under the conditions given above k has a value of 0.494 m^{-1} . Figure 8.1 shows a plot of Equation 8.1 for these conditions. As one can see from this figure, x must have a value of approximately 5 m before the particle has reached a velocity equal to 80% of that of the gas terminal velocity. This value of x is still likely to be underestimated because the drag coefficient is dependent upon the Reynold's number of the flow around the particle, which will be zero when the particle reaches the gas velocity. k is therefore a function of velocity and is not a constant.

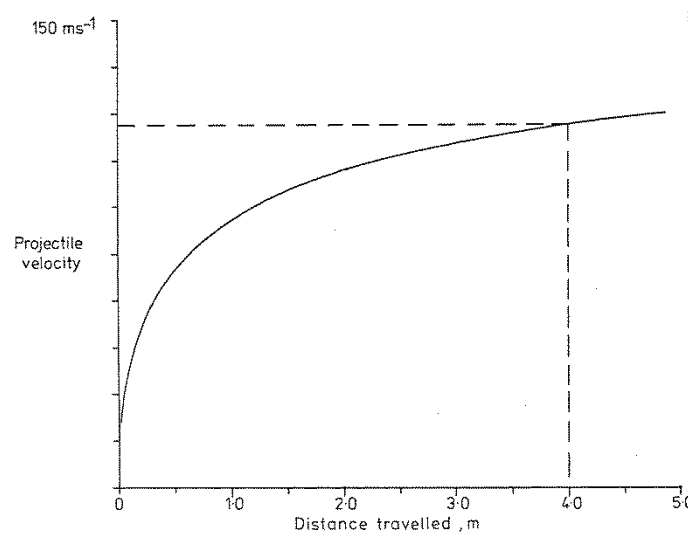


Figure 8.1

Variation of the velocity of a 250 μm sphere in a gas stream of 150 ms^{-1} velocity against distance travelled (barrel length). The dotted line shows the barrel length chosen in the multiple particle erosion rig.

Calculations of this kind indicate that the projectile acceleration tube must be very long but, unfortunately, the viscous drag between the gas and the tube wall then also will be very large, resulting in a very small gas velocity and hence a very small particle velocity. Some compromise is clearly required, with the consequence that it is now also necessary to have an accurate method of measuring the particle velocity and the velocity distribution. This latter measurement is important because we wish to monitor the spread of velocities of impacting particles which must be narrow for the experiment to be meaningful. I chose a value of four metres for the barrel length.

A perfect gas undergoing a free expansion does no work and, therefore, does not suffer a change of internal energy or temperature. A real gas undergoing a throttling expansion will be cooled, this forms the basis of the operation of the refrigerator cycle. In this apparatus gas was supplied from a high-pressure gas cylinder to the acceleration tube via a heating chamber - it is necessary to heat the gas even while performing room temperature experiments. Additional heat could be supplied to the acceleration tube by four coaxial heating coils wound along the majority of the length of the tube. This tube was thermally insulated and contained within another tube made of mild steel, which had a coaxial spiral water cooling coil soldered to it wound along the majority of its length. Up to 16 kW of heat could be supplied to the accelerating tube. The two coaxial tubes were held apart and thermally insulated by asbestos wadding.

The acceleration tube, of inside diameter 22 mm, was made of an impervious ceramic refractory, supplied by Anderman and Ryder. Ceramic was chosen because of its low erosion rate - the erosive grit will strike the tube at glancing angles and ceramics exhibit very high erosion resistance at these angles.

Figure 8.2 is a schematic diagram of the acceleration tube and pre-heater stage. The heating element of the latter was a spiral of silicon carbide, of 1 Ω nominal resistance, powered by a 60 v 60 A transformer — the power reaching the heating element was controlled by a SCR (silicon controlled

rectifier) triac. Figure 8.3 shows the circuit diagram of the transformer and controller; the latter is a modified design, the original being a circuit published by Radiospares using a zero-voltage switch integrated circuit (IC1 in diagram). This design generates a minimum of electrical interference unlike many others based on SCRs. The element was held inside another ceramic tube by two refractory annuli such that both tubes were lying with their axes collinear to that of the acceleration tube. The acceleration tube was joined to the pre-heater by an impervious ceramic cone, thereby preserving cylindrical symmetry and helping to reduce any turbulence effects which might otherwise create back-pressures and make for inefficient operation. All ceramic to ceramic bonds and the only ceramic to metal bond (the gas inlet plate) were sealed using Fortafix cement *TC Caulking Compound*. The pre-heater assembly was mounted inside a double walled brass cylinder and could be cooled with circulating water.

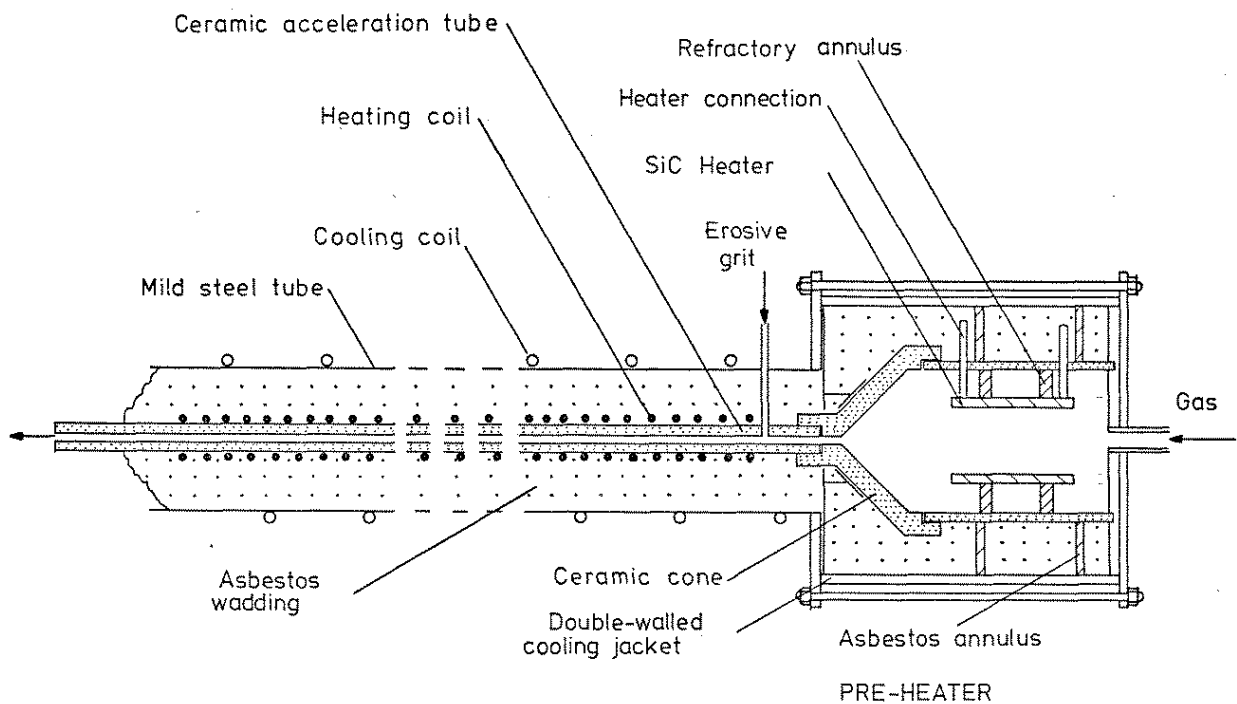


Figure 8.2

Sketch which shows the multiple particle erosion rig barrel and pre-heater stage.

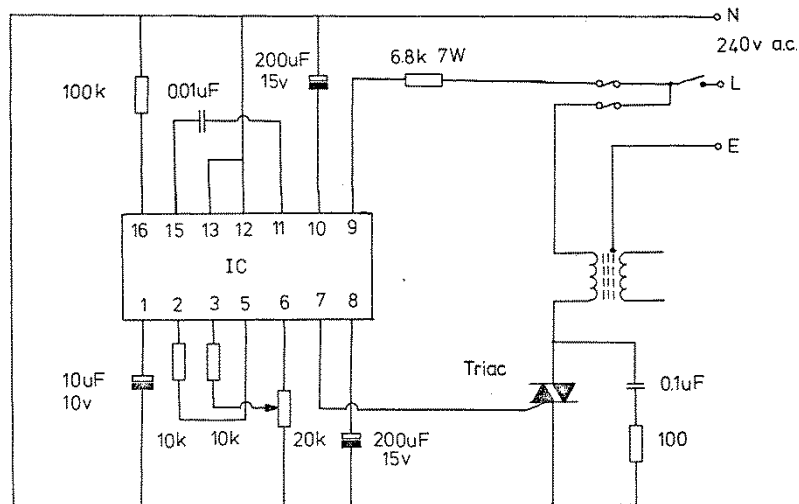


Figure 8.3

Circuit diagram of the power controller for the pre-heater element. IC = zero voltage switch. Triac = 15 A type.

8.3 Grit Ingestion Controller

The eroding grit was fed into the acceleration tube through a small hole near to one end, the end nearer the pre-heater stage. The flux of erosive particles is an important parameter in erosion experiments; in the apparatus described in this chapter the flux could be accurately metered by a rotating disc mechanism. The grit falls under gravity from a hopper into a V-groove cut on the disc, the disc rotates carrying the grit until it reaches a rubber scraper which levels the grit in the groove. The grit is then carried on by the disc to a third point where it is removed by suction. The force of suction is provided by two gas pressures, namely: the Bernoulli pressure generated by the gas flowing along the acceleration tube, and an excess pressure maintained around the disc contained within a glass bell-jar. This latter arrangement had an additional intention, which was to supply a gas and grit mixture suitable for ingestion. An inert gas was used as a propellant, usually argon gas, to eliminate oxidation of the target surface and so the same gas was used inside the bell-jar (see figure 8.4).

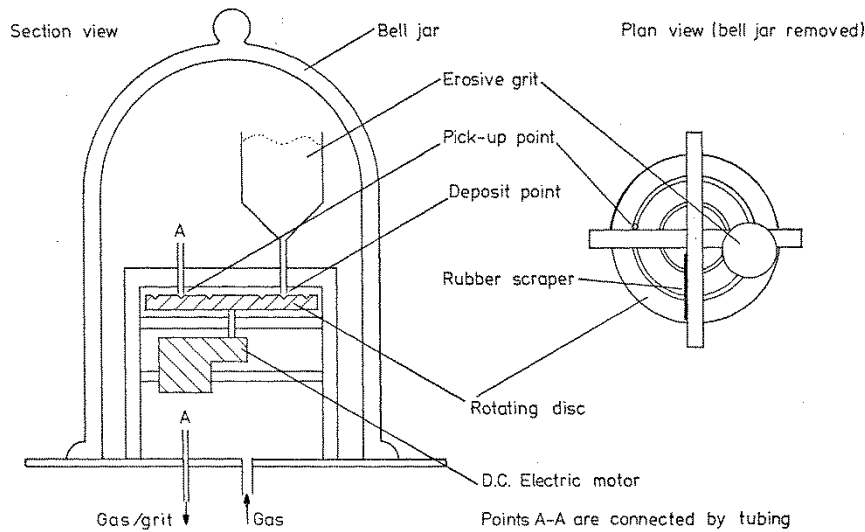


Figure 8.4

Sketch of the erosive grit metering unit which features a rotating disc mechanism.

The rotating disc had three concentric grooves cut in it, the disc was driven by a geared down d.c. electric motor and driven from a 0 to 24 V supply. The motor had a tachometer unit on it which monitored its speed under load, the disc speed was continuously variable over a range of 0 - 0.78 revolutions per second. With this arrangement the erosive agent either: sand, silicon carbide, or glass spheres could be supplied at a rate, R , given by:

$$R = \frac{r\rho h\omega}{2}$$

Equation 8.2

where r is the groove radius, with triangular section of depth equal to h and width l , ρ is the grit density (1670 kg m^{-3} for loose sand), and ω is the angular rotation speed of the disc in radians per second. R will be in units of kilograms per second (kg s^{-1}). The flux, F , of erosive particles is equal to R divided by the cross-sectional area, A , of the acceleration tube.

$$F = \frac{R}{A} = \frac{r\rho h\omega}{2A}$$

Equation 8.3

Using the device described here a maximum flux of $15 \text{ kg m}^{-2} \text{ s}^{-1}$ could be achieved.

I would like to point out that this idea of using a rotating disc is not new. Rolls-Royce (1971) Ltd., amongst others, have used this idea in their erosion rig at their laboratories in Hucknell.

8.4 Specimen Chamber

It was pointed out at the beginning of this chapter, that a considerable saving in both expense and effort could be afforded by using the same specimen chamber for single and multiple impact

experiments. For this reason the reader who is interested in details of either: the specimen chamber, the specimen heating and cooling arrangements, specimen thermometry, or the specimen holder and column is referred to Chapter 3. In this section I will discuss those modifications made to the chamber for the provision of dust extraction.

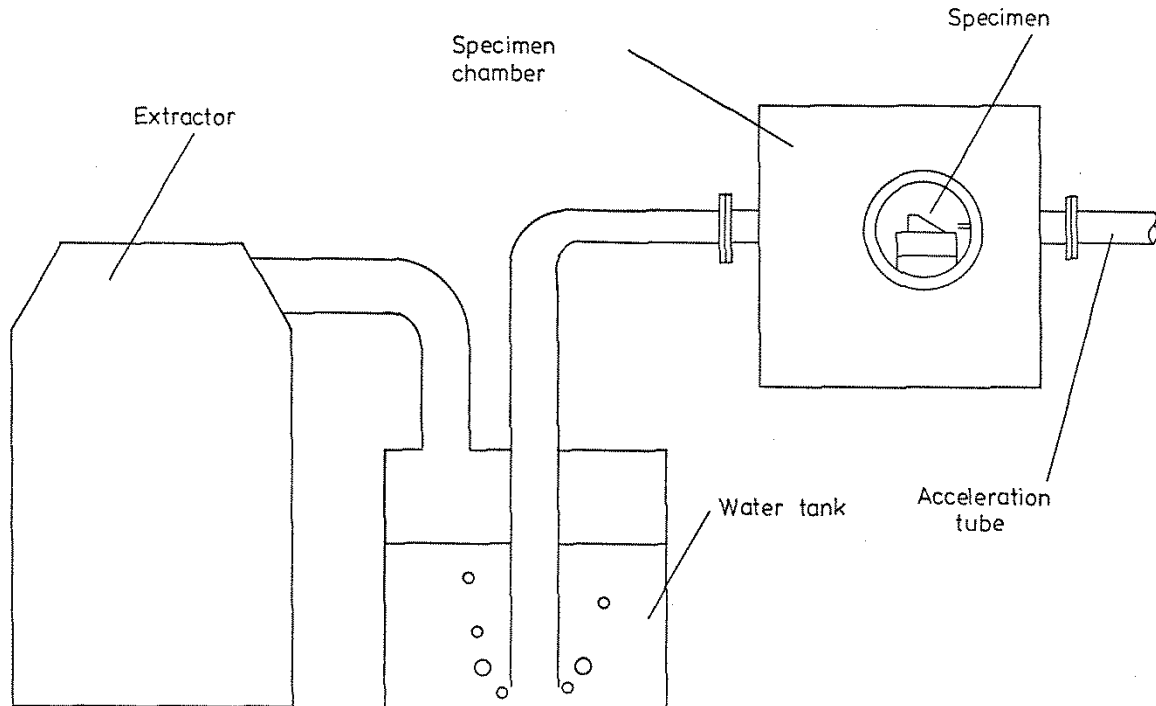


Figure 8.5

Schematic diagram of the dust extraction system used in the multiple particle erosion rig.

Erosion can be the cumulative effect of many years of wear, however, very much shorter test times must be used in experiments, typically a quarter of an hour, dust extraction is still essential even for these short test times. I thought it desirable to extract the erosive grit in a water tank because of the considerable heat energy carried by the grit/gas mixture, perhaps up to 10 M Joules. The hot erodent stream passes out of the specimen chamber after hitting the target drawn by a powerful vacuum cleaner (see figure 8.5) and bubbles through a tank containing 120 kg of cold water. By this means the gas stream is rendered harmless.

8.5 Velocity Measurement

Measurement of velocity is a difficult procedure for single particles of millimetre size travelling at velocities between 20 to 500 ms⁻¹ the problem is considerably magnified when there is a flux of several thousand particles per second to be measured, and the problem is further exacerbated when the particles are only 10 to 500 µm in size. There are a variety of established techniques available for such a measurement, some of which are:

- The laser-doppler anemometry method (Yeh & Cummins, 1964).
- The dual rotating shutter method.

- Use of the streak camera.
- High-speed photography.
- Direct time of flight deduction relying on cross-correlation performed by computer.

I chose to adopt the last method for a variety of reasons and, rather than enter into a long discussion of this method's merits and demerits, I will only point out its main advantages: it is easy to use, it does not interfere with the erosive jet, it is less costly than many of the alternatives, and it is capable of giving a considerable amount of information about the erosive jet. I hope that these advantages will become apparent to the reader in the course of this chapter.

Time of flight: a deduction by cross-correlation

The method of velocity measurement to be described here is an extension, albeit an elaborate one, of the method used for measuring single particle velocity, in which the projectile passes through two light curtains eclipsing photo-detectors and triggering an electronic timer. The technique described here relies on a very similar optical arrangement (see figure 7.6) and uses the same general principle.

In this case, the erosive jet passes through two light curtains, however the particle size is too small to be detected by eclipse, and so the light scattered by the particles is collected by quartz glass rods, and guided by quartz glass fibre optic leads to a pair of photomultiplier tubes (PM tubes). The light curtains are observed in such a way that cross-channel observation does not take place. The light for the curtains is produced by a 750 W tungsten filament bulb, and this is also conducted to the velocity sensing section along fibre optic cables. Low transmission guides can be used in this latter case because there is no shortage of light; whereas only very low levels of light are carried by the quartz cables and therefore they must be of a higher optical quality.

This method of sensing is highly immune to interference from magnetic fields; the PM tubes are very sensitive to magnetic fields and would be disturbed by those used to heat the specimen, but by using fibre optics with a very high transmission coefficient (Rofin Ltd.) the PM tubes can be kept physically well isolated.

The optical sensor is very mobile inside the specimen chamber, it can touch the RF heating coil with no ill effects because it is entirely non-metallic. The ceramic sensor can easily withstand direct radiation heating, and the plastic covered fibre optics were cooled with circulating water by putting them inside plastic water pipes for the majority of their length. The sensor was physically small, with the light curtains being separated by only 2 cm, and overall length only 5 cm. It slides directly onto the last few centimetres of the ceramic barrel, between the RF coil and the barrel, and does not obstruct the flow of the erosive jet. The quartz rods were fixed into holes in the ceramic sensor tube using *Chromix* refractory cement (Fortafix Ltd).

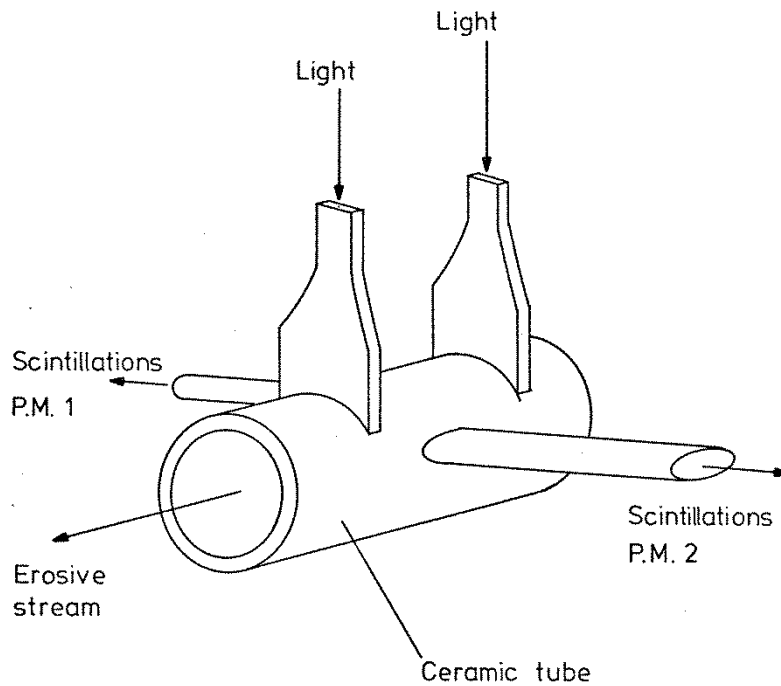


Figure 8.6

Sketch which shows the optical arrangement used to measure particle velocity in the multiple particle erosion rig. The measurement is made prior to the impact of the erosive jet on the target.

The PM tubes (EMI type no. 9698B) require a 2 kV DC power supply which, in this case, was supplied by a commercially made device (Brandenburg type 476R). The sensitivity of the tubes is dependent on their dynode chain voltage. Figure 8.7 shows the circuit diagram for the electrodes of the P.M. tubes. The two tubes were of slightly different sensitivity, and therefore required voltage balancing by a voltage dropping resistor, VRI.

The anode of a PM tube behaves as an almost ideal charge generator; the charge is usually allowed to flow through a resistor to earth but inevitably some stray capacitance, C , will shunt the anode resistor, R , (1 KΩ in this circuit) which will filter out high frequency signals with a frequency greater than f , where

$$f = \frac{1}{CR}$$

Equation 8.4

If the device is to be able to detect a particle travelling at 500 ms^{-1} through a light curtain only 1 mm wide, it must be able to respond at least as fast as this transit time which is only $2 \mu\text{s}$. Therefore, the filtering frequency must be higher than 5 MHz, which implies that the shunt capacitance should be less than 200 pF - a coaxial cable of only 1 m length has a shunt capacitance of about 200 pF. Clearly then a PM tube cannot be expected to drive a cable under these circumstances.

The circuit diagram of figure 8.8 shows a squaring device which also acts as an impedance transformer for the PM tubes. Two squaring circuits were mounted inside a die-cast aluminium screening box along with the PM tubes (and close to them) to help reduce stray capacitance and interference which otherwise might have been very troublesome. The squarer design is based on a high-speed operational amplifier (Fairchild μ A715) and two high-speed comparators (LM319 Texas Instruments). The op-amp works in the current-to-voltage converter mode where the output voltage V_o is related to the input current, I_p , by

$$V_o = -RI_p$$

In this case the feedback resistor R has a value of 10^6 ohms. The anode of the PM tube feeds directly into the virtual earth of the inverting input of the operational amplifier; it is very desirable to operate the anode at earth voltage. The op-amp is protected at its input against voltage spikes, it is also carefully compensated to obtain the highest frequency response (1 MHz) with no oscillations.

The first comparator acts as a squarer and level sensor for the signal; the second comparator is an inverter. The LM319 comparators can drive up to 25 mA of current in their output circuits and turn on or off in about 100 nS; they are capable of driving cables.

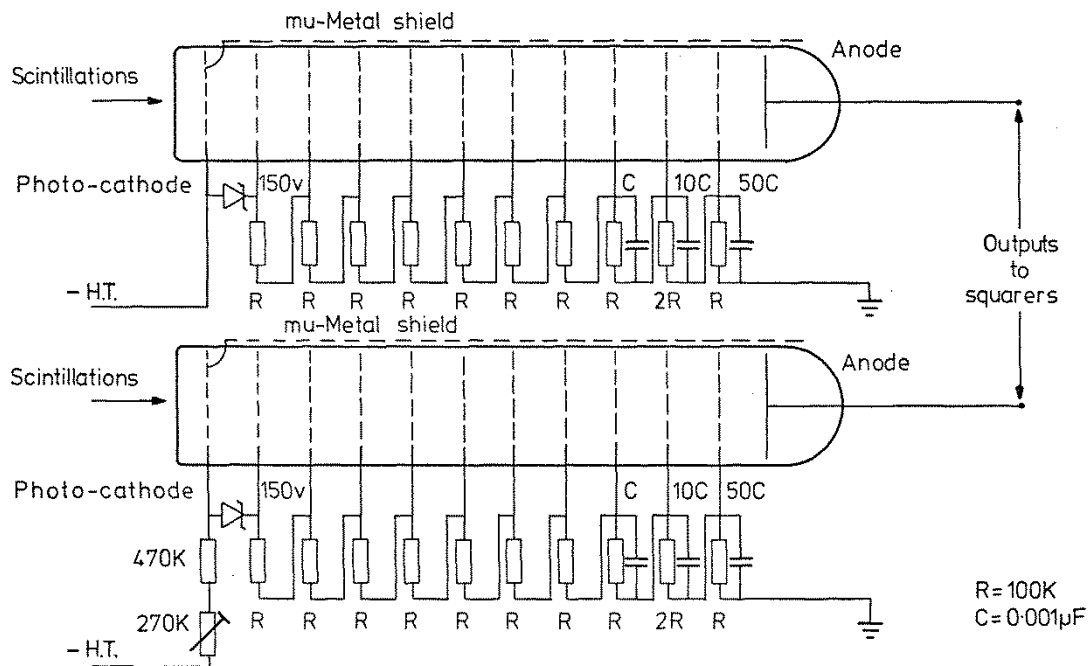


Figure 8.7

Circuit diagram of dynode chain and power supply to the photomultiplier tubes. The tubes have slightly different sensitivities, which can be balanced by adjusting the preset resistor.

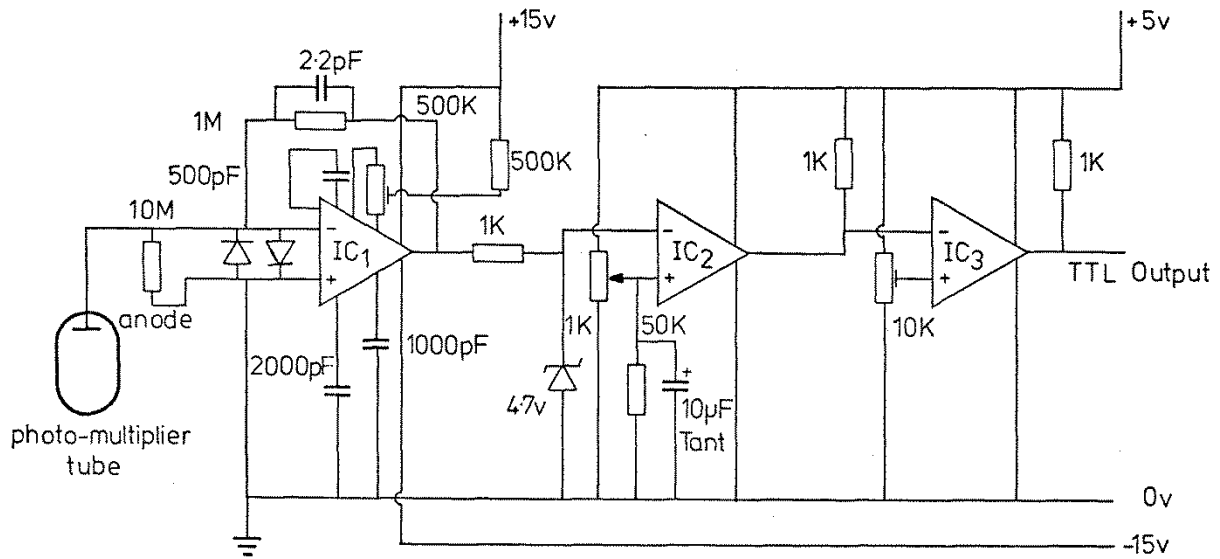


Figure 8.8

Circuit diagram of one photo-multiplier squarer circuit, it has a TTL binary output. The preset resistors, in the non-inverting input resistor chain, are used to set-up a +0.1 v to 1.0 v bias across the variable resistor. The operational amplifier offset control is also shown.

The output signals of each squarer are stored simultaneously in a digital recorder with 8 bit accuracy and 4 K byte store (Datalab Ltd, *Transient Recorder DL922*). The sampling frequency of this device is variable up to 10 MHz per channel. A sample of both channels is stored over a predetermined period and the signal can be displayed directly on an oscilloscope; or it can be punched out onto paper tape, in ASCII code suitable for reading by a computer (Solartron *4070 Facit Punch*), or fed directly in parallel-bit form to a computer via the standard HP-IB/IEEE 488 interface (iTT 2020 Micro-computer). In any case, this technique of velocity deduction depends on a computer program to perform cross-correlation of the two stored signals. The recorder and computer, acting in combination, represents a very powerful data acquisition and data processing unit with scope outside that which is mentioned here - the full 10-bit accuracy of the recorder is not being used in this application, as only binary signals are present at the input.

Figure 8.9 is a sketch of the type of signals that might come from the PM tubes' squarers: the pulses in each channel represent the transit of projectiles through the light curtains. If it were possible to label each projectile then it would also be possible to examine both signals and easily determine the velocity of those projectiles passing through both light curtains - of course this is not the case; we cannot identify individual pulses, they are indistinguishable from one another. If all the projectiles were travelling at the same constant speed, which would be very desirable in experiments, then the two channels would be identical apart from a time shift corresponding to the time of flight of the projectiles between the two light curtains. If this shift somehow can be deduced then the velocity will be known - this is the underlying aim of cross-correlation.

If T is the total time duration stored by the recorder and we assume the second PM tube signal, $S_2(t)$, to be given by,

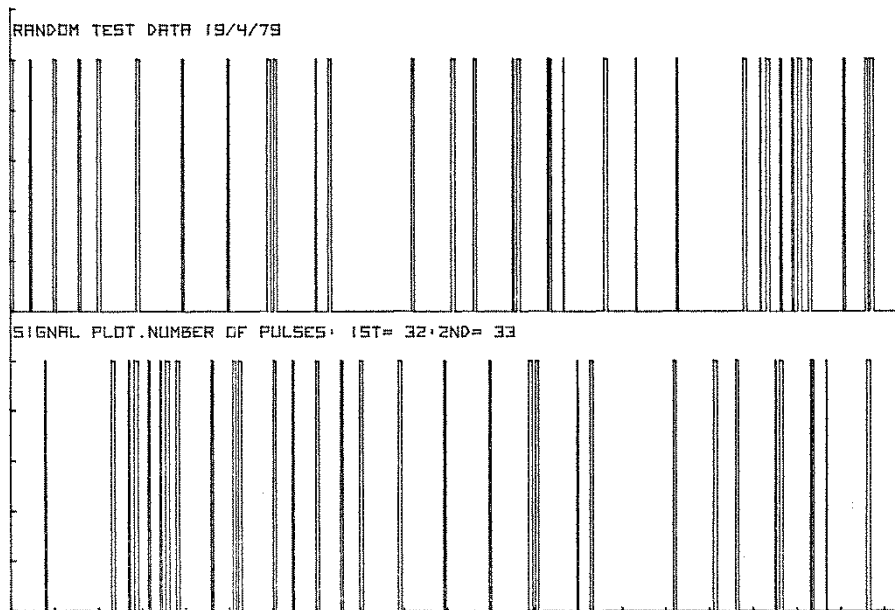


Figure 8.9

Plot of test data which represents typical signals that can be cross-correlated. The data is generated by computer program (see Appendix C) and possess a 600 unit time shift.

$$S_2(t) = V(t) ; \text{ for } 0 \leq t \leq T$$

$$= 0 ; \text{ otherwise}$$

and, because the first PM tube signal will have the same form apart from a time shift, τ_0 , then the signal from the first tube will be

$$S_1(t) = V(t - \tau_0) ; \text{ for } 0 \leq \tau_0 \leq T$$

$$= 0 ; \text{ otherwise.}$$

These signals represent the signals stored by the digital recorder. In general, the cross-correlation function, $\Phi(\tau)$, is defined as the following:

$$\Phi(\tau) = \int_{-\infty}^{+\infty} S_1(t - \tau) S_2(t) dt$$

Equation 8.5

For the sampled time-limited signals V_1, V_2 , in figure 8.9 the integral will simplify to a finite series:

$$\Phi(\tau) = \sum_{t=0}^T V(t - \tau)V(t - \tau_0)$$

Equation 8.6

It is this sum which is evaluated by the computer program (see Appendix C). When $\tau = \tau_0$, this sum will have a maximum value

$$\Phi(\tau_0) = \sum_{t=0}^T V^2(t - \tau_0)$$

Equation 8.7

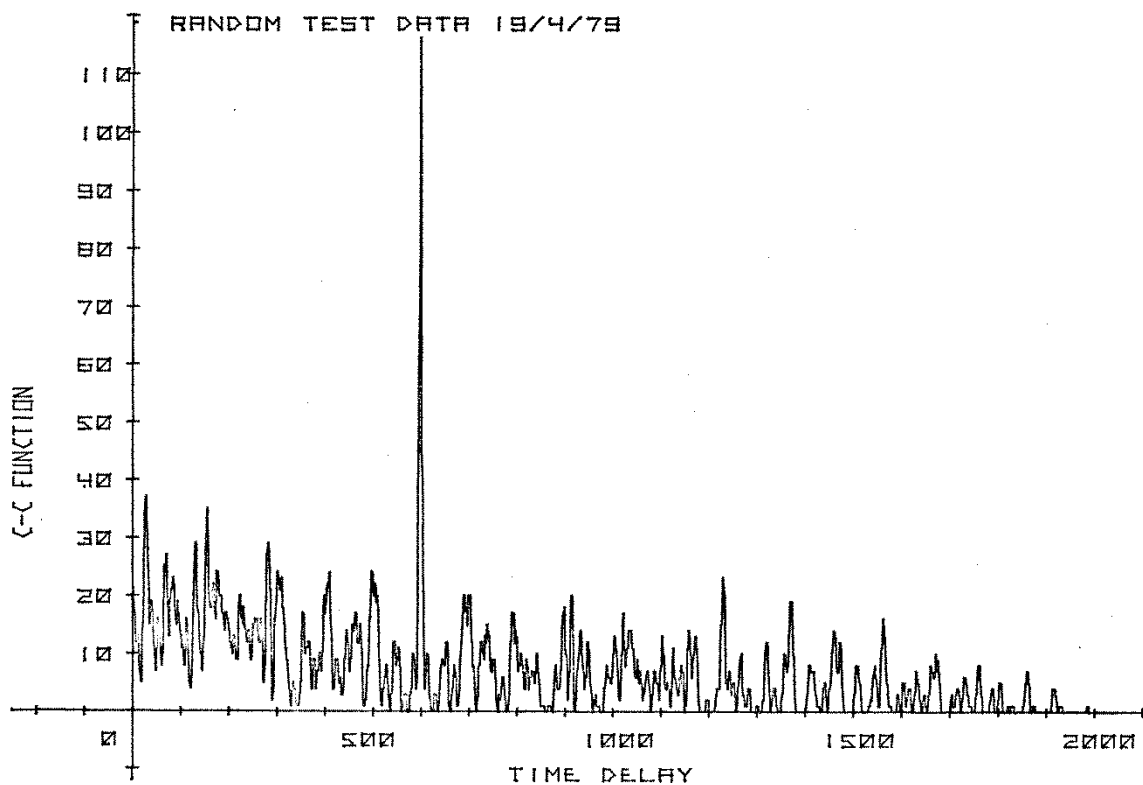


Figure 8.10

Plot of cross-correlation (C-C Function) against time delay, τ , for the signals shown in figure 8.9. The strong peak occurs at a time delay of 600 units, which was inserted into the original test data.

This result follows because:

1. There exist two possible outcomes of the product of the two random pulse sequences, notably
 - a. $V(t - \tau)V(t - \tau_0) = 1$ or 0 for some t
 - b. This can happen in four ways: 1×1 ; 1×0 ; 0×1 ; 0×0 .
2. Whereas when the signals become identical at $\tau = \tau_0$, we still have

- a. $V(t - \tau)V(t - \tau_0) = 1$ or 0 for some t
- b. But now this can only happen in two ways: 1 x 1; 0 x 0

Thereby maximising those occasions of pulses which overlap, which also maximises the cross-correlation function. Figure 8.10 shows the cross-correlation function of the two signals shown in figure 8.9. The strong peak figure 8.10 is at a value of 600 units, which was artificially inserted into the data, generated by a computer program. Appendix C lists the cross-correlation program and also the program to generate the dummy test data, along with a full explanation of the logic.

From a plot of cross-correlation function against delay, it is quite easy to calculate the average velocity, v_m of the particles that have been recorded. The peak of cross-correlation will occur at some delay, τ_m if the distance between the light curtains is l , then

$$v_m = \frac{l}{\tau_m}$$

Equation 8.8

The data shown in figure 8.9 is artificial - there is a constant delay between the two signals. An erosive stream of real particles will possess, in general, a distribution of velocities, and this will have two effects on the cross-correlation function:

1. The width of the peak delay will be widened.
2. The magnitude of the peak will be reduced because there will be fewer particles travelling with that corresponding velocity.

If there were several sets of particles, each set travelling at a different velocity, then there would be the same number of peaks in the cross-correlation plot - furthermore it can be shown that a continuous distribution of velocities will be reflected in the plot of cross-correlation. It is this last feature of the method which makes it particularly attractive for erosion experiments, where a distribution of velocities may give rise to ambiguous results in the test. Appendix D lists some of the useful properties of cross-correlation.

Velocity Measurement: Rapid Assessment

Cross-correlation is a statistical procedure and suffers from one major disadvantage, it is rather slow. Even with a computer directly coupled to the digital recorder the velocity calculation takes a minimum of twenty minutes - the calculation involves the equivalent of 2.1 million multiplications for two channels of 2000 numbers each. The average time of experiments can be less than twenty minutes, and, in any case, it is very desirable to be able to monitor the average velocity continuously while one is setting the driving gas pressure. For these reasons the circuit shown in figure 8.11 was constructed; it samples the time of flight of individual particles through the optical sensor and displays the time between successive pulses. The circuit starts counting 10 MHz clock pulses when a particle arrives at the first light curtain, and stops counting when a particle arrives at the second light curtain. Clearly this method will indicate the particle velocity if, and only if, there is a low probability of there being two or more particles within the optical sensor at a given time - the method will be successful only in the limit of sufficiently low flux.

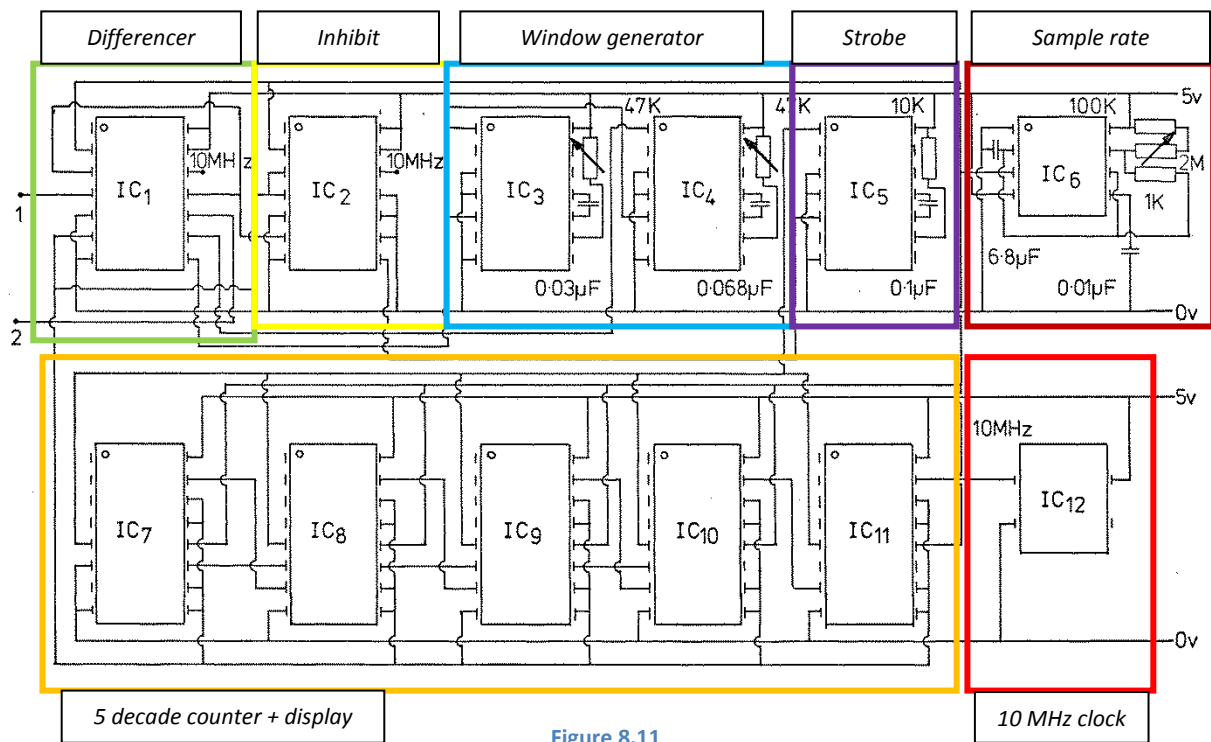


Figure 8.11

Circuit diagram of the sampling timer used to provide a quick assessment of velocity of the erosive stream. The overlay shows the dissemination of pulses within the circuit.

All ICs are TTL types:

- IC_{1,2}: 7470
- IC_{3,4,5}: 74121
- IC₆: 555
- IC₇₋₁₁: TIL 307
- IC₁₂: 10 MHz crystal controlled TTL oscillator.

In figure 8.11 the reader may observe that the lower section of the circuit, comprising IC₇ to IC₁₂, is very similar to the display and clock oscillator section of figure 3.9. For a full description of the operation of this section the reader is referred to Chapter 3; briefly however, this section acts as follows: IC₇ to IC₁₁ together comprise a five-decade counter and display unit that counts the 10 MHz clock pulses from IC₁₂ while it is enabled. There are three control lines to this section, namely: a clear line, to reset the counters and displays; a count enable line, which allows counting to proceed; and a latch strobe, which transfers the counted time value from the counters into the display.

The upper section of figure 8.11 controls the counter lines. IC₆ is a slow running oscillator, of variable frequency from about 5.0 to 0.03 Hz, which controls the sampling rate of the timer by clearing and resetting all the other ICs, apart from IC₁₂.

IC₁ accepts the outputs from the squarer circuits - it is an AND gated J-K positive-edge-triggered flip-flop. Its action is quite simple: its output state changes when its J-input receives a positive-going voltage edge, and this output will only revert to its original state when the K-input receives a positive-edge. The J-input is driven by the squarer corresponding to the first light curtain, while the K-input is driven by the second squarer. IC₅ transfers (strokes) the data from the counters into the display after counting has been completed.

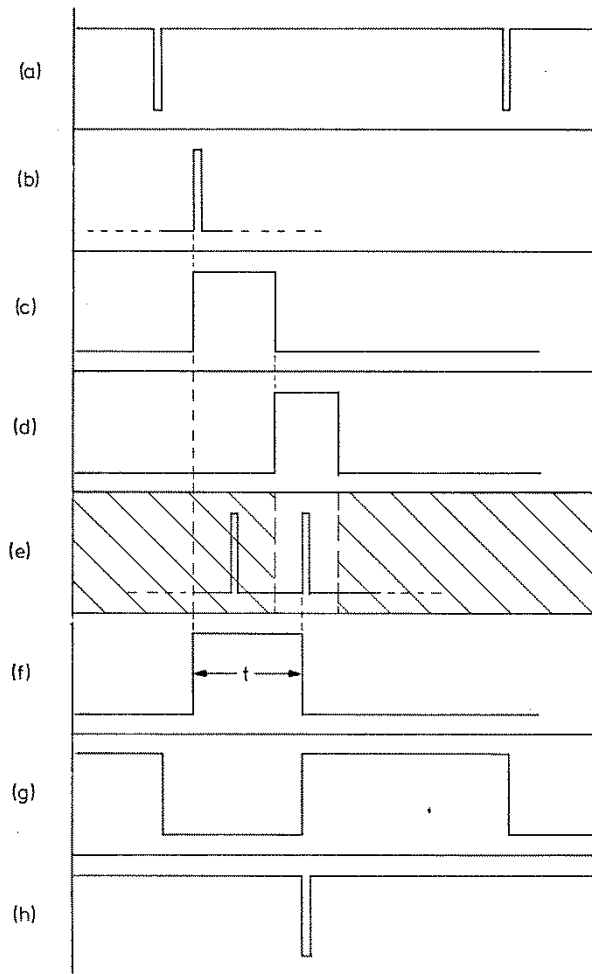


Figure 8.12

Schematic diagram showing the chronological sequence of pulses within the sampling timer shown in Figure 8.11.

- a) Clear pulses produced by $1C_6$.
- b) Input from 1st channel photo-multiplier squarer to J-input of IC_1 . This pulse starts the counter (see point 6 below).
- c) Monostable action of $1C_3$ producing a variable delay.
- d) Monostable action of IC_4 producing a variable delay.
- e) IC_3 and IC_4 acting together generate a window for IC_1 K-input. The first pulse to arrive during this window stops the timer. Further action is inhibited by IC_2 .
- f) Pulse of length t is counted by counter.
- g) IC_2 inhibiting action. TTL = 1 level indicates inhibited action.
- h) IC_5 triggers at the resumption of the inhibited period to transfer (strobe) the count into the displays.

Once IC_1 has operated then IC_2 inhibits any further flip-flop action in IC_1 . IC_3 and IC_4 , together inhibit IC_1 reacting indiscriminately to a pulse at its K-input (2nd light curtain), leaving only a *window* in time for which the input is active. IC_3 introduces a delay of 50 to 1500 μ s after the arrival of a pulse at the J-input (1st light curtain), then IC_4 opens the window for a period of 100 to 3000 μ s during which time the K-input is active. If a pulse arrives at the K-input during this period, then the flip-flop action

can proceed and the display will indicate the duration of this action. If, however, no pulse arrives within this window period then IC₁ will remain latched-up, but IC₂ will still be un-activated, which in turn will stop IC₅ from acting and the display will remain blank until the cycle is cleared and reset.

IC₁ enables the counters for the period between the arrival of a pulse at the J-input and a later pulse at the K-input, provided it arrives between certain time limits. The intention of the time *window* is to discriminate against pulses that may arrive at the K-input producing an erroneous result, which easily could be the case for the random arrival of pulses. In short, the device can *tune-in* to the range of times of flight which are most likely to be correct.

Figure 8.12 shows the chronological sequence of pulses within this circuit.

8.6 Safety Considerations

The equipment described in this chapter generates a considerable amount of heat, under certain circumstances over 10 KW, all of which is derived from electrical energy and disposed of as heat. Single phase alternating current was used to power the barrel heaters and single phase mains was used for the gas pre-heater stage. There were no hot sections of the apparatus left either exposed or un-cooled, which might injure the operator and no metal cases were left unearthed. Considerable care was taken in the construction of the barrel and pre-heater stage to allow for differential thermal expansions that might otherwise cause catastrophic cracking of the ceramic tubes at elevated test temperatures.

The hot erodent can be ducted into a water trap and drawn through it by a powerful vacuum cleaner, thereby rendering the gas/grit mixture harmless. The thermal capacity of the water and trap was made so large that no harmful temperature rise can occur in it. The trap vents the cooled propellant gas into the atmosphere. Those propellants that are most likely to be used include nitrogen and argon. Both of these are harmless gases although they are both asphyxiants when inhaled at high concentrations.

The safety features included in the specimen chamber have been described in Chapter Three.

8.7 Performance of the Erosion Rig

The apparatus which has been described in this Chapter has not yet been fully tested. There have been several problems encountered with sealing the acceleration barrel - most of these have now been overcome.

Chapter 9 Conclusion and Discussion

9.1 Major Themes of This Work

There have been several directions of study in the work described here, the major themes include:

1. To discover under what conditions target melting becomes important.
2. To observe and predict the erosive behaviour of random ensembles of particles.
3. To observe the mechanism of material removal when a single particle strikes a target at normal incidence.

9.2 Importance of Target Melting

Some of the experiments described in this work have shown that material can be removed from a target surface by melting. Copper, mild steel and Nimonic 105T alloy have all been found to commence measurable erosion at 0.6 to 0.8 of their homologous temperature; it is not possible to say with the same degree of certainty, however, bismuth also appears to conform to this behaviour. It was not possible to heat titanium targets to the temperature where they started to commence losing mass, but titanium did not depart from the behaviour of the other metals over the range of homologous temperatures for which it was tested.

The sudden increase of erosion at elevated temperature (about 1100 K) for copper has been directly attributed to melting of the target. The mechanism of material removal in the case of Nimonic alloy appears to be similar to that of copper, however, it is not possible to state with the same certainty that target melting has occurred for Nimonic alloy.

At elevated temperatures (above 900 K) material appears to be lost from the surface of mild steel targets by the detachment of a lip of material from the edge of the crater. This mechanism has been identified elsewhere for single impacts on mild steel, but only for projectiles travelling very much faster than those used in the experiments described here.

The erosion behaviour of Bismuth cannot be classified as either melting or non-melting because it is also very brittle.

Titanium has very high ductility especially at elevated temperatures (above 1100 K). No loss of material was found as a result of impacts on this metal over the entire range of test temperatures (150 to 1200 K).

Nimonic 105T has hardness roughly equal to that of the impacting steel spheres used in experiments. At low test temperatures (less than 300 K) Nimonic targets were found to increase in mass as a result of impact. X-ray analysis has shown this to be due to a thin layer of iron (presumably steel) found residing inside the crater. The steel sphere is abraded during the impact and a layer of steel is left behind adhering to the target, which increases the mass of the target. The effects of

projectile abrasion disappear between 300 to 500 K and give way at higher temperatures to the removal of mass as a result of impact.

9.3 Statistics of Impact

The statistics of erosion have been neglected by authors active in the field of erosion. This work has approached the problem of erosion by an ensemble of particles from two directions:

1. How does the *average shape* of a collection of particles affect their erosive properties? It has been shown that it is possible to use an *index of shape* to predict approximately how the particles will rotate during impact, however, the prediction of how different shaped grits will behave as a bulk erosive agent remains untested.
2. The problem of erosion has been considered as a statistical queuing process through the concept of the *impact zone*. This approach is very responsive to an empirical/deductive *mass-loss* equation. The mass-loss equation appears to be capable of coping with the problems of targets which work harden or targets which melt due to a high flux of erosive particles. This latter equation also sheds new light on the problem of incubation times in erosion. This theory is untested at present.

9.4 Normal Impact

In recent years there has been considerable debate concerning the erosion of metals at normal impingement. The results of experiments described in this work show conclusively that material removal can occur at a normal angle of impingement. Moreover, the removal of material is found to occur when single, spherical particles strike a target without disintegrating and, of course, without any cutting. Material removal appears to proceed by the rapid extrusion of a thin layer of target material under the impacting ball. High-speed photography has shown extrusion occurring on mild steel targets but not on copper. The extrusion appears to have some similarity to the mechanism for the loss of material when a single sphere strikes a brittle target.

The state of the material in the extruded layer is unknown, it may be molten as a result of the rapid work done on it. It has not been possible to verify that melting has occurred. The details of the way in which material is extruded remain unknown.

9.5 Discussion

Erosion by target melting has been shown to occur in single impacts. A target surface in a molten or nearly-molten state is much more liable to be attacked chemically. The combined effect of erosion and corrosion has not been studied here, but it is well understood that the rate of material removal by erosion-corrosion is generally much higher than by either pure erosion or pure corrosion. If erosion by melting can be summarised by a mathematical formula then the problem becomes easier to handle. It is my opinion that the arguments presented here, especially the statistical analysis in section 2.3, go some way towards reaching this goal. This latter analysis is entirely novel and appears to be capable of showing the critical conditions for which target melting can commence.

The study of erosion is not aimed primarily at producing new materials; rather more it is aimed at predicting how long a component can withstand an erosive environment. If we can predict what happens to the rate of erosion when these conditions are altered then we are in a position to discuss the economics of running an eroding system. Unfortunately, very few of the mechanisms for erosion have yet been put into mathematical forms. Until the time arrives when it becomes possible to predict the rate of erosion for different mechanisms, it seems unlikely that we will be able to deduce the dominant mechanism of erosion. I have not answered the question, "When does erosion by target melting become the dominant mechanism?" This is certainly one of the major questions in the study of erosion at the present time, and one which should be answered.

The target-melting and ploughing mechanisms of erosion place more emphasis on the plastic response of the target to impact than does Finnie's mechanism of erosion by cutting. The target-melting theory relies on target plasticity because it assumes that every impact produces heat below the target surface; a ploughing particle can remove material only as a result of the state of plastic strain within the target. Finnie only considers the target to be a perfectly plastic material, he does not consider the distribution of plastic strain around an impact. Not all impacts can be of the type envisaged by Finnie; in fact, the ploughing type of impact is the worst case of a cutting impact but material loss still occurs. Perhaps the state of strain and stress in a target surface is of paramount importance in governing how material is lost from a surface and a greater effort should be directed at determining this influence.

Appendix A

Correct adjustment of the velocity measuring circuit (Single impact)

Figure 3.7 and section 3.3 of Chapter 3 deal with the operation of the velocity measuring device and its ancillary electrical circuits. In the head amplifier stage there are two potentiometers in each channel; they must both be adjusted for correct operation of the circuit.

I will discuss the adjustment of one channel only as this is all that is necessary, both channels being identical in operation.

1. The correct DC conditions should first be set-up.
2. Ensure that the -9 V negative D.C. bias battery is not discharged. It should be replaced every four weeks in operation and immediately prior to use after any spell of inactivity greater than four weeks.
3. Adjust the $1\text{ M}\Omega$ preset resistor until the collector voltage of the BFX37 transistor registers about -1.5 V.
4. The circuit must now be adjusted for dynamic operation. The circuit shown in Figure A.1 artificially generates a known period of flight of a projectile to simulate its passage through the sensing region. Connect points X_1 , X_2 in Figure A.1 to points X_1 , X_2 in Figure 3.9 to perform the test.
5. When transistor BSX28 turns on, the LED that is now connected to it will be robbed of current to an extent controlled by the $47\ \Omega$ variable resistor in the emitter circuit of BSX28. The LED will be dimmed, simulating the passage of the projectile. Depressing switch PS2/3 allows visual verification of the LED's dimmed light level.
6. Once both LEDs are adjusted to a suitable dimmed light level select any of the four positions of switch SW1. With this switch in position, depressing switch PS1 will make IC₄ insert a time delay (4 ms, 400 μs , 160 μs , 80 μs) between dimming the LEDs. This timed period can be checked externally on an electronic timer, the same period should be displayed on this timer as on the velocity timer unit. This forms the basis of the test.
7. Adjust the decoupling preset resistor in the base circuit of the phototransistor until both displays are equal or very nearly so.
8. IC₁ and IC₂ simulate appropriate occlusion times of the LEDs (500 μs , 100 μs , 20 μs , 5 μs) to correspond to the chosen timed period. A suitable turn-on and turn-off time of the LED is also set by the base circuit of BSX28.
9. It should be possible to adjust both variable resistors in the head amplifier until the counter just ceases to work at each position of SW₁.

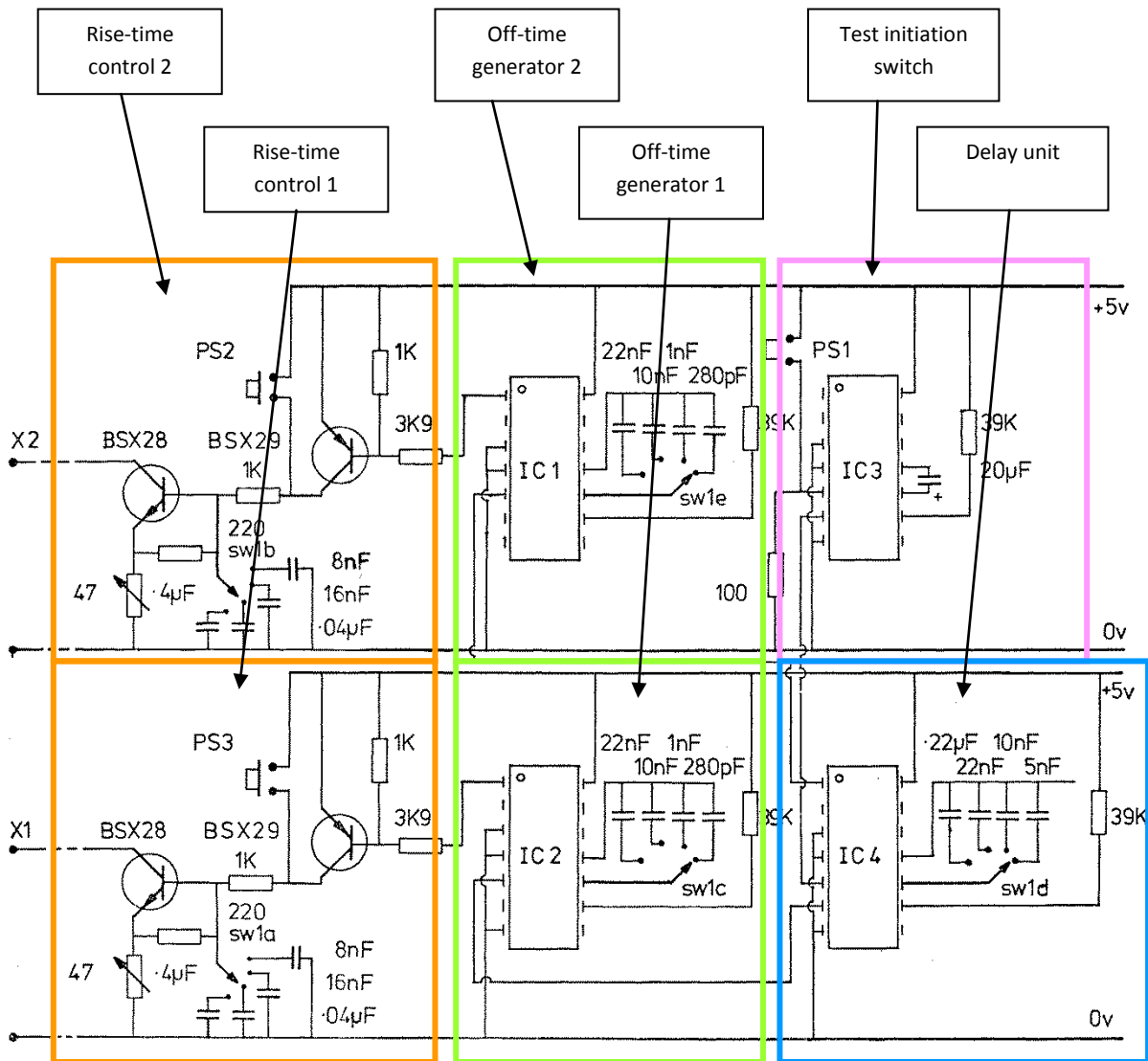


Figure A. 1

Circuit diagram of the testing circuit for the velocity timer used in single impact experiments. The overlay shows the progression of pulses within the circuit.

Signal flow:

1. Test Initiation Switch generates a master pulse when PS1 is pressed.
2. The master pulse goes to Delay Unit which generates two pulses with a known, adjustable delay time between them.
3. The un-delayed pulses go to Off-time Generator 1.
4. The delayed pulses go to Off-time Generator 2.
5. The outputs from Off-time Generators go to identical Rise-time Control circuits.
6. The output signals from X1 and X2 go to the LEDs in the head amplifier of the velocity measuring circuit.

Appendix B

Curve fitting to impact craters

The impact of a hard sphere on a ductile surface generates an indentation or crater on the surface. Craters produced in this manner have shapes which can be represented to a good approximation by the following expression:

$$\frac{dx^2}{a_o^2(z+d)} + \frac{y^2}{r^2 - (z+d-r)^2} = 1$$

Equation B1

The derivation of this expression is discussed in Chapters 2 and 4. Equation B1 contains two independent parameters a_o , d . The radius of the impacting sphere r is given. The expression is fitted to the data points (x_i, y_i, z_i) $i = 1, 2, \dots, n$ by choosing the independent parameters to minimize the error E .

$$E = \sum_{i=1}^n \{(x_i - a_i \cos \theta_i)^2 + (y_i - b_i \sin \theta_i)^2\}$$

Equation B2

$$a_i^2 = \frac{a_o^2}{d} (d + z_i)$$

$$b_i^2 = r^2 - (z_i + d - r)^2$$

$$\theta_i = \tan^{-1} \left(\frac{y_i}{x_i} \right)$$

The error is calculated in the x-y plane only. A large weighting value is applied to the error if a trial d is less than the current contour depth z_i . Although, for small z_i , there is a similar accuracy of measurement of (x_i, y_i) and (z_i) , the accuracy of measurement of z_i improves at larger z_i . It is important that these points should be included preferentially in the curve fitting.

The data is produced relative to an arbitrary coordinate system. The crater is not necessarily aligned with its length along the x-axis or with the origin above the deepest point. This introduces a further three independent parameters to the calculation.

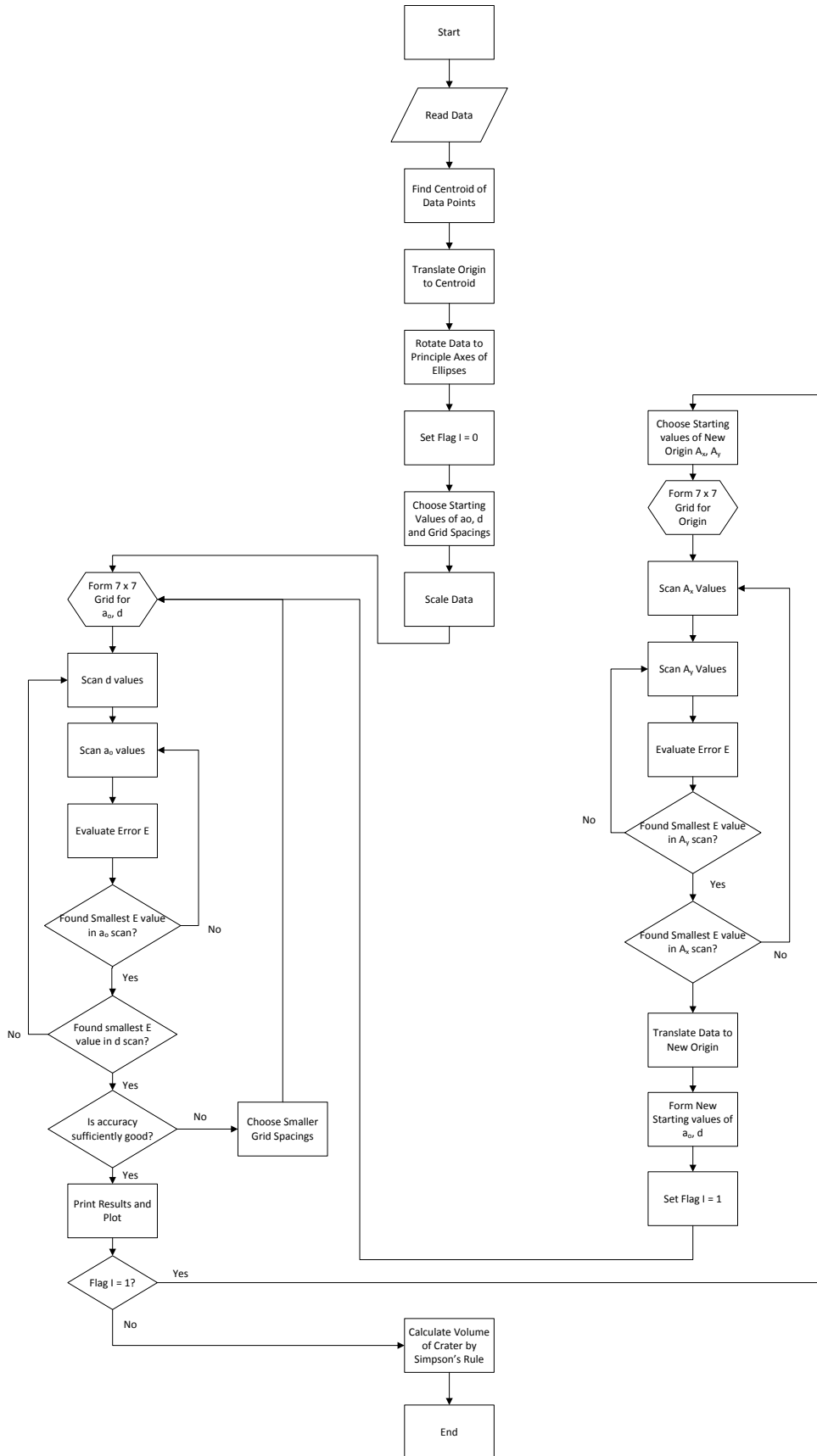
Since there are five independent parameters which must be determined and because equation B1 is non-linear it is not possible to write a rapidly converging algorithm to optimise a_o and d simultaneously. The method described here starts by choosing the centroid of (x_i, y_i) as the origin. The data points are rotated by an angle which forces the x-axis to be the major axis of the crater ellipses. The position of the origin is altered at a later stage to improve the fit.

The data points are scanned and extreme values of a_o and d are deduced. These extreme values are used as the limits of a grid of 7 x 7 points and at each one the error is calculated. The minimum value of E is determined and the square of points enclosing this point is used to form a new 7 x 7 grid. The process is repeated, without re-calculating E at any of the original grid points (to minimise computing time), until the differences between successive best estimates of both a_o and d are less than a preset value. At this juncture a similar procedure is carried out on the choice of origin until a better fit is obtained. The last limits of a_o and d are expanded and then a final gridding process is performed.

Once the best values of a_o and d have been found the original data points are plotted. The ellipses which correspond to the contour fringes of the data points are drawn allowing a visual check to be made of the goodness of the fit. Finally the volume enclosed by the plane $z = 0$ and the surface (B1) is found using Simpson's rule. The routine also generates a correlation coefficient defined as

$$\text{Correlation coefficient} = 1 - \frac{\sqrt{\frac{E_{min}}{n}}}{a_o}$$

Correlation coefficients of 0.97 have been commonly generated using data obtained from moiré fringes.



Flow diagram for algorithm

Computer Listing

Hewlett-Packard Language (HPL).

```

0: dsp "Crater
Volume Function
Fit";wait 2000
ide:iflt 3;dim
C#[3]
1: dsp "Assume:0
ata equal space
Contours";wait
2000
2: "Round":ent
"Input form
MAG/KEY?";C#
3: if C#="MAG";
sto "Mag"
4: if C#="KEY";
jmp 2
5: jmp -3
6: 0+A+B;dim
Z#[10]
7: enp "Head
Code?";Z#
8: enp "No. Cont
ours?";A
9: enp "No. Data
points in first
contour?";B;
spc
10: diw A[A],
X[B,A],Y[B,A],
B[7,5];1+H+V+R;
B+A[1]
11: dsp "No.
Data points
per Contour?";
wait 2000
12: for I=2 to A
13: dsp "No.
points in Conto
ur";I;wait 500
14: enp A[I]
15: next I
16: for J=1 to A
17: prt "Cont=",
J
18: for I=1 to
A[J]
19: prt "No=",I
20: enp "X=",
X[I,J]
21: enp "Y=",
Y[I,J]
22: next I;spc
23: next J;spc
24: ent "Alterat
ions to Data?-
YES/NO";C#
25: if C#="NO";
jmp 9
26: if C#="YES";
jmp 2
27: jmp -3
28: enp "Contour
no.";J
29: enp "Data
point?";I
30: enp "X=",
X[I,J]
31: enp "Y=",
Y[I,J];spc
32: ent "Further
alterations-
press 1 cont";I
33: if I=1;jmp -
5
34: "Determine
Rotation Angle"
:
35: prt "Major
Axis points"
36: enp "X-coord
inate,1st point
?";B[1,5]
37: enp "Y-coord
inate,1st point
?";B[2,5]
38: enp "X-coord
inate,2nd point
?";B[3,5]
39: enp "Y-coord
inate,2nd point
?";B[4,5]
40: ent "Any
alterations?-
Press 1 cont";I
41: if I=1;jmp -
6
42: B[2,5]-B[4,
5]+T;B[1,5]-
B[3,5]+S
43: if S=0;0+B[7
,5];jmp 3
44: if T=0;90+B[
7,5];jmp 2
45: atn(T/S)+B[7
,5]+B[6,5]
46: ent "Ball
Diameter in
mm?";R/R/2+R
47: prt "Ball
Diam=",2*R

```

```

48: spc ;prt
   "Scaline Factor
   s";spc
49: enp "Horizon
   tal Factor?-",H
50: enp "Vertica
   l Factor?-",V
51: ent "Any
   alterations?
   Press 1 cont",I
52: if I=1;jmp -
   6
53: spc ;eto
   "Rec"
54: "Mac":enp
   "Track no. of
   Data files?",I
55: enp "File
   no. of 1st Data
   file?",J
56: 0+A+B;dim
   Z#[10]
57: trk I;ldf J,
   A,B,Z#
58: dim A[A],
   X[B,A],Y[B,A],
   B[7,5];1+H+V+R
59: ldf J+1,A[*
   ],X[*],Y[*],B[*
   ],H,V,R
60: prt Z#;spc
61: "Rec":ent
   "Record Data?
   YES/NO",C#
62: if C#="NO";
   jmp 7
63: if C#="YES";
   jmp 2
64: jmp -3
65: enp "Track
   no.",I
66: enp "1st
   File no.?",J
67: trk I;rcf J,
   A,B,Z#
68: rcf J+1,A[*
   ],X[*],Y[*],B[*
   ],H,V,R
69: "Determine
   Ax,Ay by Centro
   id":0+B[7,3]+B[
   7,4]
70: for J=1 to A
71: for I=1 to
   A[J]
72: B[7,3]+X[I,
   J]+B[7,3]
73: B[7,4]+Y[I,
   J]+B[7,4]
74: next I
75: next J
76: 0+T
77: for J=1 to A
78: T+A[J]+T
79: next J
80: B[7,3]/T+B[7
   ,3];B[7,4]/T+B[
   7,4];T+B[6,5]
81: for J=1 to A
82: for I=1 to
   A[J]
83: X[I,J]-B[7,
   3]+X[I,J]
84: Y[I,J]-B[7,
   4]+Y[I,J]
85: next I
86: next J
87: "Rotate Data
   to Principal
   Axes":
88: B[7,5]+C
89: for J=1 to A
90: for I=1 to
   A[J]
91: X[I,J]cos(C)
   +Y[I,J]sin(C)+X
92: -X[I,J]sin(C
   )+Y[I,J]cos(C)+
   Y
93: X+X[I,J];
   Y+Y[I,J]
94: next I
95: next J
96: "Determine
   starts for d,
   Ao":
97: for J=1 to 2
98: 0+B[J,2]
99: for I=1 to
   A[J]
100: if X[I,J]+2
   +Y[I,J]+2>B[J,
   2];X[I,J]+2+
   Y[I,J]+2>B[J,2]
101: next I
102: rB[J,2]+B[J
   ,2]
103: next J
104: B[1,2]+0;
   B[2,2]+K
105: .5*0+.5*
   K+B[1,2];1.5*0-
   .5*K+B[2,2]
106: A+.3+B[1,
   1];A+1.5+B[2,1]
107: V/20+B[4,
   1];(B[2,2]-B[1,
   2])/20+B[4,2];
   prt B[4,1]
108: for J=1 to
   2

```

```

109: (B[2,J]-
    B[1,J])/6+B[3,
    J]
110: B[1,J]+3*
    B[3,J]+B[5,J]
111: B[1,J]+B[6,
    J]
112: next J
113: "Scale Data
":
114: for J=1 to
    A
115: for I=1 to
    H[J]
116: X[I,J]=H*X[
    I,J];Y[I,J]=
    H*Y[I,J]
117: next I
118: next J
119: for J=1 to
    4
120: if J=1;V+K;
    jmp 2
121: H+K
122: for I=1 to
    7
123: if I=4;jmp
    3
124: if J=1;if
    I<3;B[I,J]-1+B[
    I,J]
125: B[I,J]*K+B[
    I,J]
126: next I
127: next J
128: cfs 1
129: "Function
    fitting":0+B[5,
    3]+B[5,4]
130: 'F'(B[5,1],
    B[5,2],B[5,3],
    B[5,4])>0;1+0;
    fxd 0
131: "Pass":3+L+
    K
132: for J=0 to
    6
133: for I=0 to
    6
134: if 0=1;jmp
    2
135: if frc(I/
    3)=0;if frc(J/
    3)=0;I+1+I;if
    I>6;6+I;jmp 8
136: dsp 0,J,I,
    K,L,"d,Ro"
137: B[1,1]+J*
    B[3,1]+B[7,1]
138: B[1,2]+I*
    B[3,2]+B[7,2]
139: 'F'(B[7,1],
    B[7,2],B[5,3],
    B[5,4])>E
140: if E<D;E+D;
    I+L;J+K
141: if abs(E-
    0)>D/5;I+1+I
142: if abs(E-
    0)>D;I+1+I
143: next I
144: next J
145: for J=1 to
    2
146: B[5,J]+B[6,
    J]
147: if J=1;K+C
148: if J=2;L+C
149: B[1,J]+C+
    B[3,J]+B[5,J]
150: B[5,J]+B[3,
    J]+B[2,J]
151: B[5,J]-B[3,
    J]+B[1,J]
152: (B[2,J]-
    B[1,J])/6+B[3,
    J]
153: next J
154: for J=1 to
    2
155: if abs(B[5,
    J]-B[6,J])>B[4,
    J];0+1+0;ato
    "Pass"
156: next J
157: flt 3
158: dsp "Best
    fit found"wait
    2000;flt 3
159: prt "d=",
    B[5,1];sec
160: prt "Ro=",
    B[5,2];sec
161: prt "Correl
    ation=",1-(D/
    B[6,5])/B[5,2];
    sec
162: if flt 1=1;
    end "Change
    paper-press
    continue":L
163: scl -1.5*
    B[5,2],1.5*B[5,
    2],-1.5*B[5,2],
    1.5*B[5,2]
164: axc 0,0,.5*
    B[5,2],.5*B[5,
    2]
165: if flt 1=0;
    jmp 7
166: for J=1 to
    A

```

```

167: for I=1 to
  A[J]
168: X[I,J]-B[5,
  3]*X[I,J]
169: Y[I,J]-B[5,
  4]*Y[I,J]
170: next I
171: next J
172: for J=0 to
  A-1
173: -J*V+Z
174: r(R↑2-(Z+
  B[5,1]-R)↑2)+G
175: B[5,2]*r((Z
  +B[5,1])/B[5,
  1])↑F
176: for I=1 to
  A[J+1]
177: plt X[I,J+
  1],Y[I,J+1];
  pen:plt -.3,-
  .3;lbl "X";pen
178: next I
179: for C=0 to
  360 by 2
180: plt F*cos(C
  ),G*sin(C)
181: next C
182: pen:next J
183: "Rechoose
  Ax,Ay":
184: if fl=1=1;
  ato "Val"
185: "Re":1+0
186: B[5,2]*r((B
  [5,1]-(A-1)*V)/
  B[5,1])↑G
187: r(R↑2-((A-
  1)*V+B[5,1]-
  R)↑2)+F
188: -.1*G+B[1,
  3];.1*G+B[2,3]
189: (B[2,3]-
  B[1,3])/6+B[3,
  3]
190: -.15*F+B[1,
  4];.15*F+B[2,4]
191: (B[2,4]-
  B[1,4])/6+B[3,
  4]
192: .03G+B[4,
  3];.03*F+B[4,4]
193: 0+B[6,3]+B[
  6,4]+B[5,3]+B[5
  ,4]
194: fxd 0
195: "Pas":3+L+K
196: for J=0 to
  6
197: for I=0 to
  6
198: if 0=1;jmp
  2
199: if frc(I/
  3)=0;if frc(J/
  3)=0;I+1+I;if
  I>6;jmp 8
200: dsp 0,J,I,
  K,L,"Ax,Ay"
201: B[1,3]+J*
  B[3,3]+B[7,3]
202: B[1,4]+I*
  B[3,4]+B[7,4]
203: 'F'(B[5,1],
  B[5,2],B[7,3],
  B[7,4])↑E
204: if E<D;E+D;
  I+L;J+K
205: if abs(E-
  D)>D/5;I+1+I
206: if abs(E-
  D)>D;I+1+I
207: next I
208: next J
209: for J=3 to
  4
210: B[5,J]+B[6,
  J]
211: if J=3;K+C
212: if J=4;L+C
213: B[1,J]+C*
  B[3,J]+B[5,J]
214: B[5,J]+B[3,
  J]+B[2,J]
215: B[5,J]-B[3,
  J]+B[1,J]
216: (B[2,J]-
  B[1,J])/6+B[3,
  J]
217: next J
218: for J=3 to
  4
219: if abs(B[5,
  J]-B[6,J])>B[4,
  J];0+1+0;ato
  "Pas"
220: next J
221: .95*B[5,
  1]+B[1,1];1.05*
  B[5,1]+B[2,1]
222: (B[2,1]-
  B[1,1])/6+B[3,
  1]
223: .95*B[5,
  2]+B[1,2];1.05*
  B[5,2]+B[2,2]
224: (B[2,2]-
  B[1,2])/6+B[3,
  2]
225: sfa 1;fxd
  0;1+0;ato "Pass
  "

```

```

226: "Volume
      Calculation By
      Simpson's Rule"
      :
227: "Vol":3*
      B[5,1]-2*R+E
228: 4*R*B[5,1]-
      3*B[5,1]↑2+F
229: 2*R*B[5,
      1]↑2-B[5,1]↑3+G
      ;0+H;-B[5,1]/
      100+K
230: for I=2 to
      100 by 2
231: for J=-2
      to 0
232: (I+J)*K+r3
233: if I=100;
      if J=0;0+r2;
      jmp 2
234: r(-r3↑3-E*
      r3↑2+r3*F+G)+r(
      J+2)
235: next J
236: H-K(r0+4*
      r1+r2)/3+H
237: next I
238: π#H*B[5,2]/
      rB[5,1]↑H
239: prt "Volume
      =",H
240: pen;plt -
      1.5*B[5,2],1.4*
      B[5,2];lbl "Cod
      e ";Z#;pen;
      fxd 4
241: plt -1.5*
      B[5,2],1.3*B[5,
      2];lbl "Depth="
      ;B[5,1];pen
242: plt -1.5*
      B[5,2],1.2*B[5,
      2];lbl "Lenath="
      ",2*B[5,2];pen
243: plt -1.5*
      B[5,2],1.1*B[5,
      2];lbl "Volume="
      ";H;pen
244: plt -1.5*
      B[5,2],B[5,2];
      lbl "Ball Diam="
      ",2*R
245: stop
246: "F":0+S
247: for Q=1 to
      R
248: -(Q-1)*V+Z
249: if Z+p1<.00
      00;0+G+H;jmp 3
250: r(R↑2-(Z+
      p1-R)↑2)+G
251: p2*r((p1+
      Z)/p1)+H
252: for M=1 to
      R[0]
253: X[M,0]-p3+P
      ;Y[M,0]-p4+T
254: if G=0;S+
      P↑2+T↑2+(5000*
      (Z+p1)↑2+S;
      jmp 8
255: if P#0;if
      T#0;jmp 5
256: if P=0;if
      T>0;90+F;jmp 6
257: if P=0;if
      T<0;270+F;jmp 5
258: if T=0;if
      P>0;0+F;jmp 4
259: if T=0;if
      P<0;180+F;jmp 3
260: atn(H*T/(G*
      P))+F
261: if P<0;180+
      F+F
262: S+(H*cos(F)
      -P)↑2+(G*s n(F)
      -T)↑2+S
263: next M
264: next Q
265: ret S

```

Appendix C

Computer aided cross-correlation

In order to be able to perform cross-correlation of binary signals arising from individual particles travelling through two light curtains, certain conditions must prevail:

1. The duration of data storage, T , should be large enough to be statistically meaningful - there must be at least thirty pulses in each channel.
2. The majority of particles must pass through both light curtains during the storage of data, otherwise there will be a very small cross-correlation peak.
3. The data sampling period must be smaller than the average signal pulse duration, otherwise there will be a good chance of failing to sample a pulse.

This appendix lists two computer programs in HP-L (Hewlett-Packard Language):

1. One accepts data from paper tape or magnetic tape cassette, and performs the cross-correlation upon it.
2. The other generates dummy test data for the former.

In the latter program the choice of time delay, between the signals of the two channels, is made by the operator from the computer keyboard.

The program performing cross-correlation (C-C) is based on a novel storage of data. The digital recorder has a 4096 byte memory split equally between both channels; each channel represents data storage of 2048 numbers stored to 8-bit accuracy (better than 0.4%). The photo-multiplier tubes' squarer circuits output TTL binary signals to the recorder and the computer re-converts the recorder's signals back into true binary form. It is possible to store each binary number as if it were a 9-figure decimal number; this would require a large memory store (although well within the capability of most computers) but this is an unnecessary complication. If this method of data storage were to be used, however, then the number of multiplication operations required to evaluate the cross-correlation can be estimated.

Time delay, τ (data sample steps)	Number of multiplications
0	2048
1	2047
2	2046
i	$2048 - i$
2047	1
2048	0

Therefore, the total number of multiplications involved in calculating the C-C function is given by

$$\text{Number of multiplications} = \sum_{i=0}^{2048} (2048 - i) = 2.1 \times 10^6$$

For the computer used, this is a task that would require several hours to complete - this was thought to be an unacceptable period.

An economy of storage and a significant reduction in the execution time of the program results from storing the data in Binary One Block (B1B) lengths and Binary Zero Block (B0B) lengths. A B1B is the number of consecutive data points of binary value equal to one, it represents a figure corresponding to the signal pulse length (average of B1Bs is T_p); a B0B is the number of consecutive data points of binary value equal to zero, it represents a figure corresponding to the time between pulses (average of B0Bs is α , see Appendix D).

Performing C-C now becomes a process of forming two lists of numbers, one for each channel, with the time coordinates of the B1Bs. One list must be altered for every new time-shift, τ ; next, it is only necessary to check the lists for overlapping regions, and calculate the extent of overlap. A result from the study of Venn diagrams is most useful in this last operation; if area A overlaps with area B then

$$A \cap B = A + B - A \cup B$$

The intersection of A and B is the required overlap; the sum of A and B, and the union of A and B can both be calculated easily.

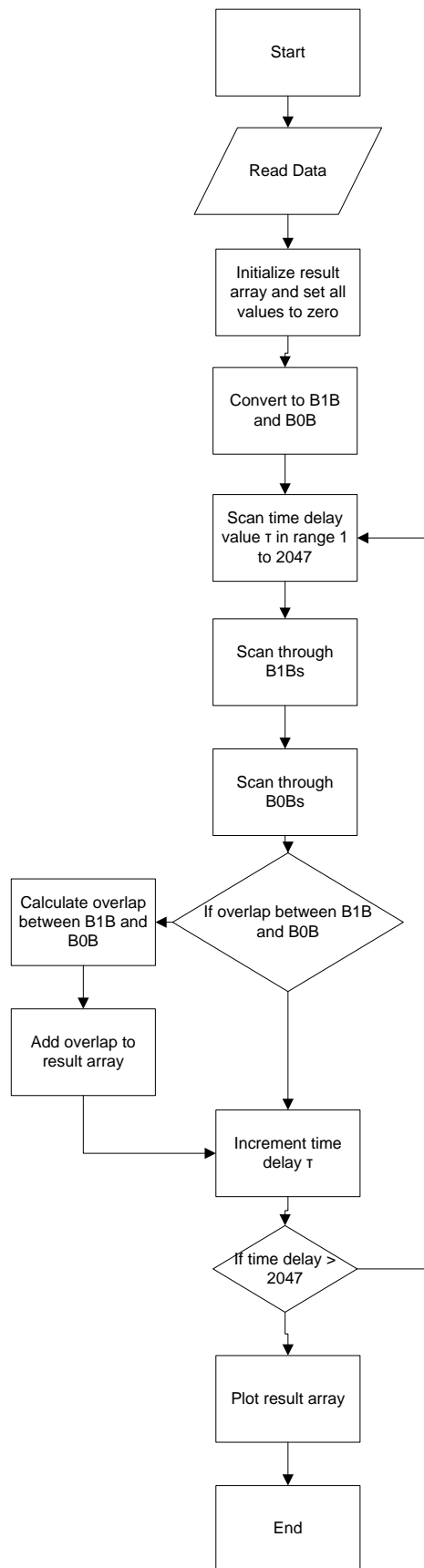
This procedure must be performed for each time-delay. In the limit of $\alpha, T_p \rightarrow 1$ then the method of Pulse Length Storage (PLS) will become equivalent to the standard multiplicative (SM) method of performing C-C. Since $\alpha, T_p \rightarrow 1$ represents a condition for which C-C becomes inappropriate, it follows that in all cases the PLS method will be faster. For the test data shown in Figure 8.9 the method of PLS took about fifteen minutes to execute, whereas the SM method would have taken about 3 to 4 hours. A SM program was written and tested, but tested only for time delays up to 700 units out of 2048, for which execution time was of the order 1.5 hours.

The faster PLS method, of which both the program and flow diagram are listed in this appendix, in addition to plotting C-C against time delay, also plots C-C against velocity. Velocity is obtained from T by the following expression:

$$\text{Velocity} = \frac{\iota}{\tau T_s}$$

where ι = distance between light curtains, T_s = sampling period.

PLS method of C-C: Flow diagram



PLS method of C-C: computer program (HP-L)

```

0: fxd 0
1: dsp "Cross
  Correlation+Vel
  ocity";wait
  2000
2: dim Y#[64],
  Y[16],D#[4096],
  E#[4096],A#[3],
  C#[4094]
3: ent "Input
  form Mag/Pap
  Tape?-MAG/PAP",
  A#
4: if A#="MAG";
  ato "MAG"
5: if A#="PAP";
  ato "PAP"
6: jmp -3
7: "Read in pape
  r tape & conver
  t to Binary":
8: "PAP":0+C+D;
  wtc 3,32:red 3,
  0
9: for I=1 to
  256:red 3,Y#
10: for J=1 to
  16;16(I-1)+J+K
11: val(Y#[4J-3,
  4J])→Y[J]
12: if Y[J]<125;
  0→Y[J];jmp 2
13: 1→Y[J]
14: if I<129;
  fti (Y[J])→D#[2
  K-1,2K];jmp 2
15: fti (Y[J])→E
  #[2K-4097,2K-
  4096]
16: next J;next
  I;wtc 3,34
17: "Count 2*
  no. pulses":itf
  (D#[1,2])→A;0→C
18: for I=2 to
  2048
19: if abs(itf(D
  #[2I-1,2I])
  -A)=1;1+C→C;itf(
  D#[2I-1,2I])→A
20: next I
21: C→M
22: itf(E#[1,
  2])→A;0→C
23: for I=2 to
  2048
24: if abs(itf(E
  #[2I-1,2I])
  -A)=1;1+C→C;itf(
  E#[2I-1,2I])→A
25: next I
26: C→N
27: "Set startin
  g Binary Parity
  =1":
28: if itf(D#[1,
  2])=0;M+1→M
29: if itf(E#[1,
  2])=0;N+1→N
30: if itf(D#[40
  95,4096])=1;M+
  1→M
31: if itf(E#[40
  95,4096])=1;N+
  1→N
32: dim Z#[64],
  A[M],B[N]
33: if itf(D#[1,
  2])=0;0→A[1];
  2→A;jmp 2
34: 1→A
35: if itf(E#[1,
  2])=0;0→B[1];
  2→B;jmp 2
36: 1→B
37: itf(D#[1,
  2])→C;itf(E#[1,
  2])→D
38: "Store data
  in A[*],B[*]":
39: for I=2 to
  2048
40: if abs(itf(D
  #[2I-1,2I])
  -C)=1;I-1→A[A];
  A+1→A;itf(D#[2I
  -1,2I])→C
41: next I
42: for J=2 to
  2048
43: if abs(itf(E
  #[2J-1,2J])
  -D)=1;J-1→B[B];
  B+1→B;itf(E#[2J
  -1,2J])→D
44: next J
45: if itf(D#[40
  95,4096])=1;
  A[M-1]→A[M]
46: if itf(E#[40
  95,4096])=1;
  B[N-1]→B[N]

```

```

47: dsp "Data
   required";wait
2000
48: for I=1 to
64
49: " "+Z#[I,I]
50: next I
51: enp "Head
   Code";Z#
52: spc
53: spc
54: sto "PASS"
55: "MAG":ent
   "Track no. of
   data file?-",A
56: ent "File
   no. 1st of data
   file?-",B
57: 0+M+N
58: dim Z#[64]
59: trk A;ldf B,
   M,N,Z#
60: dim A[M],
   B[N]
61: ldf B+1,A[*
   ],B[*]
62: prt Z#
63: spc
64: spc
65: "PASS":ent
   "Record data?-
   YES/NO",A#
66: if A#="NO";
   sto "PLOT"
67: if A#="YES";
   jmp 2
68: jmp -3
69: enp "Head
   Code";Z#;if
   fl#13;if Z#[1,
   1]=" ";jmp -4
70: spc
71: enp "Track
   no. of new data
   file?-",A
72: dsp "Caution
   :2 new data
   files wanted";
   stp
73: dsp "1st=100
   0bytes;2nd=6500
   bytes";stp
74: enp "File
   no. of first
   new data file?-",
   B
75: spc
76: ent "Files
   marked?-OK?",A#
77: if A#="OK";
   jmp 2
78: jmp -2
79: trk A;rcf B,
   M,N,Z#
80: rcf B+1,A[*
   ],B[*]
81: "PLOT":ent
   "Plot signals?-
   YES/NO",A#
82: if A#="NO";
   sto "NPLOT"
83: if A#="YES";
   jmp 2
84: jmp -3
85: scl 0,2048,-
   1.2,1.2
86: axe 0,-1.2,
   100,.2
87: if A[I]=0;
   plt 0,0;2+A;
   jmp 2
88: plt 0,1;1+A
89: for I=A to M
90: plt A[I],2*
   frc(I/2);plt
   A[I]+1,2*frc((I
   +1)/2)
91: next I;plt
   2048,0;pen
92: if B[I]=0;
   plt 0,-1.2;2+B;
   jmp 2
93: plt 0,-.2;
   1+B
94: for I=B to M
95: plt B[I],2*
   frc(I/2)-1.2;
   plt B[I]+1,2*
   frc((I+1)/2)-
   1.2
96: next I;plt
   2048,-1.2
97: pen;plt 10,
   1.1;lbl Z#;pen;
   plt 10,-.1
98: lbl "Signal
   Plot.Number of
   pulses: 1st=",
   (M-1)/2,";2nd="
   ,(N-1)/2;pen
99: dsp "Change
   plot paper"
100: stp
101: "NPLOT":
102: "Start Cros
   s correlation
   sequence":

```

```

103: for I=1 to
2047
104: fti (0)+C#[
2I-1,2I]
105: next I
106: (N-1)/2+N
107: 0+P
108: (M-1)/2+M
109: for I=1 to
2047
110: if I>B[2P+
1]P+1+P
111: if P>N:ato
"OVER"
112: 1→T
113: for R=P to
N
114: if R=0:I+C;
jmp 3
115: if I>B[2R];
I+C;jmp 2
116: B[2R]+C
117: for S=T to
M
118: if B[2R]+
1>A[2S+1]+I;
S→T;jmp 3
119: if B[2R+
1]<A[2S]+1+I;
jmp 15
120: if A[2S]+
1<B[2R+1];if
C<A[2S+1]+I;
jmp 4
121: next S
122: jmp 12
123: "WE have
correct R,S":
124: if C>B[2R];
C-1→G;jmp 2
125: B[2R]+C
126: if A[2S]+
1<G;A[2S]+I→E;
jmp 2
127: G→E
128: if A[2S+1]+
I>B[2R+1];A[2S+
1]+I→F;jmp 2
129: B[2R+1]+F
130: "A+B=A+B-
AUB":
131: itf(C#[2I-
1,2I])+W
132: fti (W+A[2S
+1]+B[2R+1]+E-
F-A[2S]-G)+C#[2
I-1,2I]
133: jmp -12
134: next R
135: dsp I
136: next I
137: "OVER":0+P
138: for I=1 to
2047
139: if itf(C#[2
I-1,2I])>P;itf(
C#[2I-1,2I])+P;
I→Z
140: next I;prt
"Peak=";P;prt
"Time=";Z
141: spc
142: enp "plot
Y scale value="
,A
143: enp "Y scal
e tic value=";B
144: spc
145: des
146: scl -250,
2100,-A/10,A
147: axe 0,0,
100,B
148: for I=1 to
2047
149: plt I,itf(C
#[2I-1,2I])
150: next I
151: pen:plt
800,-A/10;csiz
1.5,1.5,1,0;
cplt -.4,0;lbl
"Time Delay";
pen
152: for I=0 to
2000 by 500
153: plt I-50,-
A/20;cplt -1.3,
0;lbl I;pen
154: next I
155: plt -200,A/
4;cplt -.3,0;
csiz 1.5,1.5,1,
90;lbl "C-C
Function";pen
156: csiz 1.5,
1.5,1,0
157: for I=B-B/
8 to A-B/8 by B
158: plt -100,I;
cplt -1.3,0;
lbl I+B/8;pen
159: next I
160: plt 100,A-
B/4;cplt -.5,0;
lbl Z;pen
161: dsp "Labels
"iptyp

```

```

162: 1+M
163: "E":ent
    "Velocity plot,
    YES/NO?-",A#
164: if A#="YES"
    ;if M=1;eto
    "VEL"
165: if A#="YES"
    ;eto "VELY"
166: if A#="NO";
    eto "NVEL"
167: jmp -3
168: "VEL":enp
    "Time sweep?-",
    S
169: prt "Peak
    vel=",.02*2048/
    (2*S)
170: prt "Min
    vel=",.02/S
171: "VELY":enp
    "Minimum plot
    velocity?-",U
172: enp "Maximu
    m plot velocity
    ?-",T
173: enp "Veloci
    ty axis tic
    space?-",V
174: scl 1.15U-
    .15T,1.1T-.1U,-
    A/10,A
175: axe U,0,V,B
176: .02*2048/
    (T*S)+J
177: if frc(J)#0
    ;int(J)+1+J;
    jmp 2
178: int(J)+J
179: for I=J to
    int(.02*2048/
    (U*S))
180: plt .02*
    2048/(I*S),itf(
    C#[2I-1,2I])
181: next I;pen
182: plt .6U+
    .4T,-A/10;csiz
    1.5,1.5,1,0
183: cplt -.4,0;
    lbl "Velocity
    m/s";pen
184: for I=U to
    T by V
185: plt I-.025(
    T-U),-A/20;cplt
    -1.3,0;lbl I;
    pen
186: next I
187: plt 1.1U-
    .1T,A/4;cplt -
    .3,0;csiz 1.5,
    1.5,1,90
188: lbl "C-C
    Function";pen
189: csiz 1.5,
    1.5,1,0
190: for I=B-B/
    8 to A-B/8 by B
    /8
191: plt 1.075U-
    .075T,I;cplt -
    1.3,0;lbl I+B/
    8;pen
192: next I
193: plt .95U+
    .05T,A-B/4;cplt
    -.5,0;lbl 2;
    pen
194: 2+M
195: dsp "Labels
    ";ityp
196: eto "E"
197: "NVEL":end

```

PLS and SM method of C-C: Test data

```

0: dim D#[4096],
   E#[4096],F#[204
   8],G#[2048]
1: fxd 0
2: 0+A
3: "PASS":int(10
  *rnd(1))+8
4: int(100rnd(1)
  )+C
5: if A+B>2048:
  2048-A+B
6: for I=1 to B
7: fti (1)+D#[2(
  I+A)-1,2(I+A)]
8: next I
9: A+B+A
10: if A+C>2048:
  2048-A+C
11: for J=1 to C
12: fti (0)+D#[2
  (J+A)-1,2(J+A)]
13: next J
14: A+C+A
15: if A=2048:
  jmp 2
16: sto "PASS"
17: ent "Desired
  delay,1+2048?"
  ,X
18: for I=1 to
  4096
19: " "+E#[I]
20: next I
21: for I=1 to
  2048
22: D#[2I-1,2I]+
  E#[2(I+X)-1,
  2(I+X)]
23: if I+X=2048:
  X-2048+X
24: next I
25: for I=1 to
  2048
26: if itf(D#[2I
  -1,2I])=1;char(
  49)+F#[I,I];
  jmp 2
27: if itf(D#[2I
  -1,2I])=0;char(
  48)+F#[I,I]
28: if itf(E#[2I
  -1,2I])=0;char(
  48)+G#[I,I];
  jmp 2
29: if itf(E#[2I
  -1,2I])=1;char(
  49)+G#[I,I]
30: next I
31: dsp "First
  data collection
  complete";wait
  2000
32: trk 0;rcf 2,
  F#,G#
33: "Count 2*
  number of pulse
  s":
34: itf(D#[1,
  2])+A;0+C
35: for I=2 to
  2048
36: if abs(itf(D
  #[2I-1,2I])-
  A)=1;1+C+C;itf(
  D#[2I-1,2I])+A
37: next I
38: C+M
39: itf(E#[1,
  2])+A;0+C
40: for I=2 to
  2048
41: if abs(itf(E
  #[2I-1,2I])-
  A)=1;1+C+C;itf(
  E#[2I-1,2I])+A
42: next I
43: C+N
44: "Set startin
  g Binary Parity
  =1":
45: if itf(D#[1,
  2])=0;M+1+M
46: if itf(E#[1,
  2])=0;N+1+N
47: if itf(D#[40
  95,4096])=1;M+
  1+M
48: if itf(E#[40
  95,4096])=1;N+
  1+N
49: dim Z#[64],
  A[M],B[N]
50: for I=1 to
  64
51: " "+Z#[I,I]
52: next I
53: enr "Head
  Code",Z#
54: if itf(D#[1,
  2])=0;0+A[I];
  2+A;jmp 2
55: 1+A

```

```

56: if itf(E#[1,
    2])=0;0→B[1];
    2→B;jmp 2
57: 1→B
58: itf(D#[1,
    2])→C;itf(E#[1,
    2])→D
59: "Store Data
    in A[*]&B[*]":
60: for I=2 to
    2048
61: if abs(itf(D
    #[2I-1,2I])-
    C)=1;I-1→A[A];
    A+1→A;itf(D#[2I
    -1,2I])→C
62: next I
63: for J=2 to
    2048
64: if abs(itf(E
    #[2J-1,2J])-
    D)=1;J-1→B[B];
    B+1→B;itf(E#[2J
    -1,2J])→D
65: next J
66: if itf(D#[40
    95,4096])=1;
    A[M-1]→A[M]
67: if itf(E#[40
    95,4096])=1;
    B[N-1]→B[N]
68: dsp "Data
    acquired";wait
    2000
69: trk 0;rcf 3,
    M,N,2#
70: rcf 4,A[*],
    B[*]
71: end

```

Appendix D

Properties of the Cross-Correlation Function

If the eroding flux of particles is of magnitude F (units $\text{kg m}^{-2} \text{s}^{-1}$), and the cross-sectional area of the stream is A , then the average number of particles of average mass m striking the target per second is

$$\text{Average number of particles striking target} = \frac{FA}{m}$$

$$\text{Average time between impacts} = \frac{m}{FA} = \alpha$$

Equation D1

Therefore, in time T the average total number of particles, n , striking the target is given by

$$n = \frac{FAT}{m} = \frac{T}{\alpha}$$

Equation D2

If the width of each light curtain in the optical velocity sensor is L , and the erosive grains are of size d , and if the average velocity is v_m , then the average pulse width from the squarer circuit is T_p , where

$$T_p = \frac{(L + 2d)}{v_m}$$

Equation D3

Note: this last expression will depend upon the sensitivity of the photo-multiplier tubes.

T_p will be accurately stored in the digital recorder if the sampling period, T_s , of the recorder is less than T_p ,

$$T_s < T_p$$

If this condition is not satisfied then there is little point in using this method of velocity measurement because the recorder will be discarding a significant proportion of the data. The shortest pulse length that could possibly be generated would be about $2 \mu\text{s}$ in duration, corresponding to very small particles ($d \ll L$) travelling at 500 ms^{-1} conversely, the longest pulse length will be about $100 \mu\text{s}$, being for large particles ($2d \sim L$) travelling at 20 ms^{-1} . It is this kind of argument that governs the choice of recorder sampling speed.

The number of stored pulses, in one channel, that will participate in producing a value of the cross-correlation function at a time delay of τ , is given by

$$n \left(1 - \frac{\tau}{T}\right)$$

where n has already been defined and T is now taken to mean the time to record the sample (time to fill the digital recorder memory).

The peak of cross-correlation occurs at $\tau = \tau_o$ and is equivalent to the integration of the pulses participating in the evaluation. The peak value, $\Phi(\tau_o)$, can be computed once the average pulse period, T_p , is converted into memory periods (number used in recording is M) in integer values of T_s .

$$T_p(\text{in sample periods}) = \frac{T_p}{T} M$$

Then the peak value follows directly, for the case of a mono-velocity stream of particles.

$$\Phi(\tau_o) = nM \frac{T_p}{T} \left\{ 1 - \frac{\tau_o}{T} \right\}$$

Using equation D2 to eliminate n we obtain the result.

$$\text{Peak } \Phi(\tau_o) = M \frac{T_p}{\alpha} \left\{ 1 - \frac{\tau_o}{T} \right\}$$

Equation D4

The width of the peak will be just twice the average pulse width, namely:

$$\text{Peak width} = 2M \frac{T_p}{T}$$

Equation D5

The integrated area of such a triangular peak can now be written down.

$$\text{Area under the peak } I_p = M^2 \frac{T_p^2}{\alpha T} \left\{ 1 - \frac{\tau_o}{T} \right\}$$

Equation D6

Away from this peak, there is a non-zero probability of pulses overlapping at random and producing a non-zero value of $\Phi(\tau)$. The value of $\Phi(\tau)$ at this point is given by an expression very similar to equation D4 multiplied by the probability of random overlap occurring,

$$\Phi(\tau) = M \frac{T_p}{\alpha} \left\{ 1 - \frac{\tau}{T} \right\}$$

The probability factor is the case of independent probabilities, which is the probability of two pulses being at one particular time coordinate simultaneously. This latter probability is on average given by

$$P(\text{Observing one pulse at time} = \tau') = \frac{T_p}{\alpha}$$

Then

$$P(\text{Observing two pulses overlapping at time} = \tau'') = \left(\frac{T_p}{\alpha} \right)^2$$

where τ' need not equal τ'' .

The required expression is now,

$$\text{Background } \Phi(\tau) = M \left(\frac{T_p}{\alpha} \right)^3 \left\{ 1 - \frac{\tau}{T} \right\}$$

Equation D7

The ratio of $\Phi(\tau_o)$ (peak) to the value of $\Phi(\tau)$ (background) in the vicinity of $\tau = \tau_o$ is on average given by

$$\frac{\Phi(\tau_o) \text{ (peak)}}{\Phi(\tau_o) \text{ (background)}} = \left(\frac{T_p}{\alpha} \right)^3$$

Equation D8

Equation D8 is important in deciding upon the existence of a peak. The expression shows that the cross-correlation technique works best if $\alpha \gg T_p$, which is the case of low flux concentrations; however, $\alpha = 10 T_p$ still represents a very satisfactory condition, and it is only when very high flux conditions prevail, in conjunction with low velocities, that $\alpha = T_p$ may occur.

Another easily deduced parameter is the integrated background count, I_b ,

$$I_b = \sum_{\tau=0}^T \Phi(\tau)$$

When it is taken into account that the data is stored in digitized steps, i.e.

$$\tau = \left\{ \frac{T}{M-1} \right\} i$$

Then it is possible to calculate I_b using equation D7 to replace $\Phi(\tau)$.

$$I_b = \sum_{i=0}^{M-1} M \left(\frac{T_p}{\alpha} \right)^3 \left\{ 1 - \frac{i}{M-1} \right\} = M \left(\frac{T_p}{\alpha} \right)^3 \left\{ \sum_{i=0}^{M-1} 1 - \frac{1}{(M-1)} \sum_{i=0}^{M-1} i \right\}$$

The expression inside the curly brackets can be evaluated using standard results, yielding the result.

$$I_b = \frac{M^2}{2} \left(\frac{T_p}{\alpha} \right)^3$$

Equation D9

Again the advantage of having $\alpha > T_p$ is apparent, in this instance to minimize the background count. This last comment cannot be applied indiscriminately; there is a disadvantage in having $T_p \ll \alpha$ because it is important that $T_s < T_p$ for reasons already discussed, but $T = MT_s$ and if $\alpha \sim T$, then there will be too few particles recorded to give a good statistical sample - in this case a good statistical

sample would be produced by between thirty and one hundred particles passing through the optical sensor during the period recorded, T .

The ratio of I_p to I_b illustrates an interesting corollary to the previous paragraph.

$$\frac{I_p}{I_b} = 2 \left\{ 1 - \frac{\tau_o}{T} \right\} \frac{\alpha^2}{TT_p}$$

Equation D10

Now

$$\left\{ 1 - \frac{\tau_o}{T} \right\} = < 1$$

so to an instructive approximation

$$\frac{I_p}{I_b} \cong \frac{\alpha^2}{TT_p}$$

Consider the following two cases:

1. If $\alpha \sim T_p$, which is the case of a large flux of erosive particles, then $0 < I_p/I_b = < 1$, and usually this would mean $I_p/I_b \sim 0$.
2. If $\alpha \sim T$, which is the case of a very small flux of erosive particles, then $I_p/I_b >= 1$, and usually this would mean $I_p/I_b \gg 1$.

Both cases represent poor statistical samples, and therefore a good sample is when $T > \alpha > T_p$; or when α is the geometric mean of T and T_p .

$$\alpha = \sqrt{TT_p}$$

Note: under these conditions, the calculation of I_b becomes inaccurate since in calculating I_b we have neglected the contribution due to $\Phi(\tau_o)$ around $\tau = \tau_o$.

Velocity Distributions

In the case of a non-ideal erosive stream, the number of erosive particles will be distributed over a range of velocities; this in turn will affect the form of the cross-correlation function. Given these conditions it would be expected that the peak $\Phi(\tau_o)$ will be reduced in magnitude, whilst the peak width will increase. It is a little easier to discuss this complication in terms of a time-delay distribution, $n(\tau)$; where $n(\tau)$ is that number of particles travelling at a velocity of l/τ , where τ is the distance between the light curtains in the sensor.

It should be first noticed that if the following poor sampling condition exists, $T_s \sim T_p$, then it becomes very easy to interpret $n(\tau)$ in terms of $\Phi(\tau)$

$$n(\tau) = \frac{\Phi(\tau)}{\left(1 - \frac{\tau}{T}\right)}$$

This can be concluded by considering equation D4 with $T_p = T_s$. Here we have neglected the effects of any random contribution to $\Phi(\tau)$, which will be a good assumption for a sufficiently small range of distributed velocities.

The case of $T_p > T_s$ is illuminated by the preceding argument; figure D.1 shows schematically the effect of non-unity pulse width. To evaluate the magnitude of $\Phi(\tau)$ within the distributed range of τ_o , for one value, say τ_o' , it is only necessary to sum the contributions arising from the broad peaks on either side of $\Phi(\tau_o')$,

$$\begin{aligned} \Phi(\tau_o') = & \sum_{\tau=\tau_o'}^{\tau_o'-\omega} n(\tau) \left(1 - \frac{\tau}{T}\right) \omega \left\{1 - \left[\frac{\tau_o' - \tau}{\omega}\right]\right\} + \sum_{\tau=\tau_o'}^{\tau_o'+\omega} n(\tau) \left(1 - \frac{\tau}{T}\right) \omega \left\{1 - \left[\frac{\tau_o' - \tau}{\omega}\right]\right\} \\ & - n(\tau_o') \left\{1 - \frac{\tau_o'}{T}\right\} \omega \end{aligned}$$

Equation D11

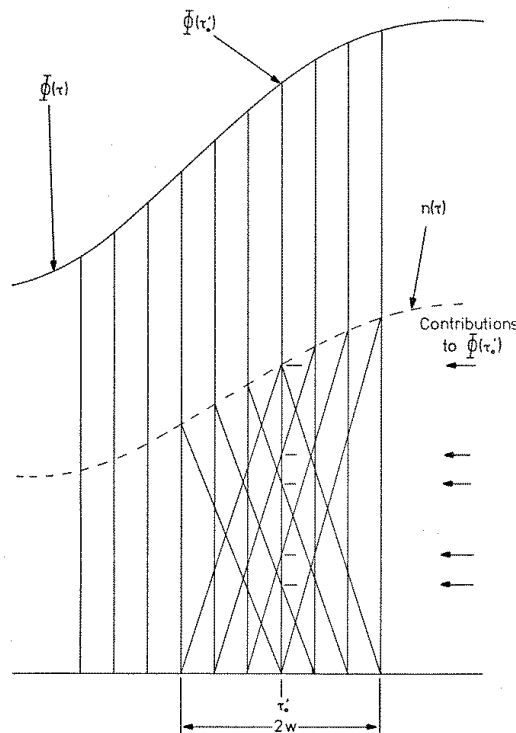


Figure D.1

Sketch showing the relationship between the cross-correlation function $\Phi(\tau)$ and the number distribution of particle time delays $n(\tau)$ in the neighbourhood of a peak at $\tau = \tau_o$. The contributions to $\Phi(\tau_o')$ are shown which arise from adjacent peaks having finite width.

where $\omega = (Tp/T)M$, the half-width of the peak due to a mono-velocity distribution. The last term in equation D11 must be included because the same term has been counted once too often in the previous terms. In the limit as $\omega \rightarrow 1$ (in integer steps) then each sum consists of only two terms; expanding the expression we obtain:

$$\Phi(\tau'_o) = \left[n(\tau'_o) \left\{ 1 - \frac{\tau'_o}{T} \right\} + 0 \right] + \left[n(\tau'_o) \left\{ 1 - \frac{\tau'_o}{T} \right\} + 0 \right] - n(\tau'_o) \left\{ 1 - \frac{\tau'_o}{T} \right\}$$

Thus,

$$\Phi(\tau'_o) = n(\tau'_o) \left\{ 1 - \frac{\tau'_o}{T} \right\}$$

which is the case of $T_s = T_p$, the case of *non-interacting peaks*. Equation D11 does not easily predict the form of $n(\tau)$ for a given $\Phi(\tau)$. However, it does indicate that if the range of the distribution in velocity is given by $v_1 < v < v_2$, then the corresponding distribution in time-delay space (τ -space) is $x/v_2 - \omega < \tau < x/v_1 + \omega$. Thus the existence and range of a velocity distribution can be detected in the cross-correlation plot, even if the form of the distribution still remains uncertain.

Bibliography

- Ascarelli, P. (1971). *Technical Report 71 - 47*. AMMRC .
- Barkalow, R. H., & Pettit, F. S. (1979). *Proceedings of the 5th International Congress on Erosion by Liquid and Solid Impact*. Cambridge. UK.
- Bitter, J. G. (1963). *Wear (6)* , 169 - 190.
- Calladine, H. W. (1969). *Engineering plasticity*. Oxford, UK: Pergamon.
- Carslaw, H. W., & Jaeger, J. C. (1947). *Conduction of Heat in Solids*. Oxford, UK: Pergamon.
- Carter, G., & Nobes, M. J. (1979). *Wear (53)* , 245 - 261.
- Carter, W. J. (1973). *Metallurgical effects at high strain-rates*. New York, USA: Plenum Press.
- Chaudhri, M. M. (1980). Private communication - to be published.
- Christian, T. (1979). *Wear (54)* , 145 - 155.
- Christian, T., & Shewmon, P. G. (1979). *Wear (52)* , 57-70.
- Dapkunas, S. J. (1979). *5th International Congress on Erosion by Liquid and Solid Impact*. Cambridge, UK.
- Davies, R. M. (1949). *Proceedings of the Royal Society A (197)* , p. 416.
- Dearnaley, G. (1978). *Materials in Engineering Applied (1)* , 28 - 41.
- Duvall, G. E., & Graham, R. A. (1977). *Review of Modern Physics vol 49 (3)* , 523 - 579.
- Eddington, J. W., & Wright, I. G. (1978). *Wear (53)* , 131 144, 145 - 155.
- Field, J. E. (1966). *Philosophical Transactions A (260)* , 86 - 93.
- Finnie, A. (1960). *Wear* , pp. 87-103.
- Finnie, I. (1958). *Proceedings of the 3rd US Congress of Applied Mechanics*, (pp. 527-532).
- Finnie, I. (1972). *Wear (19)* , 81 - 90.
- Finnie, I., & McFadden, D. H. (1978). *Wear (48)* , 181 - 190.
- Finnie, I., Wolak, J., & Kabil, Y. (1967). *Journal of Materials (2)* , pp. 682 - 700.
- Goodwin, J. E., Sage, W., & Tilly, G. P. (1969). *Proceedings of the Institution of Mechanical Engineers (184)* , pp. 279 - 291.

- Gulden, M. E. (1979). *Proceedings of 5th International Congress on Erosion by Liquid and Solid Impact*. Cambridge, UK.
- Hartley, C. S., Jenkins, D. A., & Lee, J.-J. (1979). *Proceedings of 5th International Conference on the Strength of Metals and Alloys*. Aachen, Germany.
- Horne, J. G. (1979). *PhD Thesis*. Cambridge, UK: University of Cambridge.
- Hutchings, I. (1977). *International Journal of Mechanical Science* (19) , 45 - 52.
- Hutchings, I. M. (1975). *Wear* (35) , 371 - 374.
- Hutchings, I. M. (1979). *Proceedings of the 5th International Congress on Erosion by Liquid and Solid Impact*. Cambridge, UK.
- Hutchings, I. M. (1974). *PhD Thesis*. Cambridge UK: Cambridge University.
- Hutchings, I. M., & Winter, R. E. (1975). *Journal of Physics E*(8) , 84.
- Hutchings, I. M., Winter, R. E., & Field, J. E. (1976). *Proceedings of the Royal Society of London A* (348) , 379-392.
- Ives, L. K. (1977). *Journal of Engineering Materials and Technology*(97) , 126 - 133.
- Jennings, W. H., Head, W. J., & Manning, C. R. (1976). *Wear* (40) , 93 - 112.
- Kleis, I. R. (1969). *Wear* (13) , 199 - 215.
- Clueh, R. L., & Oakes, R. E. (1977). *Transactions of ASME Series H* , 350 - 358.
- Meguid, S. A., Johnson, W., & Al-Hassani, S. T. (1976). *Proceedings of 17th MTDR conference*, (pp. 653 - 659). Birmingham, UK.
- Nielson, J. H., & Gilchrist, A. (1968). *Wear* (11) , 111 - 122, 123 - 143.
- Perfect, D. A. (1966). *Technical Report 66008*. Royal Aircraft Establishment, Ministry of Aviation, UK.
- Raask, E. (1979). *5th International Congress on Erosion by Liquid and Solid Impact*. Cambridge, UK.
- Rickerby, D. G., & MacMillan, N. H. (1979). *Private communication* .
- Seigel, A. E. (1965). *AGARDograph* (91) .
- Sheldon, G. L., Maji, J., & Crowe, C. T. (1977). *Journal of Engineering Materials and Technology* (97) , pp. 138 - 143.
- Shewmon, P. G. (1979). *Proceedings of the 5th International Congress on Erosion by Liquid and Solid Impact*. Cambridge UK.
- Smeltzer, C. E., Gulden, M. E., McElmury, S. S., & Compton, W. A. (1970). US Army Aviation Materials Laboratory Technical Report 70-36.

- Smithells, C. J. (1962). *Metals Reference Book Volumes I and II*. London, UK: Butterworths.
- Tabor, D. (1951). *The Hardness of Metals*. Oxford, UK: Clarendon Press.
- Takasaki, H. (1970). *Applied Optics (9) vol 6* .
- Taylor, G. I. (1946). *Journal of the Institute of Civil Engineers (26)* , 486.
- Theocaris, P. S. (1969). *Commonwealth & International Library of Science, Technology and Engineering Liberal Studies*. Pergamon Press.
- Tilly, G. P. (1969). *Wear (14)* , 63 - 79, 241 - 248.
- Tilly, G. P. (1973). *Wear (23)* , 87 - 96.
- Tuit, D. A. (1974). *Proceedings of 4th International Conference on Rain Erosion*. Meersburg.
- Uemois, H., & Kleis, I. (1975). *Wear (31)* , 359 - 371.
- Vijh, A. K. (1975). *Wear (35)* , 205 - 209.
- Vijh, A. K. (1976). *Wear (39)* , 173 - 175.
- Vijh, A. K. (1978). *Wear (49)* , 141 - 145.
- Wingorve, A. L. (1971). *Journal of the Australian Institution of Metals vol 16 (1)* , 67 - 70.
- Winter, R. E. (1975). *Pilosophical Magazine vol 31 (4)* , 765.
- Winter, R. E., & Hutchings, I. M. (1974). *Wear (20)* , 141 - 148.
- Winter, R. E., & Hutchings, I. M. (1975). *Wear (35)* , 141 - 148.
- Wood, R. T., & Woodford, D. A. (1979). *5th International Congress on Erosion by Liquid and Solid Impact*. Cambridge, UK.
- Yeh, Y., & Cummins, H. Z. (1964). *Applied Physics Letters (4) No 10* .
- Young, J. P., & Ruff, A. W. (1977). *Journal of Engineering Materials and Technology (97)* , 121- 126.
- Yust, C. S., & Crouse, R. S. (1978). *Wear (5)* , 193 - 196.
- Zener, C., & Holloman, J. H. (1944). *Journal of Applied Physics (15)* , 22.